

**Pulverised Biomass and Coal Co-Firing Simulation Using
Computational Fluid Dynamics**

**A numerical investigation into the aerodynamics of non-spherical particles
and full scale combustion for pulverised fuel applications**

Kristofer Jon Larsen BEng(Hons) MEng

Submitted in accordance with the requirements for the degree of
Doctor of Philosophy

The University of Leeds
Computational Fluid Dynamics Centre,
School of Process, Environmental and Materials Engineering

August 2012

The candidate confirms that the work submitted is his own, except where work which has formed part of jointly-authored publications has been included. The contribution of the candidate and the other authors to this work has been explicitly indicated below. The candidate confirms that appropriate credit has been given within the thesis where reference has been made to the work of others.

This copy has been supplied on the understanding that it is copyright material and that no quotation from the thesis may be published without proper acknowledgement.

© 2012 The University of Leeds and Kristofer Jon Larsen.

The right of Kristofer Jon Larsen to be identified as Author of this work has been asserted by him in accordance with the Copyright, Designs and Patents Act 1988.

Acknowledgements

It is my belief that hermits do not complete doctoral theses (within the time limit at least) and there are a number of people, to whom I wish to show my appreciation here. I am indebted to my supervisors, Dr Alan Burns, Dr Lin Ma, Prof Mohamed Pourkashanian and Prof Alan Williams, and have been greatly assisted by Prof Derek Ingham, for continually and patiently leading the horse back to water.

The funding of the Engineering and Physical Sciences Research Council EP/F061188/1 is gratefully recognised.

Prof Yong Yan, Dr Gang Lu and Mr Xiangchen Qian, School of Engineering and Digital Arts, the University of Kent and Prof Houzhang Tan and Dr Xuebin Wang, School of Energy and Power Engineering, Xi'an Jiaotong University are acknowledged for the access to their experimental data.

Personal gratitude to my friends within the CFD Centre at Leeds University, in particular my close colleagues Dr Sreenivasa Gubba, and Dr Maryam Gharebaghi for providing FG-DVC of the Huating coal. Also for the shared wisdom from those shortly ahead of I, Dr Shengyi Wang and Dr Mohammed Degereji.

Finally I want to recognise the financial, IT and loving support of my family and friends. In particular: my parents; siblings, Ralf, Nils, Harri and Freya; and friends, Jack and Fizz. Even when wilfully ignored your advice has been and is appreciated.

“ *In theory,*
there is no difference between theory and practice.
But in practice,
there is. ”

– Anon.

I. Distribution of Work

Elements of this thesis were performed as part of a research group principally consisting of Dr SR Gubba and I. Also Dr AD Burns, Prof DB Ingham, Dr L Ma, Prof M Pourkashanian and Prof A Williams provided supervision and advice. Chapter 4 includes work from the jointly authored: *Investigations of the Transportation Characteristics of Biomass Fuel Particles in a Horizontal Pipeline through CFD Modelling and Experimental Measurement*, submitted to Biomass and Bioenergy. Chapter 6 includes work from the jointly authored: *Numerical Modelling of the Co-firing of Pulverised Coal and Straw in a 300MW_e Tangentially Fired Boiler*, Fuel Processing Technology. In the former I developed the inter-particle collision model and performed the simulations obtaining the graphics for the paper. Inputs for the cases were calculated by Dr SR Gubba. X Qian and Prof Y Yan obtained the experimental data. In the latter I was responsible for the furnace simulations. Dr SR Gubba developed and implemented a thermal gradient model for large cylindrical particles. Prof HZ Tan and Dr X Wang obtained the experimental data.

Abstract

Recent national and international emissions legislation, in particular sulphur-dioxide, and the rapid depletion of fossil fuels are forcing power producing industries to look at various alternatives, such as biomass and co-firing techniques. Biomass may be transported to the burners of a pulverised fuel (PF) boiler either mixed with the primary fuel, in general coal, or used in dedicated pipelines. In both cases, the transportation of biomass is different due to its composition, size and shape to the transportation of coal.

This thesis investigates the computational modelling techniques for a biomass and biomass blend particle transportation (arboreal and flour) in a pipeline with a transverse elbow, the three-phase flow of a coal and biomass co-fire blend in the primary air annulus of a swirl burner and the combustion of a coal and pelletised straw mixture in a full scale furnace using dedicated burners for the biomass injection.

The comparison of spherical and non-spherical drag models, under gravity, as well as Saffman lift, inter-particle collision and randomised impulsive wall collision models has been investigated. Good agreement was observed between the computational fluid dynamics (CFD) simulations and the experimental data, using a non-spherical drag model. In both cases, due to the dilute volume fraction and secondary air flow, inter-particle collisions and lift were insignificant. In the annulus, lateral regions of high particle concentration were predicted, which are not observed physically.

Numerical simulations of a 300MW_e tangentially fired furnace, co-firing bituminous coal and pelletised straw, have been performed and compared to experimental data. Bituminous coal was co-fired with pelletised straw. Good agreement was obtained between the CFD predictions and the experimental data so that the trends of furnace temperature, NO_x emissions and carbon burnout reduction, as biomass load is increased, were observed. Quantitative prediction of unburnt carbon (UBC) and NO_x require a more detailed picture of the processes within the furnace at higher temperatures than that currently provided by experimental data.

List of Publications

I. Journal Papers

Gubba SR, Ingham DB, Larsen KJ, Ma L, Pourkashanian M, Qian X, Williams A, Yan Y. (2012a) *Investigations of the transportation characteristics of biomass fuel particles in a horizontal pipeline through CFD modelling and experimental measurement.* Biomass and Bioenergy IN PRESS: [dx.doi.org/10.1016/j.biombioe.2012.07.010](https://doi.org/10.1016/j.biombioe.2012.07.010)

Gubba SR, Ingham DB, Larsen KJ, Ma L, Pourkashanian M, Tan HZ, Williams A, Zhou H. (2012b) *Numerical modelling of the co-firing of pulverised coal and straw in a 300MWe tangentially fired boiler.* Fuel Processing Technology IN PRESS: [dx.doi.org/10.1016/j.fuproc.2012.05.011](https://doi.org/10.1016/j.fuproc.2012.05.011)

Larsen KJ, Burns AD, Gubba SR, Ingham DB, Ma L, Pourkashanian M, Williams A. (2012) *Pulverised coal and biomass co-combustion: Particle flow modelling in a swirl burner.* Journal of the Energy Institute SUBMITTED

II. Conference Proceedings

Larsen KJ, Gubba SR, Ingham DB, Ma L, Pourkashanian M, Tan HZ, Williams A. (2011) *Pulverised coal/biomass modelling in a full scale corner-fired boiler.* Proceedings of the 5th International Conference on Clean Coal Technologies, Zaragoza, Spain. 8th-12th May 2011.

Larsen KJ, Burns AD, Gubba SR, Ingham DB, Ma L, Pourkashanian M, Williams A. (2011) *Coal and biomass combustion and pneumatic transportation modelling in a shared swirl burner.* Proceedings of the International Conference on Carbon Reduction Technologies, Jura Krakowsko-Czestochowska, Poland. 19th-22nd September 2011.

Table of Contents

Acknowledgements	III
I. Distribution of Work.....	IV
Abstract	V
List of Publications	VI
I. Journal Papers	VI
II. Conference Proceedings.....	VI
Table of Contents	VII
I. Table of Figures	X
II. Table of Tables	XI
Nomenclature	XII
I. Acronyms	XII
II. Algebraic Parameters	XIII
Chapter 1 Introduction	1
1.1 Background to Biomass Co-Firing	1
1.2 Introduction to Particle Combustion Modelling	6
1.3 The Challenges.....	8
1.4 Objectives	10
1.5 Outline of the Thesis	10
Chapter 2 Literature Survey	12
2.1 Multiphase Modelling for Spherical Particles	12
2.1.1 General Method for Multiphase Modelling.....	13
2.1.2 Turbulence Coupling.....	16
2.1.3 Additional Models.....	18
2.1.4 Spherical Lift.....	19
2.1.5 Spherical Rotation	22
2.1.6 Spherical Inter-Particle Collisions.....	23
2.1.7 Spherical Wall Collisions	28
2.2 Non-Spherical Particle Modelling	34
2.2.1 Measures of Non-Sphericity.....	36
2.2.2 Fixed Orientation Models for Non-Spherical Particles.....	39
2.2.3 Preferred Orientation Models for Non-Spherical Particles	45
2.2.4 Free Orientation Models for Non-Spherical Particles.....	48

2.3	Pulverised Fuel Combustion	48
2.3.1	Coal Combustion Modelling	49
2.3.2	Biomass and Co-Combustion Modelling	51
2.3.3	Pollutant Modelling	52
Chapter 3 Numerical Modelling		54
3.1	Computational Fluid Dynamics	54
3.1.1	The Simulation Process	55
3.1.2	Conservation Equations	56
3.1.3	Gaseous Reactions	59
3.2	Computational Particle Dynamics	61
3.2.1	Lagrangian Particle Treatment	61
3.2.2	Spherical Particle Drag	63
3.2.3	Non-Spherical Drag	66
3.2.4	Spherical Rotation	68
3.2.5	Spherical Lift	70
3.2.6	Inter-particle Collisions	73
3.2.7	Wall Collisions	80
3.3	Combustion of a Single Fuel Particle	81
3.3.1	Inert Heating {1a}{1b}{6}	83
3.3.2	Evaporation {2}	84
3.3.3	Boiling {3}	85
3.3.4	Devolatilisation {4}	85
3.3.5	Volatile Combustion	86
3.3.6	Char Combustion {5}	87
Chapter 4 Biomass Fuel Particle Aerodynamics in a Pipeline.....		89
4.1	Introduction	89
4.2	Experimental Measurement System	93
4.3	Numerical Modelling	95
4.3.1	Non-Spherical Drag	97
4.3.2	Inter Particle Collisions	98
4.4	Results and Discussion	102
4.4.1	Validation Data	104
4.4.2	Modelling Results	107
4.4.3	Results - Flour	109
4.4.4	Results - Willow	113

4.4.5	Results – Mixture of Flour and Willow.....	116
4.4.6	Results – Wood and Bark.....	119
4.4.7	Inter-Particle Collisions.....	122
4.5	Chapter Summary	123
Chapter 5 The Modelling of Coal and Biomass Pneumatic Transportation in a Swirl Burner		127
5.1	Introduction.....	127
5.1.1	Description of the Combustion Test Furnace.....	128
5.1.2	The Particle Flow Case Investigated.....	130
5.2	Computational Modelling	132
5.3	Computed Results and Discussions	135
5.4	Chapter Summary	139
Chapter 6 Co-firing Chinese Straw with Coal in a 300MW_e Tangentially Fired Pulverised Fuel Furnace		140
6.1	Introduction.....	140
6.2	Experimental Facility and Fuel Properties.....	141
6.3	Numerical Grid	146
6.4	Numerical Models.....	149
6.5	Results.....	152
6.6	Chapter Summary	155
Chapter 7 Discussion and Conclusions		157
7.1	General Discussion	157
7.2	Overall Conclusions.....	160
7.3	Future Work.....	164
References		166
Appendix.....		176
A-I	Particle rotational relaxation time.....	176

I. Table of Figures

Figure 1.1	Microscopic images of some typical milled biomass particles.	9
Figure 2.1	Diagram of lift modes.....	21
Figure 3.1	Empirical drag laws.....	64
Figure 4.1	Biomass images.....	90
Figure 4.2	A schematic diagram of the gas-solid flow measurement system at the University of Kent.	93
Figure 4.3	Structure of the Multi-Channel Electrostatic Sensors.	94
Figure 4.4	Schematic of numerical domain and example of the mesh.	95
Figure 4.5	Flour and willow experimental velocities.	105
Figure 4.6	Flour and willow experimental charge levels.....	106
Figure 4.8	Air velocity predictions and measurements.	108
Figure 4.7	Numerical fluid phase velocity vectors and contour plots at the sensor planes.....	108
Figure 4.9	Numerical prediction of Case 1 – 54gmin ⁻¹ flour.....	110
Figure 4.10	CFD predictions and experimental measurements for Cases 1, 2, 3 and 1-Spherical involved in flour transportation.....	112
Figure 4.11	CFD predictions and experimental measurements for Cases 4, 5, 6 and 6-Spherical involved in willow transportation.	115
Figure 4.12	CFD predictions and experimental measurements for Cases 7, 8 and 8-Spherical involved in flour and willow transportation.....	117
Figure 4.13	CFD predictions and experimental measurements for Cases 9, 10, 11 and 9-Spherical involved in wood transportation.....	120
Figure 4.14	CFD predictions and experimental measurements for Cases 12, 13, 14 and 12-Spherical involved in willow transportation.	121
Figure 4.15	Mean axial velocity of the particles against normalised pipe radius.....	124
Figure 5.1	Photograph of the RWE Combustion Test Facility with numerical domains overlaid.	129
Figure 5.2	The mesh arrangement of the computational domain.	130
Figure 5.3	Particle normalised volume fraction against size and aspect ratio.....	131
Figure 5.4	Contours of the computed magnitudes of the air velocity.....	134
Figure 5.5	Predicted secondary air flow.	134
Figure 5.6	Predicted local particle velocities of coal and milled wood.	136
Figure 5.7	Computed local particle number concentrations of coal and milled wood.	136
Figure 5.8	Calculated particle mass fluxes of coal and milled wood.	138
Figure 5.9	Flame stabilised on the burner mouth of PF coal/milled wood.....	138

Figure 6.1	Furnace mesh details and temperature boundary conditions.....	142
Figure 6.2	Cross-section of the mesh in the burner region.....	148
Figure 6.3	Calculated temperatures at central planes, measurement planes and outlet.....	153
Figure 6.4	Quantitative evaluation.....	154

II. Table of Tables

Table 2.1	Methods for non-spherical particle modelling.....	35
Table 4.1	Mean properties of the particles investigated.....	103
Table 4.2	Test parameters.....	103
Table 4.3	Percentage by volume of the contribution of flour particles.....	109
Table 4.4	Percentage by volume of the contribution of willow particles.....	114
Table 4.5	Percentage by volume of the contribution of wood particles.....	118
Table 4.6	Percentage by volume of the contribution of bark particles.....	118
Table 6.1	Test conditions from baseline coal and coal/biomass co-firing.....	143
Table 6.2	Fuel combustion properties.....	144
Table 6.3	Particle size properties.....	145
Table 6.4	Fuel NO _x properties.....	146
Table 6.5	Fuel combustion properties.....	149
Table 6.6	Comparison of experimental data and numerical predictions.....	152

Nomenclature

I. Acronyms

A	Ash	LES	Large eddy simulation
ALE	Arbitrary Lagrangian-Eulerian	M	Moisture
AR	As received	ODE	Ordinary differential equation
BC	Boundary condition	PDE	Partial differential equation
BET	Brunauer, Emmett and Teller	PDF	Probability density function
CFD	Computational fluid dynamics	PC	Pulverised coal
CRW	Continuous random walk	PF	Pulverised fuel
CSF	Corey shape factor/function	RANS	Reynolds-averaged Navier-Stokes
CV	Control volume	RHS	Right hand side
DAF	Dry, ash-free	RKM	Runge-Kutta method
DES	Detached eddy simulation	RMS	Root mean square
DNS	Direct numerical simulation	RO	Renewables obligation
DPM	Discrete particle model	ROC	Renewables obligation certificate
DRW	Discrete random walk	R/P	Reserves to production
ECS	Equivalent circumference sphere	RSM	Reynolds stress method
EPS	Equivalent projected area sphere	SRC	Short rotation coppice
ESS	Equivalent surface area sphere	TVM	Turbulent viscosity method
EVS	Equivalent volume sphere	UDF	User defined function
FC	Fixed carbon	UDM	User defined memory (memory location for cell)
FDM	Finite-difference method	VM	Volatile matter
FEM	Finite element method		
FVM	Finite volume method		

II. Algebraic Parameters

a	Particle radius [m]	$d_{p0,j,k}$	Local particle diameter of class j in cell k [m]
A^*	Max-med-min area	d_s	Collision subject diameter [m]
A_1	Devolatilisation pre-exponential term [s^{-1}]	D	Settling tube diameter [m]
A_{EVS}	Surface area of the equivalent volume sphere [m^2]	$D_{i,k}$	Dwell of particle stream i in cell k [s]
A_g	Specific internal surface area [$m^2 kg^{-1}$]	D_0	Oxidant diffusion rate [$m^{-1}s$]
A_i	Intrinsic pre-exponential term [$m^{-1}s$]	$D_{m,j}$	Mass diffusivity of species j [$m^2 s^{-1}$]
A_p	Particle projected area [m^2]	D_t	Turbulent diffusivity [$m^2 s^{-1}$]
A_s	Particle surface area [m^2]	$D_{T,j}$	Volumetric thermal diffusivity of species j [$m^{-1}s^{-1}$]
c_p	Particle concentration [m^{-3}] {particle physics}	e	Coefficient of restitution {particle physics}
c_p	Specific heat capacity at constant pressure [$Jkg^{-1}K^{-1}$] {chemistry}	e	Specific internal energy [Jkg^{-1}] {chemistry}
C_1	Coefficient of oxidant diffusion	E	Specific total enthalpy [Jkg^{-1}]
$C_{i,s}$	Vapour concentration at particle surface [$mol.m^{-3}$]	E_1	Devolatilisation activation energy [$J.mol^{-1}$]
$C_{i,\infty}$	Vapour concentration in environment (fluid) [$mol.m^{-3}$]	E_i	Intrinsic activation energy [$J.mol^{-1}$]
C_D	Drag coefficient	f_c	Collision frequency [Hz]
C_D^*	Normalised drag coefficient	f_h	Fraction of char heat retained by the particle
C_M	Coefficient of Magnus lift	\bar{f}_D	Specific drag force [Nkg^{-1}]
C_R	Coefficient of rotation	\bar{f}_G	Specific gravimetric force [Nkg^{-1}]
C_S	Coefficient of Saffman lift	\bar{f}_L	Specific lift force [Nkg^{-1}]
C_{sV}	Swelling coefficient	f_{M0}	Initial moisture fraction
d_{EPS}	Equivalent projected area diameter [m]	f_{V0}	Initial volatile matter fraction
d_{EVS}	Equivalent volume diameter [m]	\vec{F}	Body forces [N]
d_o	Collision object diameter [m]	\vec{F}_D	Drag force [N]
d_p	Particle diameter [m]	\vec{F}_M	Magnus (rotation) lift force [N]

\bar{F}_s	Saffman (shear) lift force [N]	L_r	Roughness cycle length [m]
\bar{g}	Local gravitational constant [ms ⁻²]	\dot{m}_i	Mass flow rate of particle stream i [kgs ⁻¹]
h	Convective heat transfer coefficient [Wm ⁻² K ⁻¹] {particle physics}	$m_{\text{mass},k}$	Static mass of particles in cell k [kg]
h	Specific enthalpy [Jkg ⁻¹] {chemistry}	m_o	Mass of collision object [kg]
h_{fg}	Latent heat of evaporation [Jkg ⁻¹]	m_p	Particle mass [kg]
H	Inverse rotational relaxation time [s ⁻¹]	m_s	Mass of collision subject [kg]
H_r	Average roughness height [μm]	M	Mass ratio (collision)
H_j	Enthalpy of species j [J]	M_j	Molecular weight of species j [kg.mol ⁻¹]
H_{reac}	Heat of reaction [Jkg ⁻¹]	n_p	Particle concentration [m ⁻³]
I	Identity matrix	\hat{N}	Normal unit vector
I_{cyl}	Cylindrical particle moment of inertia about a diametric axis through the centre [kgm ²]	N_i	Molar flux of vapour [mol.m ⁻² s ⁻¹]
I_p	Particle moment of inertia about spherical diametric axis [kgm ²]	p	Pressure [Pa]
\bar{j}	Particle impulse [Ns]	$p_{\text{cell},k}$	Population of particles in cell k
\bar{J}_j	Specific diffusive flux of species j [m ⁻² s ⁻¹]	P_c	Collision probability
k	Turbulent kinetic energy [m ² s ⁻²]	P_p	Projected perimeter [m]
k_1	Devolatilisation rate [s ⁻¹]	r	Random radius of collision [m]
k_c	Specific mass transfer coefficient [ms ⁻¹]	\Re	Intrinsic reaction rate [m ⁻¹ s]
k_{eff}	Effective thermal conductivity [Wm ⁻¹ K ⁻¹]	R	Universal gas constant (8.3145 J.mol ⁻¹ K ⁻¹)
k_R	Stokes' correction to rotation	R_c	Collision cylinder radius [m]
k_S	Stokes' correction to drag	R_j	Reaction source term of species j [kgm ⁻³ s ⁻¹]
K_1	Stokes' shape factor	$R_{r,j}$	Volumetric rate of production of species j in reaction r [m ⁻³ s ⁻¹]
K_2	Newton's shape factor	Re	Reynolds number
		Re_K	Effective Reynolds number
		Re_p	Particle (translational) Reynolds number
		Re_r	Rotational Reynolds number

Re_s	Shear Reynolds number	V	Volume [m^3]
$\bar{s}_{i,k}$	Displacement of particle stream i in cell k [m]	y_j	Specific mass fraction of species j [kg^{-1}]
S_h	Volumetric power source term [Wm^{-3}]	Y	Ratio of tangential particle surface velocity to total tangential magnitude (i & j components)
S_j	Discrete source term of species j [$kgm^{-3}s^{-1}$]	Y_j	Mass fraction of species j
S_m	Volumetric mass source term [$kgm^{-3}s^{-1}$]	β	Corey shape factor
T	Temperature [K]	γ_m	Maximum virtual wall inclination [$^\circ$]
\dot{T}	Heating rate [Ks^{-1}]	Δt	Timestep [s]
\hat{T}	Tangential unit vector	ε	Turbulent dissipation rate [m^2s^{-3}]
\bar{T}	Torque [Nm]	ε_p	Particle emissivity
T_0	Initial temperature [K]	$\bar{\zeta}$	Fluid vorticity [$^\circ s^{-1}$]
T_p	Particle temperature [K]	η	Effective reaction rate
T_t	Integral timescale of turbulence	θ	Angle of incidence [$^\circ$]
T_∞	Environmental (fluid) temperature [K]	θ_R	Radiation temperature [K]
$\bar{u} \mid \bar{u}_f$	Fluid velocity [ms^{-1}]	μ	Dynamic viscosity [$kgm^{-1}s^{-1}$]
$\bar{u}_{mass,k}$	Sum-product of mass and velocity of particles in cell k [$kgms^{-1}$]	μ_d	Coefficient of dynamic friction
u_n	Relative speed of collision in normal direction [ms^{-1}]	μ_s	Coefficient of static friction
\bar{u}_o	Velocity of collision object [ms^{-1}]	$v'_{r,j}$	Stoichiometric coefficient of reactant species j in reaction r [mol]
\bar{u}_p	Particle velocity [ms^{-1}]	$v''_{r,j}$	Stoichiometric coefficient of product species j in reaction r [mol]
$\bar{u}_{p0j,k}$	Local particle velocity of class j in cell k [ms^{-1}]	ξ_N	Gaussian random number ($\mu = 0, \sigma = 1$)
\bar{u}_{rms}	Average fluid velocity [ms^{-1}]	ξ_U	Uniform random number [0,1]
\bar{u}_s	Velocity of collision subject [ms^{-1}]	$\rho \mid \rho_f$	Fluid density [kgm^{-3}]
u_t	Relative speed of collision in tangential direction (i & j components) [ms^{-1}]	ρ_p	Particle density [kgm^{-3}]
\bar{U}	Relative velocity [ms^{-1}]	$\rho_{massj,k}$	Sum-product of mass and density of class j in cell k [kg^2m^{-3}]

$\rho_{p0j,k}$	Local particle density of class j in cell k [kgm^{-3}]	ω_n	Relative angular speed about normal axis [$^{\circ}\text{s}^{-1}$]
σ	Stefan-Boltzmann constant ($5.67 \times 10^{-8} \text{ Wm}^{-2}\text{K}^{-1}$)	$\bar{\omega}_o$	Angular velocity of collision object [$^{\circ}\text{s}^{-1}$]
Σ	Dimensionless shear rate	$\bar{\omega}_p$	Particle angular velocity [$^{\circ}\text{s}^{-1}$]
$\bar{\tau}$	Stress tensor [Pa]	$\dot{\bar{\omega}}_p$	Particle angular acceleration [$^{\circ}\text{s}^{-2}$]
$\bar{\tau}_{\text{eff}}$	Effective stress tensor [Pa]	$\bar{\omega}_s$	Angular velocity of collision subject [$^{\circ}\text{s}^{-1}$]
τ_p	Particle (translational) relaxation time [s]	ω_t	Relative angular speed about tangential axes (i & j components) [$^{\circ}\text{s}^{-1}$]
τ_ω	Particle rotational relaxation time [s]	$\bar{\Omega}$	Relative angular velocity [$^{\circ}\text{s}^{-1}$]
ϕ	Random roll angle of collision [$^{\circ}$]		
Φ	Sphericity		
$\bar{\omega}_f$	Fluid angular velocity [$^{\circ}\text{s}^{-1}$]		

Throughout this thesis all instances of the statement ‘Fluent’ refer to ANSYS Fluent. Various versions have been used, v12.0 in Chapter 4, v13.0 in Chapter 5 and the other chapters referring to Fluent’s current capabilities, and v12.1 in Chapter 6. Within the body text the subscripts, $_e$ and $_{th}$, refer to electrical and thermal, respectively, as bases for stating a power rating or proportion. An italicised capital N has been used to denote ‘normal’ in reference to the normal cubic metre ($N\text{m}^3$) to prevent any confusion with the newton (N).

Chapter 1

Introduction

1.1 Background to Biomass Co-Firing

In 2010 the total world coal consumption was approximately 149EJ_{th} , which is equivalent to 29.6% of the total primary energy consumption (BP, 2011). Coal has consistently been the source for approximately 40% of the world's electricity generation over the past 40 years, despite a rise in nuclear and gas power (OECD, 2010). Over the same period, electricity production has increased 1.74 times faster than primary energy consumption (OECD, 2010, and BP, 2011). Furthermore, the future of civil nuclear power is uncertain following Germany's response to the crisis at Fukushima. With the best of renewable intentions, coal is still the natural substitute for baseline nuclear power at a similar price.

This thesis is a product of an EPSRC UK-China collaborative research project. The high population and rapid industrialisation of China make her a key focus of energy and environmental research, in particular the pertinence of the Chinese energy market to the goals of coal and biomass co-firing research is reinforced below.

China's use of coal is increasing at a rate approximately 8% more rapidly than the average for the rest of the world over the past 5 years, and coal represented 70% of the country's primary energy consumption in 2010. Although the Reserves to Production (R/P) ratio for Chinese coal (BP, 2010) is optimistically calculated as 35 years, due to the constant rate of extraction used, despite China representing 49% of the total world coal consumption in 2010, she retains approximately 15 years of proven native coal reserves, if extrapolated at the 2010 annual rate of growth (0.10 from BP, 2010) without any imports. Alternatively there is 8 years' worth of native coal in China if the 10 year average rate of growth continues. Following the same equilibrium consumption method, used to estimate China's R/P ratio, suggests that there are 25 years of coal reserves in the world. In all cases the evaluation of proven reserves tends to be conservative. These data suggest that the exploitation of coal for power is unlikely to diminish in the

medium term and should continue to rise in China. In addition to this, as the largest agricultural country in the world, China has vast under-utilised agrowaste resources amounting to about 820Mt (Cai *et al.*, 2007). All this is without considering biomass from forestry sources. Taking into account animal feeding and imperfect collection, there remains at least 400Mt of Chinese cotton, maize and wheat straw residues alone as of 2006 (Cai *et al.*, 2007). It has been estimated that approximately 23% of this surplus straw was openly burnt in fields between 2000 and 2003. Although this proportion varies greatly with location, it was shown to increase with the regional rural population density and affluence (Cao *et al.*, 2008). Therefore, bearing in mind the 1350Mt (approximately 37EJ_{th}) of bituminous coal that was consumed in China's electrical power stations in 2008 (IEA, 2011), it might be suggested that co-firing at 15-20%_{th} waste straw would utilise the whole resource. Of course the economic practicalities of this scenario are not certain, but if a significant number of power plants were to add around 10% straw then this would appear to be a sensible proposal before other methods of disposal were found for the straw.

Potential energy yields from fuel crops on the world stage are less certain as the various predictions must assume scenarios involving different human behaviours. Therefore predictions are made ranging from essentially nil to supplying the current world total annual primary energy consumption of about 600EJ_{th} when agro-wastes are utilised (Slade, 2012). There are two predominant ethical balances which are likely to limit energy crop production significantly below the theoretical maximum. The first is the so called 'food versus fuel' debate, in which limited arable land is under competition to feed humans and livestock as well as grow fuel and chemical feedstocks. This could drive up food prices with dire human consequences. The second is the destruction of wild habitats to extend arable land to ensure food and energy crops. In many cases this would have a negative environmental impact globally, let alone consideration of the local wildlife. Rainforest clearances, for example, may be seen, in a purely abstract sense, as the release of medium term carbon stores to the atmosphere and thus cause far greater damage than any fossil-carbon offsetting from the new land use (Slade, 2012). Legislation could inadvertently subsidise such counter-productive measures and so these remain important issues.

Co-firing biomass in existing pulverised coal fired power stations is seen as the most economically and rapidly adoptable method to increase the proportion of power generated from renewable sources (Basu *et al.*, 2011). A reduction in fossil-CO₂ emissions is possible by replacing a proportion of the coal with a ‘carbon neutral’ biomass. This is particularly beneficial where the supplanting biomass is a waste agricultural residue that would release carbon emissions were it not utilised, but without useful energy output. Studies have also shown improvements in the NO_x and SO_x emissions when comparing coal firing and co-firing (Battista *et al.*, 2000, Damstedt *et al.*, 2007, and Wang *et al.*, 2011). In fact co-firing from a desire to reduce these harmful emissions predates the ‘carbon neutral’ aims.

Pulverised fuel (PF) combustion is the major technology for modern coal power stations, commonly called pulverised coal (PC). In the UK, grate fired boilers have been superseded and fluidised bed reactors are less popular. PC was originally pioneered to rapidly increase the burning rate of the combustion as air and coal dust mixtures had, under tragic circumstances, been found to be explosive. In modern plants, lump coal is generally delivered by rail to be stored and subsequently milled to powder as required. The coal dust is transported pneumatically through the feedpipes to the burners in the furnace (Williams *et al.*, 2000b). Schneider *et al.* (2002) give an interesting account of the use of computational fluid dynamics (CFD) in such an investigation for coal, where efficiency is much increased by a rope splitter prior to the riffle-bifurcator. Different configurations of these burners exist and for more detail the reader is directed to Basu *et al.* (2000).

The great advantage of retrofit co-firing over other renewable generation technologies is the minimal capital outlay. Also, compared to purely renewable thermal energy, even new build coal-biomass co-firing can offer large plant efficiency and a safe trading position for tactical withdrawal from unfavourable biomass prices in the emerging market, in the form of the mature coal market (Dai *et al.*, 2008). In England and Wales, the Renewable Obligation (RO) scheme drives the co-firing of ‘energy crops’ with coal. ‘Energy crops’ are defined as short rotation coppice (SRC) wood (willow and poplar) and miscanthus (elephant grass). In 2010-11, just over 11%_e of the energy, sold by suppliers, had to be covered by equivalent renewable obligation

certificates (ROCs) (DECC, 2010). This does not necessarily mean 11% of the electricity sold had to be renewable since the ROCs and energy may be bought separately. In addition, different sources may be worth multiple, or indeed fractional, ROCs per MWh. Suppliers who do not meet their obligation must pay a fixed ‘buy-out’ price per ROC, for which they are liable, into the ‘mutualisation fund’ (DECC, 2010). The collected ‘buy-out’ payments are effectively awarded as a dividend on all ROCs held by suppliers that did meet their obligation.

Although, in the governmental scheme, biomass and coal co-firing has low value (half a ROC per MWh electricity production times the proportion of heat input from the biomass or a full ROC if the biomass is an ‘energy crop’), there are many reports that <10%_{th} biomass in coal is safe (Battista *et al.*, 2000, Damstedt *et al.*, 2007, and Wang *et al.*, 2011). Furthermore with only a 25 year guarantee as to the life of the ROC scheme, heavy investment in the more expensive renewable energy technologies is a financial risk. In China much focus is on the utilisation of the large surplus of agro-wastes (Cai *et al.*, 2007, and Wang *et al.*, 2011). From a power generator’s perspective, other benefits include biomass’ nature as a low grade fuel. Although unconventional, as chemical energy in form, biomass may be collected and stored far more easily than kinetic (wind) or electromagnetic (solar) sources and production continues at previously connected sites on the distribution network. Locations for the kinetic, electromagnetic and potential (hydroelectric) forms of renewable energy cannot generally be optimised for the end consumer.

Many potential co-firing customers would like to retrofit an existing coal power station, for which different options are present in the redesign of the fuel delivery system. The reasons behind this are highlighted by van Loo and Koppejan (2008), “*Co-firing [of biomass and coal] makes use of the extensive infrastructure associated with the existing fossil fuel-based power systems, and requires only relatively modest additional capital investment. In most countries, the co-firing of biomass is one of the most economic technologies available for providing significant CO₂ reductions.*” Due to financial implications, it is desirable for the two fuels to share as much of the previous infrastructure as possible. It is therefore common for fuel lines to carry both fuels, through bifurcation systems, to all burners. The investigation focuses heavily on

what Dai *et al.* (2008) and van Loo and Koppejan (2008) term ‘direct co-firing’, in which the fuels share a boiler (commonly also feedlines and burners). This is the most popular method of retrofit as it represents the lowest capital investment. Although few journal sources give a full definition of co-firing, the problem specified invariably assumes both fuels in a single boiler in the same vein as direct co-firing. Therefore there are essentially three subdivisions of direct co-firing, depending on the location at which the coal and biomass fuel streams are mixed. These are the “dedicated hopper”, “dedicated mill” and “dedicated burner”, under which methods the streams are mixed, respectively and in increasing proximity to the boiler, in the mill feedpipes, after the mills and within the boiler. “Dedicated” refers to the final equipment used solely for the biomass, of course the same type of equipment is also used for the coal but the separate fuel streams are processed by separate machines. If the equipment were not “dedicated” to biomass, this would mean the biomass is processed by machines also processing coal. The control of the heating value of the fuel blend at injection to the burner is paramount for flame stability, so an important investigation is into whether the blend is maintained in transport along the feed line or the powders coalesce into segregated ropes. Common sense issues relating to the co-energy-conversion of biomass and coal are listed in Dai *et al.* (2008) in which less common methods of coal/biomass co-firing are also introduced. These being the ‘parallel’ and ‘indirect’ techniques, in which a traditional coal boiler is employed in conjunction with, respectively, a dedicated biomass-fired boiler or an alternative chemical to thermal energy conversion technology, e.g. biomass gasification, for steam raising in the turbine drive system, which is common to both the biomass and coal combustion units. Benefits from separation of the fuels for heat generation entail preservation of an existing or proven coal combustion system, whilst allowing deployment of alternative (more suitable) technologies for biomass conversion (Dai *et al.*, 2008) which may be independently optimised. The focus of this thesis rests upon the previously described direct co-firing, with justification given here. Despite the advantages of parallel biomass systems, the construction of an additional new boiler design at an existing generator site is somewhat extraneous to the term “retrofit”. Energy generators desire flexibility in fuel feedstock so that high generation capacity can be maintained through market fluctuations. Although dedicated biomass systems are

likely to be more tolerant of poor fuel quality than co-fire PF, such systems could not be fired with coal and would leave a capacity gap should the biomass be unavailable. Furthermore the dispensation of coal combustion in the biomass boiler design also eliminates PF's advantages for hard coal combustion. Following this argument, it is the author's opinion that research to address the biomass side of such stations will approach that for individual biomass plants. Optimisation of the heat exchange would be readjusted for the separate load requirements and if the exhaust streams are mixed a co-firing system will be necessary here. Other infrastructure required by parallel or indirect co-firing is that of any thermal power station or is peculiar to biomass (such as fuel handling), without specialised co-firing consideration. In addition to these points, the inclusion of such isolated multi-fuel combustion systems, in which the original fuel constituents will mix only subsequent to combustion as exhaust products, under the banner of co-firing leads to multifarious "co-firing" systems, whose meaningful discussion lies beyond the scope of this thesis.

1.2 Introduction to Particle Combustion Modelling

The overarching aim of this thesis is to develop computational methods to model the co-combustion of pulverised biomass and coal. Commercial CFD software provides a platform for deployment of additional models and will assist in ensuring compatibility with other researchers' publications. In the past, intense effort has been focused on coal combustion modelling with much success, as illustrated by its incorporation into standard CFD software models. This represents a logical basis for the modelling of other solid fuels, such as biomass. However these existing models cannot be adopted directly, due to the fundamental assumptions in the models being compromised by pulverised biomass particles. The most notable is the assumption of a spherical shape for the aerodynamics, heat transfer and combustion models, by which biomass chips cannot meaningfully be represented. Upon deviation from a spherical shape, the computational particles no longer benefit from point symmetry so an orientation, which is itself a function of particle rotation, must be considered. Aside from this, significantly dissimilar moisture, volatile, carbon and ash content of biomass from coal (and between themselves) will yield heating/expansion and devolatilisation profiles which might

require additional stages to the standard coal combustion models (described in Section 2.3), which were developed from oil spray combustion in the 1990s. In this thesis, a complex heterogeneous combustion problem is described. In order to tackle such problems, a sensible approach is to begin with a section upon which subsequent models will find foundations. In this case the suspended particle transport modelling may be considered as stand-alone, as it is largely indirectly coupled to the temperature, and the experimental data for comparison are available at room temperature.

For the reasons outlined above, it was decided that the primary research area of this project would be the aerodynamics of non-spherical particles, focusing on cylindrical shapes to match the acicular structure of splinters caused by biomass grinding. Initially the more basic omissions from the standard models are to be investigated.

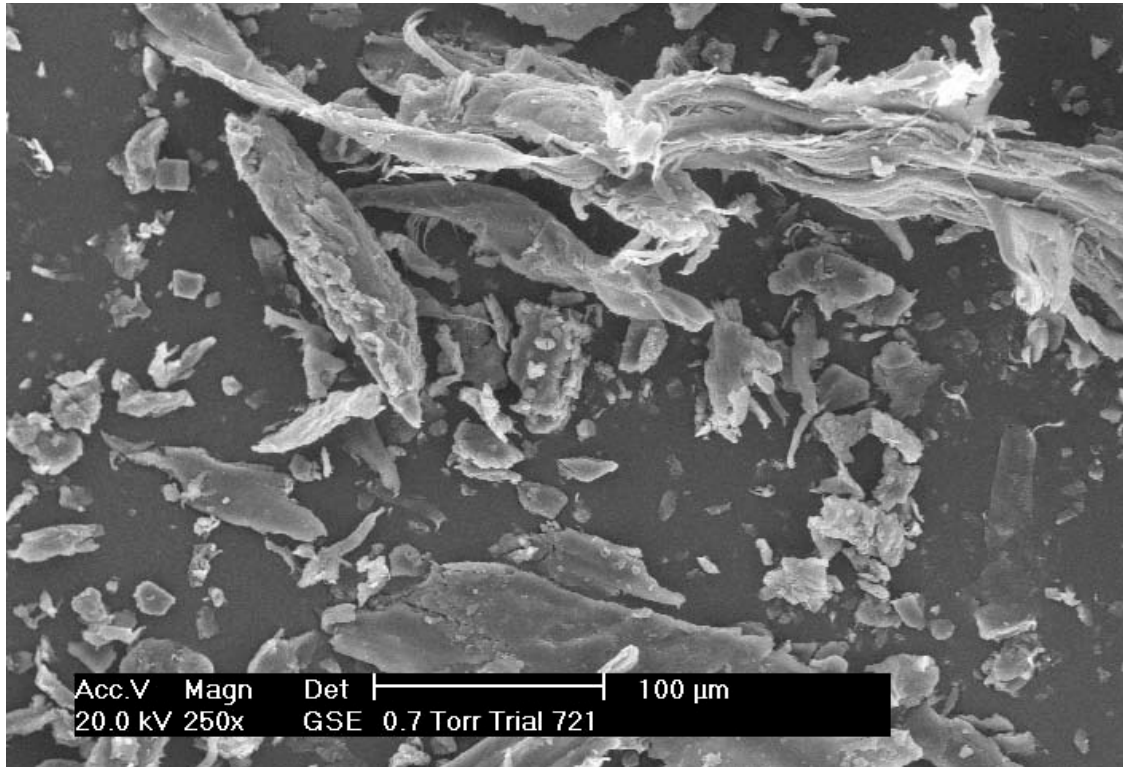
There are two major numerical methods for tracking the motion of particles, which are based on the Euler and Lagrange approaches. Both such methods were taken from fluid mechanics, considering the continuum as infinitesimal fluid elements, and adopted for discrete particle descriptions. Treatment of solid particles in the Eulerian model is as a volume fraction of an extra fluid phase, which shares the computational cell, modelled with a granular viscosity and different density. A set of all field variables, except the pressure, must be calculated for each phase. Each Eulerian solid phase is of identical particles (as aerodynamic effects upon the particles are on an averaged basis) requiring several phases to model even a coarse size distribution. As each phase requires a set of partial differential equations (PDEs) to be solved, this becomes impractically computationally expensive. Conversely, the Lagrangian model assumes particles are mass points of negligible volume, whose motion is described by ordinary differential equations (ODEs). This must be rationalised by a negligible total volume of such particles existing in any computational cell and therefore a dilute suspension. Nevertheless far greater freedom is allowed in the size distribution with this method at an acceptable cost, see Göz *et al.* (2004). Thus for low populations, simulation of the individual particles is possible. The latter, Lagrangian, method is most commonly implemented for coal particles since a wide distribution of particle sizes, which evolves, temporally, due to heating and burn out, is required. The particle surface area is of acute

importance in heat exchange and surface reaction predictions. Although not yet considered at this stage, the eventual cooperation of this model with combusting particles must be borne in mind. Also the volumetric concentration of solid particles that is expected to be transported by a gaseous carrier is assumed to be low, so the method is not invalidated by a dense concentration. Donea and Huerta (2003) also present the arbitrary Lagrangian-Eulerian (ALE) method, in which the frame of reference may move relative to the fixed boundaries and fluid flow. Following this discussion, the Lagrangian method is taken as the most appropriate for biomass and particularly co-firing due to the number of particle size classes that are required.

1.3 The Challenges

The challenges in the field of pulverised fuel co-fire modelling are threefold. They may be categorised as: measurement of salient properties and experimental results, understanding the chemical and physical processes, and selecting the appropriate level of modelling sophistication for computational effort. This thesis addresses the final category, modelling choices, but the decisions are limited and informed by the former. In particular the new models developed experimentally, in simplified systems, must be programmed and tested to determine their computational significance. However, verification and apportionment of weight between different modelling effects is obscured due to the uncertainty in experimental measurements.

Coal combustion modelling and simulation has received numerous investigations and is reasonably well understood (Williams *et al.*, 2000a). However, the simulation of biomass transport and combustion still presents challenges in that the particle aerodynamics may not follow the established assumptions for coal particles, due to the irregular particle shape. In addition the greater size may invalidate the assumptions of uniform temperature throughout the particle as well as the entire particle undergoing sequential combustion stages without overlap. These problems preclude simulation to estimate the very real physical effects of slagging and fouling and also the unburnt-carbon (UBC) in ash, which can translate to wasted fuel and worthless bottom ash. Figure 1.1 gives examples of the acicular morphology of fibrous biomass. Complicating matters is the vast array of materials under the label biomass and the very great variance



(a) Milled Wood



(b) Miscanthus

Figure 1.1 Microscopic images of some typical milled biomass particles.

within an individual species/product. Particle size and shape and the combustion and ash properties can change depending upon which parts of the plant are harvested, the climate, time of year, fuel handling and even the rate of milling.

1.4 Objectives

The aims for this thesis, arising from the previous discussions, are as follows:

- A* Examine the existing particle flow capabilities of ANSYS Fluent in reference to pneumatic pulverised fuel feedlines, respecting the expected air velocities, temperatures, mass loadings and geometries.
- B* Develop user defined codes for the omitted aerodynamic models that influence an individual particle, such as lift, non-spherical drag and wall collisions, and determine recommendations for new models based on predictive improvements and computational expense.
- C* Extend this type of aerodynamic examination to particles in a burner, considering three-phase flow (coal and biomass pneumatic transport) including inter-particle interactions and discuss the significance that the analysis has towards burner-exit combustion simulations.
- D* Investigate the combustion in a straw fired furnace. Experimental data has been made available by Prof Tan, Xi'an Jiaotong University, obtained at a 300MW_e power unit at Baoji Power Station, Shaanxi.

1.5 Outline of the Thesis

Chapter 1 presents a general introduction to the motivation for coal-biomass co-firing and the technical problems that arise. Chapter 2 is the literature survey for the particle aerodynamics modelling as well as coal and biomass/co-fire combustion. Chapter 3 introduces the theoretical basis of the computational modelling.

Chapters 4-6 describe the simulations of the experimental test cases, investigated. Chapter 4 evaluates the cold-flow behaviour of spherical and non-spherical particles in a pipe. Chapter 5 focuses on higher density particle concentration within a burner annulus and estimates the effect of the particle loading upon combustion. Chapter 6 presents the

simulations of a full scale pulverised coal furnace using pelletised straw in real co-firing trials.

Chapter 7 relays the discussion and conclusions from these investigations and suggests some possible future investigations.

Chapter 2

Literature Survey

This literature survey is split into three sections reflecting the emphasis of the thesis. The major component of the thesis is concerned with the behaviour of particles so the greater part of this literature survey is directed to that subject (Chapters 4 and 5). Sections 2.1 and 2.2 focus on spherical and non-spherical particle aerodynamic modelling, respectively. The second aspect of this thesis is that of the combustion of coal and straw particles (Chapter 6). Aspects of that and its development from coal modelling are surveyed in section 2.3, including non-spherical effects upon combustion. The accepted conventional representation of subsonic air as incompressible and ideal has been employed.

2.1 Multiphase Modelling for Spherical Particles

The sphere, being a highly pure mathematical volume (fully described by a single dimension with perfect symmetry about any plane through its centre) has received a vast amount of attention in particulate modelling since it allows simplifications in the theoretical and numerical models. It also aids experimental measurement, assuming particle orientation is unimportant and a simple method of determining the effective spherical diameter is available. However in a study of the lift force on spinning spheres, undertaken by Oesterlé and Bui Dinh (1998), it is suggested that greater confidence could be placed on their experimental results if it had been possible to measure directly the rotation, by optical means, of the spherical particles. This might be facilitated by the eccentricity in particle shape. Instead, this was deduced from the relative translational velocity of the particle and of threads coiled around an axel through the sphere transverse to the flow, with (experimentally ensured) fixed orientation through the particle's axis of revolution. An overview of the implementation of Lagrangian particle tracking precedes examination of non-standard particle models using the assumption of spherical shape.

2.1.1 General Method for Multiphase Modelling

In this section, Euler–Lagrange multiphase modelling, referring to the technique for the continuous and discrete phases respectively, is given a stronger foundation. The method is well defined, described in textbooks, and standard commercial software has default models based upon the technique.

The continuous phase field is generally represented by an Eulerian mesh of control volumes (CVs), meaning that the fluid flows through a stationary grid of cells, for which the variables are commonly calculated by the Reynolds-averaged Navier-Stokes (RANS) equations with partial differential equations (PDEs) solved using the finite-difference method (FDM) integration schemes. Large eddy simulation (LES) and direct numerical simulation (DNS) are other forms of the Navier-Stokes equations that simulate turbulent fluctuations (only of the large eddies for LES) as macro-scale fluid velocities. These respectively require reduced or no turbulence modelling (due to increased turbulence simulation) with respect to the instantaneous continuous phase momentum, giving greater accuracy. In LES the subgrid eddies (filtered as small) are modelled by RANS methods. However, due to the greatly increased computational effort for flow resolution, this method is only slowly adopted for engineering applications. In the context of computational fluid dynamics (CFD), simulation and modelling have distinct definitions: simulation refers to the solution of the spatially and temporally discretised PDEs, whereas modelling refers to other, generally algebraic, ad hoc calculations that apply to certain field variables. Modelling is less accurate but also less computationally expensive. Pertinent to the application under consideration, Chinnayya *et al.* (2009) employed LES to simulate particle dispersion numerically, by the macro-scale fluid turbulence and thus eliminate the requirement that one of the less accurate turbulence coupling models need be employed. An additional hybrid method is available to circumvent the full LES at its most costly, within the near wall region, in which the eddy sizes exponentially decrease so extensive grid refinement need be required for a sufficient proportion of the turbulent kinetic energy to be captured in the simulation. Instead, a RANS turbulence formulation, with more relaxed mesh size requirements, is used in the near wall region, earning the method the name ‘detached eddy simulation’ (DES) as this effectively treats the near wall turbulence as a subgrid to

the LES. The RANS equations contain more unknowns than their number since, by legacy of the ensemble averaging process, Reynolds stress terms are introduced. Therefore closure requires a turbulence model, see Hinze (1975). The Reynolds stress method (RSM) uses the Reynolds stress transport equations, although the cheaper (fewer equations) eddy/turbulent viscosity methods (TVM), which use an algebraic expression for the Reynolds stress in terms of an artificial ‘turbulent viscosity’ and known velocity gradients (Boussinesq hypothesis) are popular for simple fluid flows (ANSYS, 2009c).

For true Euler–Euler multiphase flows a complete additional set of RANS equations (except shared pressure) has to be solved with supplementary source terms included in (primarily the momentum) equations due to fluid interactions (ANSYS, 2009c). The alternative, as introduced in section 2.1, Lagrangian particle tracking method models particles as points of mass and samples the local carrier fluid conditions (at this point) from the Eulerian fluid field, described above. Turbulence coupling is introduced in the following section 2.1.2, however in the simplest (incompressible cold-flow) models only the averaged Eulerian continuous phase velocity at the particle centre is of importance. Position and velocity vectors, mass and variables relating to the particle’s virtual volume, such as diameter, are stored for each trajectory. In addition, each trajectory has a mass flow rate attributed to it as computational savings are made by reducing the number of tracked trajectories to fewer ‘representative particles’ with the assumption that a parcel of identical particles injected at the same point follow a single trajectory (Göz *et al.*, 2004). The particle and local field variables are used to calculate forces, via models such as the drag described in detail in the next paragraph, on the particle (in the general case no torque is involved as revolutions of the particle are ignored). Newton’s second law prescribes an ordinary differential equation (ODE) for the velocity of a point of mass (particle) from the non-equilibrium state of forces. By default, Fluent uses a switching mechanism to select a trapezoidal (linear two-step method) or implicit Euler (unconditionally stable) scheme depending on the requirement of second-order accuracy or large time steps (ANSYS, 2009c). An efficient multi-order Runge-Kutta method (RKM), which assesses the error of various steps in the RKM, in order to detect non-smooth responses and therefore select the highest

suitable order (Cash and Karp, 1990), has been incorporated for higher order integration techniques. Computational effort is saved by the imbedded lower orders as previously calculated gradients may be recycled. This method, where the drag of the particle is governed by the fluid momentum but the continuous phase calculations are oblivious to the particle's presence, is the most basic, one-way coupling, named for the single direction of the interaction between the phases. Kinetic energy, in the form of particle impulse, is effectively conjured within the system by the technique. Plainly this is not physically accurate and so can only be justified when the energy *ex nihilo* is insignificant compared to the total energy in the flow. One-way coupling is used under conditions of low mass loading, meaning the ratio of particle mass flow rate to carrier mass flow rate is low, as in dilute particle suspensions. In pneumatic transportation for pulverised fuel (PF) mass loading may exceed unity although volume loading will be around three orders of magnitude lower. The one-way exchange between the phases (including mass, momentum and energy) can be simply balanced by subtracting the source to one as a sink to the other, for momentum this will generally be a source to the particle and a sink to the fluid, resulting in two-way coupling. The individual calculations do not appreciably increase in complexity with this method. It is typical for the source/sink due to all particle trajectories through a cell to be stored during the Lagrangian particle tracking, and subsequently for the local sources/sinks to be exerted upon the cell centre calculation of the continuous phase. The difficulty arises because the particle phase now has an indirect influence upon itself, demanding an iterative process to allow the continuous phase to converge to the damped (or excited) state. The reduced expense involved may explain the popularity of one-way coupling in earlier papers (Oesterlé and Petitjean, 1993). Details of the components of the force balance will be introduced in Chapter 3.

The paramount quantity in the momentum calculations for particle aerodynamics is the drag force upon the particle. Clift *et al.* (1978) is the seminal text on this subject. The phenomenon is caused by the imbalance of hydrodynamic forces acting upon a particle's surface when it moves relative to the fluid in which it is immersed. A pressure gradient is developed across the particle due to the highly localised compression and expansion of the fluid as it flows around the surface of the particle. The resultant force

opposes relative motion. The drag upon the solid spherical particles in an ideal fluid is a highly researched topic with an accepted force equation. As the relative velocity increases, the boundary layer around the particle surface begins to be shed as a turbulent wake, altering the pressure field in the fluid and decreasing the specific interaction between the particle and fluid, appreciable as a reduction in the drag coefficient. However, the drag force itself continues to increase along with the velocity as it meets the fluid at a greater rate. This effect manifests itself as drag regimes in which the drag coefficient has differing behaviour. These are most commonly considered Stokes' (creeping) flow with transition into Newton's (ballistic) flow as they cover many engineering problems. The drag force presents, respectively, a roughly linear and square response to the relative velocity in the two regimes. In fact a supercritical regime exists at higher Reynolds numbers in which the drag coefficient drops further as the laminar boundary layers cannot form. Equations are postponed until the next chapter of the thesis, however Chapter 5 of Clift *et al.* (1978) gives a detailed account of the phenomenon.

2.1.2 Turbulence Coupling

As mentioned in the previous section, 2.1.1, the cheaper RANS form of the Navier-Stokes equations solves only the averaged flow field, and therefore a Lagrangian particle within such a flow field would experience no turbulent fluctuations (affecting the local pressure). This is in contrast to LES or DNS in which turbulent fluctuations would be picked up by the relative velocity for the drag between the phases and instigate particle dispersion without the need for modelling (Chinnayya *et al.*, 2009). In some investigations it is assumed that no special coupling of the fluid velocity fluctuations, due to the turbulence, to the particle phase need be made (Yasuna *et al.*, 1995, and Yin *et al.*, 2004) as the intensity of the random velocity is assumed to play an insignificant role in inertial particle drag. Therefore in such simulations only the average continuous phase velocity has any influence upon the particles. In a congruent manner to the average flow drag model, described in the previous section, 2.1.1, the fluid turbulence can be one-way or two-way coupled to the particle motion, the latter being called 'turbulence modulation' (Laín *et al.*, 2002, and Saffar-Avval, 2007). For

simplification, dilute system two-way turbulent modulation is often neglected (Lun and Lui, 1997, Minier and Peirano, Chapter 7, 2001, and Sommerfeld, 2003).

Attempts to introduce the effect of carrier flow turbulence upon the particle phase through modelling have been published in the literature, and some additional models necessary for a RANS fluid field are available in standard commercial software (Rosendahl, 2000). These are incorporated into the drag with the instantaneous Eulerian fluid velocity predicted for use in the same equations. Patently the real instantaneous fluctuation is lost to the averaging process and so the fluctuation intensity is sampled stochastically. The simplest stochastic velocity method is the discrete random walk (DRW). In DRW the instantaneous fluid velocity is predicted based on the averaged RANS field velocity plus a stochastically determined value sampled from a Gaussian distribution of standard deviation equal to the root mean square (RMS) of the time averaged Reynolds stress. For the Reynolds stress transport turbulence closure, this standard deviation may be anisotropic (a vector in three dimensions). For the TVM an algebraic expression is used to translate the eddy viscosity closure parameters into an isotropic Reynolds stress, nonetheless random Gaussian numbers are obligatory for each component, regardless of the same standard deviation of velocity fluctuation being present in all directions. The instantaneous fluid velocity alters the drag magnitude and direction experienced by the particle, and remains constant throughout the particle's interaction with a particular eddy, whose 'life time' is stochastically sampled from statistical properties of the experimentally determined Lagrangian integral time scale coefficient. In addition to this it is common to model the 'cross over effect', named for the phenomenon of the particle crossing over (traversing) the eddy. This is where the relative velocity between the particle and the fluid (eddy velocity) is high enough for the eddy residence time to dip beneath the 'eddy life time' and therefore supersede the 'eddy life time' as the limiting factor for eddy interactions. The overall result is that the instantaneous velocity will fluctuate more frequently which would suggest a smoother average velocity and therefore decreased dispersion. A closely related method, to the previously defined DRW, is the continuous random walk (CRW) (Bocksell and Loth, 2001). The general application of this model exploits a Markov chain, whereby only the present state is used to yield a continuous fit between the new stochastically established

and the current instantaneous velocities, with re-evaluation of the random terms at every time step. In addition Bocksell and Loth (2001) make mention of an alternative with a greater sympathy to the particle's trajectory history.

2.1.3 Additional Models

The omission of particle rotation and inter-particle collisions from the standard Lagrangian discrete particle model might be acceptable in the general case, however a number of authors have investigated the implementation and effect of their inclusion. (Oesterlé and Petitjean, 1993, Yasuna *et al.*, 1995, Lun and Lui, 1997, Yilmaz and Levy, 2000, Sommerfeld, 2003, Saffar-Avval *et al.*, 2007, and Laín and Sommerfeld, 2008). There are certain known and theoretically formulated phenomena mentioned in the literature, but these have unanimously uncontested assumptions of insignificance for the relevant application (considering the solid to gas density ratios or individual particle masses that will be present in PF transport modelling). Brownian and thermophoretic forces are assumed negligible compared to the particle inertia of hyper-micron dimensions (N.B. thermal effects are not considered in this section so there are no thermal gradients to exert a thermophoretic force). In addition the 'virtual (or added) mass' and 'Basset history' terms due to the additional mass of the fluid displaced by the particle and the fluid viscosity, respectively, are ignored, since the solid phase is over 1000 times the density of the gaseous carrier, in the case of high rank coals. These have all been disregarded in subsequent discussion within this subchapter, however there is an indication that virtual mass is of importance for biomass and so is included in some non-spherical studies that are reviewed at a later stage. Similar arguments have been given for the abrogation of the lift models (Bocksell and Loth, 2001), however a more in depth consideration of this is discussed in section 2.1.4.

2.1.4 Spherical Lift

Lift is introduced to the simulations simply as additional forces at the particle centre to be appreciated during the force balance. These supplementary calculations will be cheap algebraic evaluations (Magnus lift force requires particle rotation) in addition to the pre-existing ODE. Although the lift force is traditionally thought of as being perpendicular to the drag force, which is itself parallel to the relative motion of the fluid, since merely the resultant of the force balance is desired, individual vector components of both drag and lift (in the Eulerian coordinate directions) are calculated. There are two accepted lift forces that are frequently modelled, the Saffman (or shear) lift and the Magnus (or rotation) lift, named after their early investigators (or the cause of the pressure gradient which induces the lift). The lift coefficient's dependence upon the Reynolds number of the particle, Re_p , must be respected, which will depend upon the relative velocity magnitude rather than that in any particular component direction. Also in the case of the Saffman lift, in three dimensions, the root of the resultant fluid angular velocity magnitude must be calculated and the correct componential value substituted back by the use of a unit vector of the angular velocities. Taking the square root of the components on an individual basis will not represent the non-linear relationship. In two dimensions, there is only a single relevant angular direction and so taking the root of this component is equivalent to taking the root of the magnitude and multiplying by the directional unit vector.

Many authors take the lift to be negligible (Pelegrina and Crapiste, 2000, Bocksell and Loth, 2001, Laín and Grillo, 2007, and Vreman, 2007). Dobrowolski and Wydrych (2007) assess the drag, gravimetric and lift contributions within their numerical simulations of a pulverised fuel feedline system including multiple elbows, specifically to calculate wall erosion, and conclude that the lift force never surpasses 1% of the total force. While this is a reasonable justification for exclusion, the elbow test case, from horizontal to down-flow, does not appear to be representative of the main test geometry, in which the flow is predominantly slightly positively inclined and has long (normalised by elbow radius) straight sections. In addition, inter-particle collisions are not mentioned in the paper despite their intentions to model wall erosion, the observation of

roping and local regions of elevated particle-wall collision frequency imply high particle concentration. The conditions under which the lift is assessed are critical for the applicability of the judgement for its omission. Due to a possible synergy between the lift and other effects (such as collisions) or an inequality of flow changes (reduced drag relative to lift), in scale up from a single particle model the lift may become significant in practical cases whilst remaining inconsequential for the test. Somewhat less commonly only one of the lift forces is considered, this practice is followed by Yilmaz and Levy (2000) and Pirker *et al.* (2009). Also, quoting Saffar-Avval *et al.* (2007), “Cao and Ahmadi [1995] concluded that the rotational energy of particles is less than 10% of their translational energy even in the case of dense granular flow. Therefore in the present case of relatively low solid volume fractions, the effect of particle rotation and Magnus lift are neglected.” It is important to note that all four recently mentioned studies (Yilmaz and Levy, 2000, Dobrowolski and Wydrych, 2007, Saffar Avval *et al.*, 2007, and Pirker *et al.*, 2009) were concerned primarily with vertical apparatus. Investigations of horizontal transport afford lift force a greater significance as it may assist in the suspension of particles when gravity is acting normal to the flow (Laín and Sommerfeld, 2008). Lun and Lui (1997) found the Magnus lift to be important due to the rates of rotation as a consequence of collisions and that these are critical to particle suspension.

The physical phenomenon of lift is as a consequence of a pressure gradient across the particle, which is in turn bound to the localised fluid velocities at the particle surface. This induces local potential flow which may entrain the particle. Any such motion is damped by the particle inertia so significant lift is only considered if the relative velocity variations are strong and polarised. These pressure conditions can be resultant from the previously introduced lift modes, shear and rotation, and are presented in Figure 2.1. This is because regions of high shear will naturally present a velocity gradient across the particle, due to fluid viscosity, as laminae closer to the wall will have decreased velocity. From Bernoulli’s Principle, a lower pressure is present at the top surface of the particle in Figure 2.1(a) than at the bottom, due to the greater relative velocity. The solid surface supports this stress in the fluid and therefore an acceleration is induced. Instead the fluid velocity might be considered constant but the

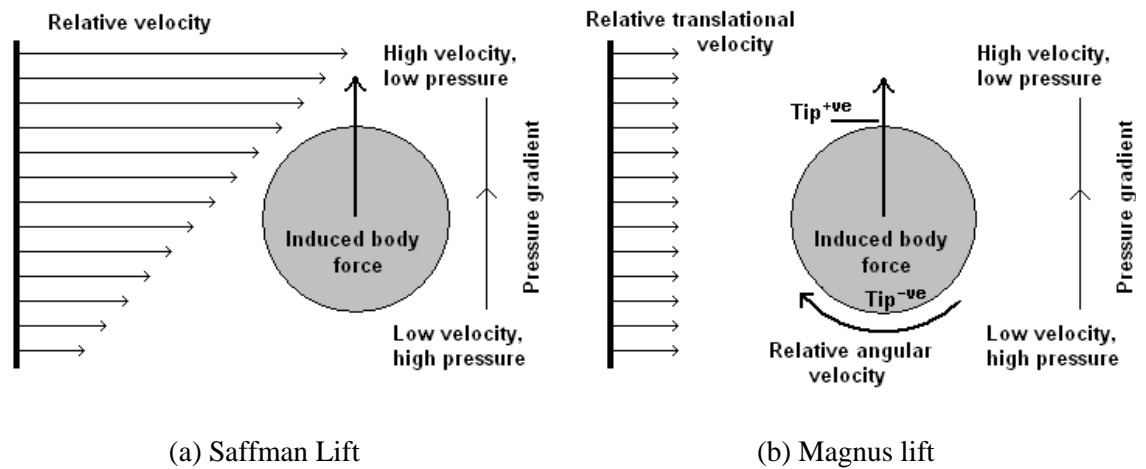


Figure 2.1 Diagram of lift modes

rotation of the particle will skew the relative velocity. For example, at the particle tips, the points on the surface at which the tangent is parallel to the relative translational velocity when observed along the axis of rotation, the relative surface velocity will be the sum for one, and the difference for the other, of the relative translational velocity and the relative angular velocity times radius. This is seen in Figure 2.1(b) where a greater relative velocity is present above the particle, as the particle surface meets the relative velocity with a negative component parallel to the relative velocity, therefore the relative velocity between the fluid and an instantaneously stationary particle surface is increased, whereas the reverse occurs at the lower surface. Remember the relative angular velocity is that of the fluid about a stationary particle. Induction of motion parallel to the pressure gradient within the fluid is due to the same process as before. In particle dynamics the direction of Magnus lift is the relative velocity cross the axis of rotation. No confusion should be caused when other applications, particularly sport, consider a particle, given impulse, moving through a quiescent fluid due to inertia and record the particle velocity rather than relative velocity. The two velocities have opposite direction and so in different situations the reverse cross product may be seen. Physically, the particle is entrained along a single instantaneous pressure gradient, but the phenomenon is decomposed into two independent forces, numerically. With meshed

particles in a DNS, the actual local conditions might be captured, however, to allow a reasonable calculation time, in practice these effects are modelled.

2.1.5 Spherical Rotation

In numerical Lagrangian particle physics the calculated acceleration is assumed constant, throughout the timestep, until the next force balance. To incorporate particle rotation into this, torque balances must also be conducted. The particle rotation can be influenced by the fluid phase in a similar manner to translation, such as angular drag and instantaneous relative angular velocity due to turbulent fluctuations, through tangential forces at the surface of the particle in a laminar boundary layer or turbulent wake.

An empirical fit, analogous to the Schiller-Naumann drag law equation [3.22], is presented by Laín and Sommerfeld (2008) for particle coefficient of rotation C_R , equation [3.49]. The basic torque expression and the coefficient of rotation, under creeping and spinning flows were presented by Rubinow and Keller (1961) and Dennis *et al.* (1980), respectively. These were recast into the authors' rotating Reynolds number, Re_r , taking into account the relative angular velocity of the fluid and sphere. An identical method was proposed by Lun and Lui (1996) but this considered only the angular Reynolds number coefficient of rotation fit by Dennis *et al.* (1980), and adopted the same authors' characteristic length (a , particle radius) for their 'spinning Reynolds number' (Re_ω). Due to Laín and Sommerfeld's (2008) choice of particle diameter, d_p , as the characteristic length, also chosen in this study, under the same conditions there exist the relations: $Re_{p(L\&S)} = 2Re_{p(D)}$ and $Re_{r(L\&S)} = 4Re_{r(D)}$. Where the subscripts dictate the authors, $_{(L\&S)}$ for Laín and Sommerfeld (2008) and $_{(D)}$ for Dennis *et al.* (1980). This leaves confusion as to how Laín and Sommerfeld (2008) set the Re_r boundary ($Re_r \leq 32$) for the use of the Dennis *et al.* (1980) rotational drag law which uses $40 \leq Re_{r(L\&S)} < 2000$ but is primarily based on the range $100 \leq Re_{r(L\&S)} < 200$.

Rotation can also be induced during inter-particle and wall collisions, as the relative force of impact is decomposed, into a radial translational force through the centroid and tangential force at the particle surface, in other words a torque about the centroid of the sphere. In the majority of investigations, in two-dimensions, only

rotation about the normal to the plane is considered, this prevents induced translational motion at the particle's surface or Magnus lift forces (see the previous section, 2.1.4) in the third direction, that is not simulated. The number of rotation parameters to be calculated, for rigid bodies, quadruples in 3D space since any line connecting two points may rotate about three independent axes and this line may describe a particle's axis of revolution. Despite the somewhat onerous computational toll, 3D rotation of non-spherical Lagrangian particles has been performed by Yin *et al.* (2003) and Yin *et al.* (2004) using the vectrix method of Hughes (2004). Rotation is, without exception, calculated for the use of a Magnus lift model. Its direct effects are as a fluid momentum sink and irreversible losses through inelastic collisions between particles and at the wall, akin to the translational motion. If collisions are frequent, translational to rotational kinetic energy conversion may be significant in its own right. However this is not discussed in the literature.

2.1.6 Spherical Inter-Particle Collisions

The statement of dilute volumetric concentration is usually regarded as licence to neglect inter-particle collisions, as in Yin *et al.* (2003), Göz *et al.* (2004), Yin *et al.* (2004), Ku and Lin (2008), and Wang and Yan (2008). Besnard and Harlow (1986) quantify dense concentration by expressing the threshold of significance for inter-particle collisions at a volume ratio of 0.2, this corresponds to a mass loading of greater than about 200 for bituminous and anthracitic coals, which is far removed from the operational loads in pneumatic feedlines. Contrary to these Lin and Lui (1997) state, "*For dilute systems with solids volume fraction of the order 10^{-3} [coal mass fraction ≈ 1], inter-particle collisions are found to be crucial in sustaining a steady and fully developed suspension in the horizontal channel.*" Pirker *et al.* (2009) agree that inter-particle collisions are insignificant in dilute suspensions. However this is qualified by referring to the local instantaneous concentration rather than the nominal inlet condition. In addition, Yasuna *et al.* (1995) concluded that inter-particle collision is an essential mechanism for the production of a pressure head.

A study of the flow of a pneumatic suspension of spherical glass beads through a simple horizontal rectilinear channel was undertaken by Laín and Sommerfeld (2008) as

a continuation of earlier work (Laín *et al.*, 2002) employing what has been called ‘four-way’ coupling, meaning two-way coupling of both momentum and turbulence. The method of inter-particle collision modelling used assumes an instantaneous binary collision between particles of a similar size (neglecting fluid phase interaction during collision), detected by stochastic sampling from a statistical probability of collision. This is estimated from the kinetic theory of gases (Sommerfeld, 2001) by way of the treatment of a system of suspended particles as molecules of a gas. At each calculation step a stochastically prescribed “collision object” (characteristic local particle) is provided for which a probability of collision by the tracked particle (potential collision subject) can be made. Relevant particle variables are stored in the Eulerian fluid cells as if they were field variables so that they may be accessed by the Lagrangian particle during trajectory calculations. The method has been applied to a monodisperse particle suspension and so only the velocity of the collision object, in addition to the local particle concentration, must be recorded. In addition the size and density of the particles is necessary for the calculation of collision probability but this is known *a priori*, or could be taken from the tracked particle.

Rotation of the particles during collision was ignored in the method described above (Sommerfeld, 2001). However an indistinguishable probabilistic collision method, satisfying particle rotation, was developed, and similar experimental suspensions observed, by Oesterlé and Petitjean (1993) as it was expected that the Magnus lift force would prove significant due to collision induced rotation. Magnus lift (section 2.1.4) is used to explain the raising of the maximum particle concentration, in the measured profile, off the lower wall for a mass loading of 10. When discussing the reasons for the maximum concentration, at a mass loading of 20, to return to the lower wall, Oesterlé and Petitjean (1993) honestly state that, “*No satisfactory explanation can be proposed for the moment.*” However it appears to be possible that the additional momentum, sunken from the continuous phase, and turbulence modulation caused by increased particle collision frequencies would reduce the transport efficiency of the flow. No carrier fluid velocity results are present and only one-way coupling, which would be unable to capture this effect, was included in the numerical model, which the authors concede is inappropriate for such high mass loadings. An alternative or

compounding cause might be that high frequency inelastic collisions absorb the angular momentum of the particles and therefore inhibit the lift.

Bearing in mind the common practice of lumping particle mass into representative trajectories, some discussion considering this fact is of value at this point, since the assumption becomes questionable for coarse particle streams (a large proportion of the mass flow rate is attributable to a single particle trajectory). When a collision occurs, the whole flow rate of the stream must follow the same post collision path, for the standard coding mechanism. Physically, for steady discrete phase model (DPM) calculations, this represents a stream of particles, of which every member receives a step change in momentum at the same position in space. This in itself is intuitively false, however is mathematically justified by other particle streams continuously delivering the correct momentum to this balance. The contested assumption that the “static mass” (that is the Eulerian mass of particles that would be present in a computational cell due to steady Lagrangian flow rate through the cell) can readily supply the reacting impulse to the stream, so that this momentum strain is negligible, requires that the flow rate in the colliding stream is much less than the total through the cell. An alternative perspective is that the “static mass” must be refreshed rapidly relative to the rate of momentum interaction from the colliding stream which would otherwise disperse it. For increasingly coarse equal mass rate trajectories the ratio of flow rate between the colliding stream and the “static mass” will approach unity. The steady state calculations are repeated using the local particle field of the previous step until a converged flow field is found. A greater number of trajectories will promote a smoother distribution of local mass amongst the cells. This is desirable as these calculations are ever intended to emulate the condition of individual particle trajectories at an acceptable cost.

The stochastic method, previously discussed (in this section) is a practical method for sequentially tracked particles, which grant a reduced memory requirement, although warning is given for its use in conjunction with the parcelling of “characteristic particles”. For both stochastic models described, it must be noted that the entire parcel collides or continues so a larger number of trajectories may be required. The method is also influenced by the determination of relative velocity between the colliding particles. Sommerfeld (2001) takes into account the velocity correlation between the two

colliding particles due to turbulence (that is a proportion of both the collision object's and collision subject's random components of instantaneous velocity are equal to each other, based on the Stokes number, St). The rationale is that colliding particles are in contact so would inhabit the same eddy, whereas Oesterlé and Petitjean (1993) only considered the average velocity of the collision object, which would tend to overestimate the relative velocity of collision. Turbulence coupling has been fully explored in an earlier section 2.1.2. In addition the numerical testing of these stochastic collision models was undertaken on simple geometry, i.e. horizontal pipe/channel and in Sommerfeld's (2001) case a monodispersion in only two dimensions. Therefore the true computational expense of the models is not realised. For general engineering situations Pirker *et al.* (2009) express that the above method is too costly.

Although not compared to a non-colliding particle case, directly within the publication, Laín and Sommerfeld (2008) conclude that the inter-particle and particle-wall collision models play essential roles in the particle profile prediction. Inter-particle collisions are shown to have an impact upon the strength and frequency of wall collisions. However the relative effect of wall collisions becomes more dominant with increasing wall roughness. In addition, the fluid pressure drop is governed by the wall collisions since the fluid turbulence and particle kinetic energy dissipation at the wall are the only horizontal momentum irreversibilities of the system. This is not surprising when it is considered that only the time averaged carrier flow velocity (horizontal direction) is coupled to the particles and the drag exerts only a longitudinal force. Saffar-Avval *et al.* (2007) used a different inter-particle collision mechanism to Oesterlé and Petitjean (1993), and Laín and Sommerfeld (2008) but from the same fundamental theory (of kinetic gases), the 'hard sphere' model of Crowe *et al.* (1998). A point is made of this being a deterministic approach, meaning that instead of a statistical probability of a collision being calculated: the displacement between each Lagrangian particle (point of mass) and every other particle is compared to the sum of the pair's radii. If the particle centres are closer than this value then a collision occurs. The relative velocities and angle of collision are then readily available. This DNS of the Lagrangian phase clearly handles a full size distribution. However, the necessity for simultaneous particle tracking, with particle time steps to yield discrete displacements

in the order of the particle diameter (time steps are limited to permit displacements of only a fifth of the particle diameter by Lun and Lui (1997) to appropriately resolve particle volume overlap), precludes its use in engineering applications for fine powders. An additional consideration of Vreman (2007) for the 'hard sphere' model is an 'inter-particle drag' parameter which models the particles' influence upon each other via boundary layers in the carrier fluid but without actual collision. However, its expense and insignificant effect upon the particle motion, for the high density ratio of the discrete to continuous phases in the study (glass and air), are also described.

As reported earlier in this section, stochastic collision prediction of the tracked Lagrangian particle with sufficient particle load resolution (fine lumping of the total mass of the particle phase into many streams) with polydisperse sizes, through complex 3D geometry and particularly with regions of dense concentration may prove preclusive in computational expense. In the numerical study of cyclone separators, for example, in which very high particle concentrations occur near to the wall, a less computationally expensive alternative is sought (Pirker *et al.*, 2009). It is relayed that former publications, unavailable for cross reference, have suggested novel hybrid solutions (Pirker *et al.*, 2009), in which the particulate phase is modelled by both Lagrangian particle streams and Eulerian phases, either in partitioned regions of the fluid depending upon particle concentration or synchronously within the whole of the fluid domain. In this latter method, the Lagrangian phase is coupled to the Eulerian particle phase by a force indicating the average collision direction arising from the Eulerian gradient of the granular pressure. The method described in Pirker *et al.* (2009) leaves the majority of the particle modelling in Lagrangian terms, such as drag, lift, rotation and most notably wall collisions, however expediently generates the local average particle diameter for use within the current cell by the Eulerian monodisperse particle phase. The continuous multiphase continuity and momentum equations for the Eulerian gaseous and particle phases are calculated to determine the Eulerian particle velocity from which an inter-particle drag force is translated back to the Lagrangian stream. As the Eulerian and Lagrangian particle phases have coupled momentum by this method, the convergence criteria for the flow are based on monitors of global performance. Mention must be made that only the averaged effect of collisions, whereby the particles tend to diffuse

from high concentrations, is captured by this method, however Pirker *et al.* (2009) do not attribute inaccuracy to this fact.

2.1.7 Spherical Wall Collisions

Despite similarities in the impulsive transfer present in both inter-particle and wall collision models, the numerical handling is quite different. However, notation is borrowed from the previous section 2.1.6, on inter-particle collisions. Due to rigid body motion (or more commonly, quiescence) of the walls and the fair assumption of infinite inertia ratio between wall and particle, more sophisticated models remain less computationally expensive, as does deterministic collision event detection, for the case of tracked Lagrangian particles colliding with a solid boundary. With stationary walls, relative velocities are simply those of the colliding particle. Particle-wall collisions are a primary additional source of momentum loss from the suspension system due to particles, representing additional pressure head on the fluid flow (Tsuji *et al.*, 1987, Oesterlé and Petitjean, 1993, Sommerfeld and Huber, 1999, Laín *et al.*, 2002, Saffar-Avval *et al.*, 2007, and Laín and Sommerfeld, 2008). Although some kinetic energy loss to thermal could occur through fluid-particle and particle-particle interactions, these are largely reversible momentum exchanges. The full wall collision mechanism is not described in the ANSYS Fluent User's Guide, however simple investigation (extremely dense particles colliding with a wall in quiescent inviscid fluid) yields the following, numerical collision events are detected when a particle (centre) crosses a fluid cell face which is connected to a wall zone. The tolerance associated with the location of the wall surface can be of the order of a PF particle diameter (10^{-4} m), therefore overwhelming any inaccuracy of particle position, in the wall normal direction, caused by allowance of half the particle to enter the wall before collision detection. For a shallow impact angle, that between the particle's velocity direction and the wall's tangent, this same limitation of detection would cause significant postponement in the triggering of a collision, in the wall tangential direction. However, the tangential location of the collision becomes infinitely dependent upon the wall position tolerance for impact angles approaching zero. The actual normal displacement between the collision and wall is dependent upon the particle's path with no observed effect attributable to the computational cell size, the

particle's diameter or step length of the calculation updates. Given that the dimensions of a walled domain are indeed far greater than those of a particle, for which the mechanism is designed, and the probability of an impact angle follows its value as this descends to zero the simple boundary check method is vindicated by its low computational cost. The wall collision models, available to standard software, that are triggered by the catch described above in this section, enable only coefficients of normal and tangential restitution's dependence upon the impact angle by a piecewise polynomial fit. (This enables a single set continuous function, constant values or a linear distribution, as 0th or 1st order polynomials). More advanced models also exist in ANSYS Fluent, but are intended for fluid particles (Wall Jet and Wall Film models). This method, perhaps too simplistic to be called a model, of directional restitution coefficients omits the tangential restitution's coupling to the normal velocity, due to wall friction, and particle rotation entirely, but benefits from easily measureable empirical constants. As an aside; it is possible to set boundary conditions for wall roughness parameters, however these are to supplement the fluid turbulence model and play no role in collisions.

Description of the velocity restitution by momentum balance equations rather than simple parameters will provide advanced wall collision modelling. Tsuji *et al.* (1987) present the combination of restitution and friction (Coulomb's law) in momentum conservation equations to determine post collision normal and tangential velocities as well as the angular velocity about an axis perpendicular to both translational velocity components, from their pre-collision counterparts and empirical coefficients of restitution and friction. Corresponding to the inter-particle collision model (section 2.1.5), "instantaneous" collisions are assumed meaning that the reactant force upon a colliding particle is exerted over a negligible length of time in comparison to the particle relaxation time so that hydrodynamic forces play no part during the rapid momentum exchanges.

A two dimensional experimental analysis in which a single plane is illuminated by a pulsed 'light sheet' is used to measure the rebound parameters demanded above (Sommerfeld and Huber, 1999). This method records collisions in the plane via multiple optical images, whose length of exposure causes the reflections from particles, in the

pulsing light sheet, to form streaks. The experimental method of Sommerfeld and Huber (1999) has no strategy for angular velocity measurement, however it is used only to obtain empirical values (of restitution and friction) and all velocities are determined on a theoretical basis. In addition to the impulse equations, Tsuji *et al.* (1987) suggested an augmented impact angle below a shallow threshold (7°) presented in an earlier paper, as clarified in Sommerfeld and Huber (1999). This solely deterministic approach effectively models perfectly smooth walls, where the evaluation of the function of impact angle yields a single result. The effects of roughness are represented only by the empirical restitution and friction parameters. More realistic spread due to wall roughness might be obtained by stochastic means.

The preceding discussion uses empirical parameters which are therefore correct for only a single material and roughness pair or for the average of a distribution. A supplementary reason for stochastic wall roughness modelling in horizontal conveying of solid particles is as an aid for suspension (Matsumoto and Saito, 1970) wherein other physical phenomena have been truncated from the numerical representation. Consider an horizontal gravimetric suspension system with perfect smoothness of both spherical particle and bounding wall, and neglecting turbulent dispersion and lift forces upon the particle. For any practical situation, the coefficient of normal restitution will be less than unity and the fluid flow in the normal direction will be negligible compared to that perpendicular. Therefore gravity induced wall collisions will exponentially decrease the maximum vertical velocity, concluding with zero vertical velocity and elevation. Inclination of the wall, at a microscopic local position of collision, effectively resolves the global normal and tangential components at an angle, whereby some of the particle's tangential momentum, that may be recovered due to particle drag, can be deflected into the normal direction. Matsumoto and Saito (1970) introduce a stochastic method by which the wall roughness is modelled as a sinusoidal wave. A spherical particle is assumed to meet the wall at a random phase offset of that sine function, uniform random number of interval $[0, 2\pi]$, from which a variation in local wall normal can be obtained. The amplitude and period of the sine wave would be related (through equality) to the roughness height, H_r , and cycle length, L_r , respectively (which are the average peak height and peak interval in the surface roughness). However this spherical particle

wall collision model was developed from experimental work on ellipsoidal particles colliding with a smooth (glass) wall within an earlier publication from the same authors (Matsumoto and Saito, 1970). Therefore the “roughness” is inversely traced from the circumferential eccentricity of the ellipsoid to the wall, this fact reiterated in Sommerfeld (1992), and here the rationale for the sine function becomes clear. The rigours of computing the time dependent ellipsoid orientation deter the explicit calculation of this parameter, leading instead to its being modelled by a random $[0, 2\pi]$ orientation at the wall. In this analogous consideration, of a particle with an elliptical circumference colliding with a smooth flat wall, a ‘shadow effect’ (Sommerfeld and Huber, 1999) may be introduced. Manifest as the distribution of contact probability across the particle surface due to rotation, the ‘shadow effect’ skews the uniform probability of a sphere for particles with an aspect ratio greater than unity. The leading edges, with respect to the rotation, near the ends of the semi major axis will have greater probability of collision. At each end of the semi-major axis, the surface normal is radial from the particle centre, the leading edge is marked by its possession of a tangential component that shares direction with that of the instantaneous translational velocity of the end of the semi-major axis due to rotation about the particle centroid, whereas the tangent to points on the trailing edge will be in the opposite direction. However the probability distribution of the collision patch is not taken into account by Matsumoto and Saito (1970) as the random number describing the roughness phase is sampled from a uniform interval. The ‘shadow effect’ will be re-examined in terms of the general roughness model later in this section.

In order to capture the random result of wall collisions, Tsuji *et al.* (1987) adjusted their deterministic inclined wall model so that the augmented angle would contain a stochastic component, selecting the form of a coefficient and exponent to the random number. These were tuned iteratively by comparison to the experimental results. The model was subsequently adopted by Sommerfeld (1992) but with the threshold angle abrogated so that a stochastic wall inclination is applied for all collisions. Furthermore, methods of randomisation of the ‘virtual wall inclination’ are compared, direct sampling from uniform or Gaussian random number (the selection of interval properties is based on wall roughness and will be described below) or that of Matsumoto and Saito (1970),

outlined earlier in this section, to determine which results in the most appropriate probability distribution of apparent normal restitution coefficient (global normal direction). In these numerical studies the local coefficient of restitution, at the micro-surface of the rough wall, was taken from an empirical cubic fit, with the true reflection angle (in the local coordinate system) as the independent variable. The actual roughness surface inclination angle is determined by adding a stochastic element to the global impact angle. The computational mechanism applied to control this random angle generation depends upon a theoretical maximum angle, γ_m , the greatest inclination that a local facet of a rough surface may assume relative to the global tangent, which is itself composed by the measured surface roughness with the parameters previously identified within Matsumoto and Saito (1975), namely the average roughness height and cycle length (H_r and L_r , respectively). A simple trigonometric analysis of the idealised (average peak values) roughness system yields different results for γ_m , depending on the relative scale of the particle and roughness. Particles of smaller diameter than the roughness cycle can penetrate the 'roughness valleys' finding access to more sheer faces, whereas the angle observed by particles greater in size is limited by the interference of preceding peaks. Clarification is best found in the diagram presented by Sommerfeld (1992, Fig.2, p909). The random number intervals used in the first two test cases therefore used positive and negative limits of magnitude, γ_m , the maximum angle, for the linear distribution and a zero mean with the maximum angle as the standard deviation for the normal distribution. The experimental data of the global normal restitution examined, as presented in Sommerfeld (1992), shows smooth symmetric Gaussian bell curves of restitution coefficient. The test is performed at 20° and 45° angles. A broader range of probable normal coefficients of restitution is measured for the more acute impact angle, from zero to above unity, whereas the narrower range at 45° has a 99% confidence interval of below 0.7 (approximately). As might be expected, the Gaussian virtual wall inclination distribution best recreates the Gaussian distribution trends in the normal coefficient of restitution, with similar means to the numerical and experimental restitution curves, at least as may be appreciated through graphical means. What is surprising is that the somewhat arbitrary designation of maximum angle as the standard deviation for the stochastic virtual wall inclination closely reproduced the

range of restitution coefficients for the lesser angle (20°), but a narrower range was identified for the (numerically determined) coefficient of restitution range for a 45° global impact angle. The distribution of coefficients of tangential restitution is also provided for this Gaussian random roughness angle case, the match to the experimental data is poorer than in the normal case with two discrete probability curves occurring for the 20° impact angle. This results from a shift between sliding and non-sliding collision conditions that is dependent upon the random angle. The base impact angle plus 1.5 times the nominal maximum virtual inclination is at the limit of the sliding condition (29°), therefore only angles varying from the mean by greater than one and a half positive standard deviations ($<7\%$) should be in the lower restitution group, this is difficult to assess visually. For 45° , all collisions will be non-sliding due to the relative strength of the normal velocity component. At this point it is of substantial value to mention that all numerical studies performed by Sommerfeld (1992) assumed irrotational particles, this condition could not be enforced in the experiments, and results in constant, spatial, particle velocity at different points on the particle surface and that only translational momentum is transferred during collisions. The assumption in the numerical investigation gives rise to a constant coefficient of rotation under non-sliding conditions of 0.714 in the local tangential direction, and therefore the distribution of global tangential coefficient of restitution is entirely due to the local normal restitution's dependence upon impact angle and the resolution of the resultant restitution path (in the direction of reflection) into global coordinates. This reveals a strong relationship between global restitution and the constraints set on the random virtual inclination, the conclusion being that a more accurate determination of the probability density function (PDF) for virtual wall inclination is required with a dependence upon the global impact angle. Also the expectation is that empirical parameters for given particle sizes and particle-wall material pairs would lend greater accuracy than modelling based on averaged roughness values.

In answer to these requirements, the roughness heights on a stainless steel surface sampling at spatial intervals representative of the particle size were measured by a depth probe. From this a PDF of the linear inclination between pairs of roughness height recordings could be generated for a particular particle size as presented by Sommerfeld

and Huber (1999). Additionally, the shift in distribution as a consequence of the ‘shadow effect’ is imposed upon the absolute roughness angle PDF by calculation of the effective mean and standard distribution multiplying the individual probabilities by a factor based on the normalised projected area that would be presented by a plane inclined at that angle, resolved in a perpendicular direction to the impact direction. This reflects a dependence upon impact angle. Plainly, if the virtual wall inclination is more steeply negative than the global impact direction the local impact angle would be negative (meaning the pre-collision particle path must pass through the wall) and so collision with the surface impossible. The shadow factor coefficient for the probabilities associated with such cases is 0. Otherwise the local impact angle will be positive, the shadow factor probability coefficient decreases, for lower and higher angles, from a maximum at a ‘virtual wall inclination’ perpendicular to the global impact direction (in other words the impact will occur normal to the local wall facet). Since the maximum will always coincide with a positive inclination, this promotes a positive mean for the Gaussian distribution of virtual wall inclinations.

2.2 Non-Spherical Particle Modelling

Given that the topology of a sphere, introduced in section 2.1, represents the minimum in surface area to volume ratio, any less unique volume will require at least a second parameter for its mathematical description. Multiple methods for measuring the non-sphericity exist. This section builds upon the last as spherical and non-spherical particle tracking share a common methodology, indeed non-spherical particle modelling might be considered simply doctoring spherical tracking, albeit with extensive influence over all other models. In addition, non-sphericity allows manifold opportunity for variance within the particle population, both in particle shape and orientation, whereas spherical particles may differ only in diameter and density when considering aerodynamic effects. This fact suggests that greater ‘population refinement’, a greater number of streams each of lesser mass flow rate, is necessary when defining the numerical streams of non-spherical particles. In the following discussion, “orientation” takes on a particular meaning: it is the inclination of distinguishable dimensions of the particle relative to the local fluid velocity. Therefore a spherical particle may not assume differing orientation,

Table 2.1 Methods for non-spherical particle modelling.

		Shape Description	
		Monodimensional	Multidimensional
Motion	Irrotational	Fixed Orientation	Preferred Orientation
	Rotational	-	Free Orientation

since its form drag and skin friction will be unchanged (orientation is undetectable by the flow). Thus it is considered to have a fixed orientation.

Essentially there are three theoretical methods, placing varying simplifications upon the particle motion or shape description, for use in the simulation of non-spherical particles, which will play a part in all of the previous phenomena (disclosed in subsections 2.1.1-2.1.7) “fixed” (Levenspiel, 1989, and Ganser, 1993), “preferred” (Ganser, 1993, and Loth, 2008) and “free” orientation (Zhang *et al.*, 2001, Yin *et al.*, 2003, and Yin *et al.*, 2004). The former two are very closely related and use irrotational particle motion, in which the exertion of torques is ignored in determination of the particle orientation. It should be noted that the rotation about an axis of symmetry, which is non-existent in real particles but common in mathematical shape approximations, does not alter the size or position of the particle’s cross-sectional area or effective surface area and therefore may be included as this rotation has no traceable effect upon the particle orientation. However, this rotation may still be employed (for influence in the lift calculations). The latter two use a multidimensional shape description, typically bidimensional. Of course, as stated in the first sentence of this section, all non-spherical particles must have plural shape descriptors. In the case of the “fixed orientation” these are equal volume spherical diameter and a dimensionless factor for its homogenised deviation from a sphere on some basis (such as surface area), this second parameter is referred to as the ‘shape factor’, sometimes used synonymously with the ‘sphericity’ (Loth, 2008), explained in the next section 2.2.1, as opposed to multidimensional (to be described in section 2.2.2), which requires that there be at least one non-unity aspect ratio between mutually perpendicular particle dimensions. Table 2.1 helps to outline the difference between the models. No model is listed with rotational dynamics for a monodimensional (i.e. spherical) particle as under the

condition of spherical symmetry no change in orientation will be detectable by the flow, and the rotation calculations irrelevant. Following this method, constraints are placed upon the individual spherical particle models within the trajectory calculations (of section 2.2). In fact extraneous theoretical models (e.g. heat transfer) would also be distorted by the effect of non-sphericity (Pelegrina and Crapiste, 2001). Furthermore, the shape descriptors may be employed inconsistently for different models, Pelegrina and Crapiste (2001) apply a projected area shape factor for momentum exchange equations (e.g. drag) and the familiar sphericity (surface area shape factor) for both mass and heat transfer equations (e.g. particle drying) in application to potato particle drying. Despite aspect ratios as high as 3, it is apparent that the momentum shape descriptor is dimensionless (fixed orientation method). Sphericity is sufficient for use in the simple heat and mass transfer models, coarse resolution of the temperature field permits little more than a lumped exchange. Also necessary for heat and mass transfer is a characteristic length, which coherently represents the effective particle thickness and length scale in forced convection respectively, defined as arguments to particle Nusselt and Reynolds number functions. There is no allusion to these characteristic lengths' exact natures and unlike the previous shape factors they are not at unity for a sphere.

2.2.1 Measures of Non-Sphericity

Prior to the description of the modelling concepts, it is of importance to review the methodology of non-spherical particle mathematical shape description. Regular non-spherical geometric volumes can be easily described, by attributing numerical values to known dimensions (such as length, width, base, radius, semi minor axis etc.), however the context of each would have to be recorded in programming syntax for the numerical value to maintain any meaning. The goal for engineering applications is to develop a generalised model, which can handle the full spectrum of particle topology which includes a universal description (input) for that topology. An intuitive and ubiquitous foundation to the characterisation of non-spherical particles is the definition of a proportionate spherical particle. So although not touching on the degree of sphericity, just as with spherical particles, a global scaling of the non-spherical particle is preeminent for the employment of analogous dimensional analysis. This allows an

appropriate length scale for Re_p to be obtained for a multidimensional particle, namely the diameter of an equivalent sphere. The prevailing method employed is volume (V) equivalence, physically the material density is treated as constant so that this method also conserves the mass of the equivalent particle. For this reason the first approximation of non-spherical particles is universally by their equivalent volume sphere (EVS). However Clift *et al.* (1978) identify a further three modes of equivalence, these being surface area (A_s), projected area (A_p) and projected perimeter (P_p), by which the equivalent sphere might be equated. Therefore there exist the EVS, equivalent surface area sphere (ESS), equivalent projected area sphere (EPS) and equivalent circumference sphere (ECS). In fact these concepts generally form the basis for shape factor definition. In this way the ratio of one or more of these measures, for the EVS to the non-spherical particle, may be employed as “shape factors” which describe the discrepancy between the spherical and aspherical volumes. A confusing array of terms exist in the literature however these often represent multiple names for the same parameter, or its inverse. For example Loth (2008) defines the term ‘surface area ratio’ as the area of the non-spherical particle normalised by that of its EVS, pointing out that other authors have labelled its inverse as the ‘sphericity ratio’, simply ‘sphericity’ or even ‘shape factor’. This study would call the same property (inverse surface area ratio) the “surface area shape factor” but the shorter ‘sphericity’, Φ , after Wadell’s naming as: ‘degree of true sphericity’, is preferred. Care must be taken with each paper to find the individual definition of the entities therein. Ganser (1993) defines sphericity as the square root of the reciprocal of the ratio of ESS diameter to EVS diameter, which with a quick check is seen to be equivalent to the standard definition, although the benefit of this definition is not so easily perceived. The convention adopted in this thesis (Clift *et al.*, 1978) is to use shape factor to refer to the class of dimensionless geometric parameter which is a ratio of equivalent spherical to non-spherical particle measure. The measure used in the ratio precedes its name, e.g. “projected area shape factor”. Unless otherwise stated, the equivalence will be volumetric and the ratio taken with the EVS parameter as numerator to the fraction. In this way a particle’s sphericity may never exceed unity which is the value for a perfect sphere. Without spherical symmetry, the particle will present orientation dependent projections (area and its perimeter) which

complicate their implementation in shape factors, however this can be used for the preferred orientation method (in section 2.2.3) as the different orthogonal projections manifest the aspect ratio. As in the introduction to this section, in complete ignorance of the non-spherical topology, the drag coefficient is isotropic and can be found from a universal drag law with Re_p scaled by the EVS' diameter, $Re_p(d_{EVS})$, and using a shape factor to model the enhancement of the drag (often sphericity, Φ). A shape factor may also be based upon the measureable drag conditions of the particle and related to the data for spheres. Such a method will have dependence upon Re_p . The idea is presented in Clift *et al.* (1978), however a simpler form introduced by Ganser (1993) relates to constant coefficients of the drag within Stokes' and Newton's regimes. Stokes' shape factor, K_1 , is the ratio of EVS Stokes' drag ($24Re_p^{-1}$) to that of the non-spherical particle, whereas Newton's shape factor, K_2 , is the inverted volume equivalence of critical drag coefficient (i.e. non-spherical particle's to EVS'). The peculiar form of K_2 is as consequence of its subsequent use to cast an effective particle Reynolds number, Re_K , described in the next section 2.2.2. Clift *et al.* (1978) include a review of contemporary shape factors, however these find little mention in more current literature, but are re-exposed and compared in Gabitto and Tsouris (2007). A modified form of the Corey shape function (CSF) has been proposed for highly irregular particles, given by:

$$\beta = \frac{c}{\sqrt{ab}} \quad a > b > c \quad [2.1]$$

in its canonical form the CSF, β , is the ratio of the least dimension, c , to the square root of the product of its two greater dimensions, a and b , where all dimensions are mutually perpendicular (Gabbitto and Tsouris, 2007), but is mistakenly reported by Loth (2008), with a instead of c as the numerator.

This shape factor is convenient as only orthographic lengths must be measured. This may be facilitated by optical camera and automated by software. The particles are spread, with negligible contact or intrusion of individual particles, on a high contrast background and a camera takes a plan view of the particles. Under such circumstances the particles may be assumed to align their greatest cross-sectional area parallel to the surface on which they rest, therefore with this 'broadside orientation' (section 2.2.3),

relative to the camera. A similar method to estimate the particle shape by optical means, as used in this thesis, is described in section 4.3.1. Lu *et al.* (2010) use an advanced imaging algorithm to transpose three orthographic photographs into a 3D meshed volume, from which a highly tortuous surface area can be integrated. However, only the volume and surface area are taken from this.

Following Loth's (2008) convention of normalisation by equivalent sphere and area shape factor, the square of the inverse of the CSF was identified with the 'max-med-min area', A^* , this is then used to form drag corrections:

$$\beta^{-2} \equiv A^* = \frac{ab}{c^2} \quad a > b > c \quad [2.2]$$

Some naturally occurring mineral particles may form regular shapes for which V , A_s , A_p and P_p may be trivial to find (Loth, 2008). However, for a real system of irregular particles, volume estimation presents difficulties by spatial means and mass or displaced volume measurements might be precluded by the particles' sizes and diversity. This problem is not satisfactorily addressed in the literature.

2.2.2 Fixed Orientation Models for Non-Spherical Particles

The cheapest non-spherical mechanism exploits a non-dimensional identity parameter, maintaining the directional independence of a sphere, in addition to the diameter of the EVS. Therefore the same effective cross-sectional and surface area are presented regardless of particle orientation, whereby the particle's rotation is inconsequential to drag (a coincident rotatable local coordinate system tracking the particle's orientation would remain fixed, earning the model its name). This approach is rationalised for arbitrary volumes with high sphericity, or even regular isometric shape (called spherically isotropic). Notwithstanding, the same method has also been utilised in studies for drag dominated flows (e.g. terminal settling) for highly non-spherical particles of both regular and irregular shape. Effectively this method uses spherical particle physics but with an artificially enhanced drag coefficient due to its greater surface area in comparison to the EVS substitute particle or similar non-dimensional enhancement to the momentum transfer under other phenomena such as lift. Therefore the particle is non-orientatable since it has spherical symmetry (appears identical

regardless of orientation). Particle roughness (micro-surface protrusions) should not be modelled in this way, despite possible macro-sphericity of the shape, as it plays a more intricate role in the turbulence regime transition than greater surface area. Protrusions from the particle surface can hasten the onset of turbulent drag characteristics (transition from laminar wake occurs at lower Re_p), which in fact reduces the drag in the vicinity of the transitional regime (in the particle Reynolds number domain). Stepping away from perfect smoothness permits uneven roughness which could trigger localised high Re_p ‘hot spots’ resulting in ‘wake tripping’. The pressure gradients, due to the inconsistent drag regime acting on different regions of the particle surface, cause high scatter of experimental data in the transitional Re_p band (Clift *et al.*, 1970). If a turbulent wake is allowed to fully develop, irregular volumes follow spheres down a tendency to obey a Newtonian constant drag coefficient, presuming a stable settling mode is established, and is discussed in greater detail below.

Haider and Levenspiel (1989) give a good early account of the analysis of non-spherical particle settling dynamics based on the similarity of their drag curves and illustrate the base from which non-spherical particle multiphase flow modelling is performed. The sphericity (or surface area shape factor, the ratio of the surface area of an equal volume sphere, EVS, to that of the particle) is employed as the additional non-dimensional descriptor (shape factor). For the regular isometric particles, as well as discs, a clear inverse dependence of the drag coefficient upon low particle Reynolds numbers is identified, as in Stokes’ law, which is observed to diminish in transition to an independent relationship as a constant drag coefficient in Newton’s (higher Re_p) turbulent regime. The results are plotted against the standard drag curve for spheres (a 408 point set of data from a single publication) in the subcritical Reynolds domain. The isometric particles (including the sphere) have practically coincident Stokes’ regime drag dependence, whereas the disc drag decreases at a similar gradient but from a raised intercept, that is itself increased by lesser particle sphericity. It might be noted that the least spherical isometric shape used (for indeed the regular tetrahedron is the least spherical regular shape) in this study had a shape factor, whose deviance from unity (0.607) is greater than the absolute value of the most spherical disc’s shape factor (0.230). So it is questionable, although academic, as to whether the previously

mentioned intercept is bred of aspect ratio or simply that the isometric particles' high sphericities prevent its detection herein. In addition to their similar structure, a trend for advancement of the transition to Newton's regime, at depressed Re_p , for increasing non-sphericity is recognised, whereby greater Newtonian drag coefficients are assumed by less spherical particles. This is due in part to the quiescent fluid intercept value and significantly to the earlier curtailment of the Stokesian regime. Values of coefficients in the four parameter spherical drag correlation of a very similar form to that supposed by the Clift-Gauvin drag curve are evaluated by regression. Due to the difference in the power of the second Re_p term (assumed linear by Haider and Levenspiel, 1989) between the forms the previous four parameters do not correspond for the two approaches. Also the coefficients' own dependence upon shape factor, to suitable polynomial order, is calculated. The resulting equation for non-spherical particle drag coefficient is rather unwieldy (containing 13 arbitrary constants discounting the value in Stokes' law) leading the authors to propose a truncated version.

Criticism of Haider and Levenspiel's (1989) more accurate approach lies on the difficulty associated with measuring the surface area of real (irregular) particles, examined in section 2.2.1, and the cumbersome dual argument function required for non-spherical particles. Chhabra *et al.* (1999) also doubt that experimental accuracy allows valid determination of the empirical constants to the four decimal places used. These reservations might also be held against Haider and Levenspiel's (1989) simplified model. To this end Ganser (1993) attempts to consolidate to a single independent variable (effective particle Reynolds number, $Re_K \equiv K_1 K_2 Re_p$) using practically measureable shape descriptors. The author named these Stokes' and Newton's shape factors, K_1 and K_2 respectively, although the original proponents of the latter named it 'scruple' and is simply the ratio of a non-spherical particle's Newtonian drag coefficient to its EVS' (generally above unity). For full definition, the "constant" drag coefficients for the real and fictitious spherical particles are evaluated at $Re_p = 10^4$, alternatively it is averaged over a range of effective particle Reynolds numbers such that $10^4 \leq Re_K < 10^5$ (N.B. effective Reynolds number range, Ganser, 1993). Instead, K_1 , in creeping flow ($Re_p \leq 0.05$) is inversely defined as the ratio of an EVS' Stokesian drag relation ($24Re_p^{-1}$) to the non-spherical particle's (therefore generally less than

unity). The dependence of Stokes' shape factor upon the size of the pipe for the experiments was investigated, which for fair comparison, led to the adoption of an infinite pipe correction, K_{10} . The premise is that a drag law based on a single argument, the effective particle Reynolds number, Re_K , for a sphere can be used to accurately predict the behaviour of the full spectrum of particle shapes from Stokesian to Newtonian flow. The assumptions being that, for all particles, a regime in which the drag is proportional to the velocity and a regime in which the same is proportional to the square of the velocity exist and the transition occurs in the same manner. The effects of non-sphericity will be commuted by the enhancing of Re_K compared to the neat EVS flow, $Re_p(d_{EVS})$. This study does not attempt to model into supercritical drag, which is not well understood for non-spherical particles (Loth, 2008), in fact, it is suggested that no drag crisis exists for highly irregular particles, presumably the roughened edges induce greater propensity for the advanced wake separation characteristic of Newton's ballistic regime. The drag curve chosen is as suggested by Haider and Levenspiel (1989), influenced by the Clift-Gauvin drag curve.

Accepting warranted rounding (4sf) the constants presented by Ganser (1993) and Haider and Levenspiel (1989) are identical for the spherical case. This is to be anticipated as all evidence suggests that an identical set of drag data, and certainly the same function template were used in both studies. This common drag function accepts different arguments depending on the study, recall that Haider and Levenspiel's (1989) is purely a function of Re_p when sphericity can be taken intrinsic to the constants, whereas Ganser's (1993) uses $Re_K (K_1 K_2 Re_p)$ as a single compound argument. The particle Reynolds number in both cases is based upon the same characteristic EVS diameter. In a review by Chhabra *et al.* (1999), five separate fixed orientation drag laws for non-spherical particles of arbitrary orientation were compared. The conclusion is that the method of Ganser (1993) provides the best fit for a wide compilation of available experimental results from some nineteen publications. However, a disadvantage is reliance upon sphericity as calculating the surface area of irregular particles is a non-trivial undertaking (Chhabra *et al.*, 1999), as reported in section 2.2.1. Recognition should be given to the fact that the relationships of the shape factors to the sphericity need not be used as the Stokesian and Newtonian shape factors can be

evaluated directly. Providing the K_1 and K_2 values for appropriate particle shapes exist, this criticism can be circumvented.

Another in depth examination, following similar supposition to that of Ganser (1993), evaluates different classes of non-spherical shape (ellipsoidal, regular and irregular) in Stokes' regime as well as general non-spherical particles in Newton's in order to generate a drag curve fit for subcritical flow (Loth, 2008). An insightful method to compare the drag data was to plot the normalised drag coefficient, $C_D^* \equiv C_D K_2^{-1}$, once again as a function of the effective particle Reynolds number, Re_K . In this way, the C_D^* for all shapes would revert to the critical drag coefficient for a sphere within Newton's regime. Observation of two distinct drag responses with segregation between circular and non-circular cross-section is reported. This is ambiguous terminology as it conjures the image of circular projected area (normal to the flow), however from the context it is apparent that the cross-section to which reference is given is in a plane parallel to the flow. For this reason alternative terms are introduced here as "convex prow" and "planar prow". Prow relates to the projected 3D surface presented by the particle, rather than the simple projected area. To illustrate, a sphere has circular projected area but hemispherical (convex) prow, whereas a disc, presenting its full area, has both a circular projected area and flat circular (planar) prow (which enhances the ambiguity in the previous terms) and a cube orientated so that a line connecting the centre and any vertex lies parallel to the relative flow would present an hexagonal projected area but three mutually perpendicular square planes as its (planar) prow. For a spheroid/cylinder assuming 'broadside orientation' (Loth, 2008), as discussed in section 2.2.3, this will be the bowed projection from a plane collinear to the axis of symmetry and of resemblance to the underside of a canoe. Such 'circular cross-section' shapes are better regarded as "convex prow" shapes as they have a curved face. Two-dimensional shapes, such as discs and chips, will be monoplanar whereas isometric shapes and irregular particles will likely appear multifaceted (or multiplanar) from the perspective of the flow, hence these three groups are collectively the "planar prow" particles.

An insert within the graph (Loth, 2008, Fig.8, p350) shows that such a segregated relationship would be incomprehensible from the raw data (C_D against Re_p). The phenomenon is not produced artificially as a consequence of a diametric schism in the

sphericity values of the representative particles, despite similar data to that of Haider and Levenspiel (1989). Recognising the gulf that remains between the sphericity values of the isometric and anisometric particles, it might be expected that when only these sphericity extrema are considered, in the archetypal particle classes, a more general transition across the full sphericity spectrum would be intractable from the responses of these two polar groups, however in this case the members within a segregation do not share similar sphericity. Indeed no relation to sphericity is detectable, perhaps unexpectedly the spherical and acicular (high aspect ratio cylindrical or spheroidal) shapes demonstrate a closely correlated trend of less rapid transition to the critical drag coefficient (convex prow). Whereas even highly spherical, but angular, isometric particles (such as the cube octahedron, $\Phi = 0.9$) show a sharper decline in C_D^* with Re_K to an earlier Newtonian regime (planar prow). The discs follow the “planar prow’s” trend. An increased degree of scatter is present in this rectilinear cross-sectional group particularly at commencement of the critical drag. It is difficult to determine whether this is a physical curiosity or simply a raised concentration of datum points is present at this Re_K location.

Employment of this directionally independent model preserves the (equivalent volume) spherical particle model’s disregard for rotation, simplifying the calculation, but also for hydrodynamic drift. This is translational motion, induced perpendicular to the drag direction, caused by the direction of the body force exerted due to the effective pressure gradient. The considered pressure gradient is that of particle drag, whereby a uniform velocity profile exists perpendicular to the drag direction, but viscous resistance to the passing of the particle causes a greater pressure on the windward side of the particle (velocity is relative to the particle’s). Additionally, the resultant of the surface integral of the drag force upon an anisometric shape is deflected from the true direction of drag (to contain a component of drift). Essentially a longer edged area “catches” more relative velocity “wind” than a shorter edge since the total of the forces normal to the elemental areas and acting perpendicular to the drag force do not balance (Clift *et al.*, 1978). In modelling terms the drag force may be decomposed into directions corresponding to orthogonal “prows” of known projected area. The deflected drag force acts at the centre of pressure. This is the point at which the resultant

hydrodynamic (surface) force acts, as consequence of a pressure gradient within the fluid across the solid particle, without inducing a moment. In general, the particle centre of pressure does not project through the particle centre of mass (centroid), observed along the relative velocity. However, no drift would be induced should the drag direction be parallel to two orthogonal planes of symmetry which exist in the particle volume (the centroid necessarily lies on the line of these planes' intersection). Two such planes indubitably exist where a volume of revolution (such as a spheroid) is aligned with its axis of symmetry parallel to the drag. Following this discussion, it is apparent that drift cannot be caused by any drag acting upon a constant density spherical particle. Spherical symmetry imposes infinite axes of symmetry, at the centre of volume, parallel to all directions. In addition to the drift an aligning torque is developed, when dealing with anisometric shapes (except under the previously mentioned symmetry conditions), since the pressure gradient acting at the centre of pressure does not project through the centroid of the particle. So a moment is induced about the centroid by a component of the pressure force acting about an arm (which is the displacement, perpendicular to the relative velocity, between the particle's instantaneous centre of pressure and centre of mass). Whichever shape factor is used, it is essentially, merely a drag correction to a spherical model and represents significant physical truncation for orientatable particles. A particular weakness of this method, as warned by Loth (2008), is that highly dissimilar shapes might exhibit the same sphericity with vastly different drag response. This eventuality is likely both between isometric and acicular particles and even prolate and oblate particles of the same anisometric topology.

2.2.3 Preferred Orientation Models for Non-Spherical Particles

Anisometric particles have a tendency to present their greatest projected area to the relative flow of fluid past them, Clift *et al.* (1978) call this the 'broadside orientation'. At first this may seem counterintuitive, when considering projectiles the opposite, that the smallest area is perpendicular to the flow appears true. However, these are stabilised by parallel axis rotation, which resists pitching of the rotating axis due to precession, or fletching, which increases the drag at the hind end of the projectile, so shifting the centre of pressure behind the centroid and causing the shaft to realign to the

flow. As described in the previous section (2.2.2) when the particle is unaligned to the flow there exists an unbalanced distribution in the hydrodynamic forces between the leading and trailing edges of the particle. The preferred orientation is as a consequence of the lateral displacement of the centre of pressure, of the aerodynamic forces acting on the particle, from the particle centroid, thereby inducing a torque on the particle. An analogy would be the self-aligning torque experienced by tyres in motion due to the local deformation of the contact patch.

A form of the hydrodynamic drift may be incorporated by way of the ‘preferred orientation’ assumption. This is an adaption of mono-directional shape factor to multi-dimensions. Generally it will be based on cylindrical projected areas (two parameters: being the length and diameter, otherwise the aspect ratio of these axes including information about oblate or prolate shape and d_{EVS} must be known), physically, rotation for orientation may exist. However that normal to the preferred direction is ignored, as with fixed orientation, and the other moments of inertia are null resulting in instantaneous orientational compliance with the fluid flow direction (averaged value). Therefore torque due to the drift is also ignored. It is ostensible in the preceding sentences that the preferred orientation method exploits fixed orientation. However, the rationale is that the preferred orientation is that which is stationary relative to the fluid flow, whereas fixed orientation exhibits such a behaviour both locally and globally as rotation cannot be discerned. The lucid progression from spherical “donor” physics as has so far been described, for particles of significant aspect ratio, is to adopt a non-spherical, but still idealised mathematical, volumetric shape, so that geometric parameters such as surface area are still analytically apparent. In this way the characteristic diameter, i.e. d_{EVS} , will have an analytical solution.

This model is a generalisation of the ‘fixed orientation’ model so that dimensional heterogeneity of a particle may be included, providing a mathematical revision, reflecting the real form drag and skin friction for appreciably orientatable particles, to yield two separate drag coefficients at orthogonal orientations. Generally, this takes the form of a spheroidal shape with a single aspect ratio, however this method is readily adoptable for any such isosceles (or scalene) regular shape (i.e. anisometric – isometry would relapse into the fixed orientation method). The concept was touched on in the

previous section 2.2.2 in the rationalisation of the “prow” grouping (Loth, 2008). Although a monodimensional model was used the empirical data in the study is implicitly influenced by the particle’s (Re_p dependent) orientation. No greater simulation mechanism is required, than for fixed orientation, and the result should be much the same if based on empirical data. However for particles with a stable (and correctly presumed) settling orientation this method should lend better accuracy to extrapolated drag coefficients. The general assumption of ‘broadside preferred orientation’ (greatest projected area facing the relative velocity) would suggest higher terminal drag coefficient for increasing non-sphericity, however the preference of orientation is formulated in simple terminal settling velocity (laminar region) experiments and not corrected for higher Re_p .

It has been estimated that the ratio of Stokes’ drag coefficient of a non-spherical particle to its EVS’ (K_1^{-1} from the previous section, 2.2.2) would have dependence upon the non-spherical particle surface area and projected area, in the same proportions as the drag on a spherical particle, reported in Ganser (1993). This is slightly abstracted from Clift *et al.* (1978) which states, in reference to slow viscous flow past a solid sphere, “*Two thirds of this drag arises from skin friction, one third from form drag, and the component due to deviatoric normal stress is zero.*” The deviatoric normal stress to which is alluded is critical for fluid particles, which are inviscid relative to the carrier (i.e. bubbles in liquid) as these may be easily deformed by the flow, however pneumatic or hydraulic systems of solid particles have an infinite viscosity ratio and so the deformation of the particles due to the fluid viscosity is effectively zero. The proportions of drag from the separate sources, published by Clift *et al.* (1978), recreates exactly the ratio of the surface area of a hemisphere ($2\pi r^2$) to a circle (πr^2), which are, respectively, the presented surface area to the flow (or “prow”), and the projected area of a sphere.

Due to the linearity of the drag to the relative velocity, at low Re_p , under conditions of Stokes’ law, the drag force on a particle of oblique orientation may be determined as the resultant of decomposed particle directions (i.e. parallel and normal to the axis of symmetry for a spheroidal particle) in which the components of relative velocity act (Loth, 2008).

2.2.4 Free Orientation Models for Non-Spherical Particles

True free-orientation models are not explored in this thesis as the full calculation of the quaternion equations, detailed in Hughes (2004), of three-dimensional rotations are expected to be preclusive for a representative population of simulated particles. The method of Yin *et al.* (2003) presents a successful, if computationally laborious, method for cut straw pneumatic transport. However these particles are described as having dimensions of the order of 10 times greater than other pulverised biomass studies. Pertinent to rotation is the relationship of a solid volume's moment of inertia to L^5 . Therefore the response to a torque of a PF particle could be expected to be 10^5 times as great and require much smaller timesteps in the angular momentum ODE calculations.

2.3 Pulverised Fuel Combustion

Pulverised fuel power stations are the predominant method of energy generation from coal. They burn faster than grate boilers and therefore have higher power density but have a less energy intensive operation than do fluidised beds (Williams *et al.*, 2001, and Gera *et al.*, 2002). Pulverised coal combustion modelling has seen great interest in the literature for some time (Badzioch and Hawksley, 1970, Eaton *et al.*, 1999, Williams *et al.*, 2002, Backreedy *et al.*, 2005, and Jones *et al.*, 2010). The most common solution to the simulation and modelling of the complicated interactive processes of pulverised coal combustion is firstly, as with particle flow, to simulate a single characteristic particle in place of a packet of particles. The total heat and species exchanges between the Lagrangian packet of particles and Eulerian fluid are calculated from the models introduced below multiplied by the number of particles in the packet (ANSYS, 2009c). Particular issues of interest to operators with regard to any solid fuel combustion modelling are the rate and extent of combustion (particle extinction) as well as gaseous pollutants, notably NO_x , and corrosive condensates that may lead to slagging and fouling.

2.3.1 Coal Combustion Modelling

Williams *et al.* (2002) outlines the coal particle combustion model methodology, in sequential stages, as “*heating up, devolatilisation, volatile combustion and the combustion of the char*”. These describe distinct episodes during the combustion. Other studies use identical methodology for coal combustion modelling (Backreedy *et al.*, 2006, Ma *et al.*, 2009, and Edge *et al.*, 2011). The standard solid fuel combustion models in ANSYS Fluent v13.0 are based on these foundations. The slightly altered sequence is as follows: inert heating, evaporation, inert heating, devolatilisation, volatile combustion, char combustion and inert heating. These in fact describe the full response of combusting particles throughout their trajectory rather than only during combustion. No flame would be present until the volatile combustion stage. Two inert heating stages exist, although this is really the default behaviour under conditions of no mass exchange. Coal dust in power generation applications will generally enter the computational domain at a temperature when evaporation would have begun and a secondary heating stage would only be apparent between the temperature plateaux of evaporation and devolatilisation for wet coals. During evaporation or devolatilisation, the rate of moisture or volatile mass loss from a particle is dependent upon temperature and the remaining pertinent component fraction, commonly called the Arrhenius equation. Many experimentally measured activation energies and pre-exponential values are available in the literature (Smith *et al.*, 1994, Gera *et al.*, 2001, Williams, 2002, Ma *et al.*, 2009, and Jones *et al.*, 2011) and the local Eulerian cell receives species and mass sources to balance the system. Actual combustion of the volatile gas may be handled by a fluid equilibrium combustion model. As volatile release occurs early in the particle’s furnace residence and initiates heat output from the fuel, accurate devolatilisation modelling is imperative or the error will be further compounded in other stages of combustion (Williams *et al.*, 2002, and Abbas *et al.*, 2003).

The final stage in coal combustion is the char combustion. This is generally assumed to be pure solid carbon which oxidises to leave incombustible ash (Williams *et al.*, 2002, and ANSYS, 2009c). Char combustion is governed by temperature and oxygen concentration, but also by the mass transfer, pore growth, particle size, its composition and fragmentation. In practice char combustion is assumed to be controlled

by: (a) chemical reaction rate, (b) chemical reaction rate and pore diffusivity, or (c) mass transfer. Case (a) closely resembles simple chemistry models for small particles at low temperature. In case (b) the oxygen at the particle surface cannot be replaced fast enough for the chemical rate to be maintained at high temperatures. In case (c), at very high temperatures the activation energy becomes negligible and so oxygen transfer controls the combustion. Eaton *et al.* (1999) favour this oxygen diffusion limited reaction rate. Early char combustion takes place before full devolatilisation and therefore the hydrogen content may affect the combustion. Lower temperature char combustion tests' intrinsic reactivity results predict an under-activation energy requirement due to catalytic content. Pore surface area is difficult to model throughout char lifetime (Williams *et al.*, 2001). Williams *et al.* (2002) investigated the Baum and Street (1971) kinetic/diffusion surface reaction rate for char combustion, as well as Smith's (1982) intrinsic reactivity. In the latter chemical reactivity suffers a reduction based on pore diffusion. An average structure and surface area are assumed throughout the combustion modelling for simplicity. However physically and chemically, the size, porosity and surface area changes and hence so does the reactivity. The data for comparison were obtained by a drop tube furnace (DTF) and heated wire mesh pyrolysis in an N₂ atmosphere to simulate devolatilisation then the resultant chars combusted in an oxidising O₂-N₂ environment. The Brunauer, Emmett and Teller (BET) surface area reactivity is conducted in N₂ at its boiling point, 77K. These conditions reduce the reactivity of micropores, but these also play a lesser role at rapid high temperature combustion (transport controlled), however it is the best method for macropore char reactivity prediction. Initial char surface area is related to the fixed carbon content of the parent coal. Baum and Street's (1971) char combustion requires a library of coefficients for each coal, determined experimentally. The intrinsic reactivity method of Smith (1982) is not dependent upon the pore surface area and size allowing a common comparison of different chars. When testing the methods in the computational fluid dynamics (CFD) software, for a DTF, Baum and Street (1971) over predicted the total burnout, whereas the intrinsic methods was at worst inaccurate by 20% from the experimental results (Williams *et al.*, 2002).

In recent years, the fraction of unburnt carbon (UBC) in ash has increased due to the use of low NO_x burners. This reduces the thermal efficiency and also might cause the ash to be unusable by the construction industry. Clearly the ash would be far more expensive to dispose of otherwise. The principal problem is that some particles do not react fast enough allowing the char combustion to deactivate due to annealing etc. Also rich 'pockets' can isolate the coal particles from air (Williams *et al.*, 2001).

2.3.2 Biomass and Co-Combustion Modelling

Biomass has been shown to respond in a similar way to coal (Gera *et al.*, 2002, and Ma *et al.*, 2007), however in general a far greater mass fraction of biomass is moisture and volatiles compared to coal, also volatile release begins at a lower temperature. Ma *et al.* (2009) presents the dry, ash-free (DAF) volatile fraction of three typical international bituminous coals and four varieties of biomass provoking interest (representing both energy crops and agricultural residues), in the range of 35-45% and 75-90%, respectively. These were measured by a low temperature DTF and 50-60% volatile matter (VM) is expected of bituminous coals at furnace temperatures. Fibrous biomass does not mill easily resulting in larger particle sizes (Yang *et al.*, 2008, and Ma *et al.*, 2009). Although difficult to resolve in practice Williams *et al.* (2001) state that due to the interaction of volatiles from differing coals and combustion temperatures in a blend, their individual contributions cannot simply be weight averaged. This would also apply to biomass or biogas/natgas blends and co-firing.

Increased UBC in ash has been linked to biomass co-firing when compared to previous coal combustion. Larger chars that undergo lesser shrinking than those of coal due to the lignitic cellular structure of herbaceous and arboreal biomass promote UBC by delaying ignition, decreasing suspension and persisting with an enlarged surface area – increasing heat loss. Moghtaderi (2007) concludes that, as biomass is specifically less reactive than coal (purely considering the calorific value of the fuels), less internal heat generation takes place, requiring a greater critical particle size (or a higher temperature to accommodate smaller particles) to ensure radiative heat loss does not extinguish the particle. Biomass and coal particle burnout is similar above the critical sizes but deviate approaching biomass' critical diameter and proposes adding highly reactive fuel to

improve burnout. Therefore larger particles would be expected to improve burnout. Alternatively it may be thought that each particle extinguishes once obtaining a certain small, temperature dependent, diameter, so increasing the particle sizes and thereby reducing the number of particles would aid burnout. However, due to the very high proportion of volatiles in biomass fuels, the study's methodology of combusted chars that were produced in a non-oxidising environment is questionable. One might speculate that the low char reactivity would be counteracted by increased temperatures due to the volatile combustion. In addition, aerodynamically, larger particles will have stronger inertial and gravimetric responses, reducing their residence times at the highest furnace temperatures.

Once again the non-sphericity will influence the mathematical treatment of acicular biomass particles. Lu *et al.* (2010) investigated the influence of particle surface area during devolatilisation of a single particle of biomass, grouping the particles as approximate spheres, cylinders and flakes. This yielded good correlations between the predictions and experimental data and a large disparity was observed between the rates of devolatilisation of spherical and aspherical particles. However, the behaviours of cylinders and flakes were very similar. Also larger particles may warrant more advanced heat transfer modelling. Gera *et al.* (2002) and Gubba *et al.* (2011) attempted to address these issues in different manners, respectively considering; flame propagation along a cylindrical particle's length, and radial heat transfer within a cylindrical particle.

2.3.3 Pollutant Modelling

Emissions of NO_x from energy generation are stringently legislated. In the EU the NO_x emission limit for large scale coal power stations is 200mgNm^{-3} . For co-firing stations, if a particular fuel class accounts for greater than 50% of the thermal input during operation that fuel class' legislative limit is used. The NO_x emission limits are identical for biomass and coal in a plant with a power rating in excess of 300MW_{th} (EC, 2011). Approximately 80% of NO_x in coal power stations is from char-N considered by the chemistry (Williams *et al.*, 2001). However, the small concentrations of NO_x , relative to other species, play a negligible role within combustion and so the NO_x formation may be predicted by post-processing using the models described in

Backreedy *et al.* (2006). In this method, source terms for nitrogen oxide radicals are included in proportion to devolatilisation and char combustion mass loss as described in section 2.3.1. The key sources of NO_x for solid fuel combustion at high temperatures are, in order, fuel-N and thermal-N (Williams *et al.*, 2001). Fuel-N comes from the intrinsic nitrogen content of the fuel whereas thermal-N is produced from high temperature oxidation of atmospheric N₂ in the oxidising environment. It has been found that the biomass chars retain a greater proportion of the original fuel-N than those of coal (Wornat *et al.*, 1995), although Glarborg *et al.* (2003) suggest that this trend is reversed at furnace temperatures. Co-firing with biomass is expected to reduce NO_x emissions, compared to burning coal, through lower fuel-N, on a calorific basis, and decreased combustion temperatures.

Chapter 3

Numerical Modelling

This chapter gives a brief introduction to the subject of computational fluid dynamics (CFD) and in particular the application of the ANSYS Fluent commercial code, relating to particle aerodynamics and combustion simulation. Thereafter is given an overview of the mathematical models particular to particle flow and combustion. Within CFD there are several distinct disciplines, such as meshing techniques, the mathematical theory and numerical integration schemes. Within each of these are manifold methods which cannot be adequately approached herein. A brief summary of the background elements to this thesis is given prior to a more detailed description of the particle modelling.

3.1 Computational Fluid Dynamics

CFD, simply, is the numerical solution of fluid dynamics problems. It was developed because many problems in fluid dynamics have no closed-form analytical solution. The cornerstone of fluid dynamics is the Navier-Stokes equations. The equations of motion, combined in the momentum vectoral equation, were independently derived by Sir George Stokes and Louis Navier. It is now common for the Navier-Stokes equations to be used as a label for all the governing equations of fluid flow; continuity, momentum and energy (Massey, 1998). CFD is essentially the discretisation of these partial differential equations (PDEs) for solution by numerical integration schemes. The technique uses finite-difference, in that finite spatial cells are used to replace infinitesimal elements as classically understood in calculus. The basic finite-difference method (FDM) has equally spaced nodes, representing identical volumes (in 3D), known as control volumes (CVs). This simplifies the flux as all areas, over which it takes place, are equal and the directions of the flux are globally aligned. The partial derivatives are approximated by difference quotients and so the values in the flow field can be developed iteratively, given the boundary conditions (BCs). The finite element

method (FEM) is an alternative finite-difference form originally developed for structural analysis (Versteeg and Malalasekera, 1995). It is particularly powerful as it allows the use of unstructured meshes of triangularly/quadrilaterally faced elements, the irregularity of which is recorded as a shape function (Donea and Huerta, 2003). This method uses the polynomial integral forms of the partial differential equations for numerical integration rather than difference quotients (Massey, 1998). The reader is directed to Roache (1998), Donea and Huerta (2003), and Zienkiewicz *et al.* (2005) for a more thorough introduction to FEM.

ANSYS Fluent uses the finite volume method (FVM). Massey (1998) states, “*Advocates of FVM claim that it combines the best feature of the FEM, namely its ability to handle complex geometries readily, with the virtue of the FDM, the simple and self-evident relationships between the finite-difference formulations and the partial differentials they replace.*” Conservation is ensured by integrating over the CVs, difference quotients replace partial differentials, as with finite-difference, and unstructured meshes may be used, as with finite elements (Versteeg and Malalasekera, 1995).

3.1.1 The Simulation Process

In general, the initial stage to performing CFD calculations is to set up a case, then run the calculation until convergence and finally interpret the results. All steps require operator decisions. Roache (1998) identifies CFD more as numerical experimentation than theory. Setting up a case requires generation of the mesh, also known as the grid, and prescribing the mathematical representation of the physics and chemistry. Similar to a thermodynamic system considered on paper, the mesh is the numerical domain that sufficiently describes the physical volume of the fluid system in the simulation. Several simplifications to the numerical domain over the physical volume may, and often must, take place. Small geometries might be omitted, as they require fine meshing, however there must be experience from experiments to justify the truncation of the physical problem. Also many engineering systems will be open, inducting and exhausting through at least one inlet and one outlet, the extent of these fluid boundaries is set by the arbitrary termination of the system. The incomplete measurements of the extremities of

experimental open systems and a total deficiency of data from such regions often require that the boundaries of the numerical system be cut close to the more accurately defined experimental volume with assumptions of the properties of the inlet and outlet streams used. The mesh is split into CV cells, the number of which (typically perhaps 10^3 - 10^7) is the ‘mesh size’. The cells may be refined down in edge length/volume (increasing mesh size) at critical regions of the domain. In fact it is probably more accurate to state that operators follow the equivalent practice of coarsening the cells in less vital regions of the mesh. All flows considered in this thesis are of subsonic air and are assumed to be incompressible and ideal.

This numerical domain records the field variables at spatial locations. The edges to the domain have prescribed BCs. A BC is generally a constant value for a field variable at a particular point, this is still true when a spatial distribution for BC values is given on a face by a non-periodic function of face coordinates, but may also be a function of time (periodic), state zero gradient in the field variable (symmetric) or be an indirect function involving a constant or periodic ambient condition rather than the field variable itself. The CVs must have initial values assigned to them. Highly inaccurate ‘first guesses’ may be employed so long as they are not unphysical. Quiescent fluid at a reference density, pressure and temperature is commonly the first guess.

3.1.2 Conservation Equations

The Navier-Stokes equations are repeated from the Fluent Theory Guide (ANSYS, 2009a) in vector notation as equations [3.4]-[3.5], [3.7]. The conservation forms in Leibniz notation provided by Massey (1998) may be useful for familiarisation. Initially a reminder of some 3D vector calculus notation is given (ANSYS, 2009a):

$$\text{Gradient,} \quad \text{grad}(f) = \nabla f = \left[\frac{\partial f}{\partial x} \quad \frac{\partial f}{\partial y} \quad \frac{\partial f}{\partial z} \right]^T \quad [3.1]$$

$$\text{Divergence,} \quad \text{div}(\vec{F}) = \nabla \cdot \vec{F} = \frac{\partial F_x}{\partial x} + \frac{\partial F_y}{\partial y} + \frac{\partial F_z}{\partial z} \quad [3.2]$$

$$\text{Curl,} \quad \text{curl}(\vec{F}) = \nabla \times \vec{F} = \left[\frac{\partial F_z}{\partial y} - \frac{\partial F_y}{\partial z} \quad \frac{\partial F_x}{\partial z} - \frac{\partial F_z}{\partial x} \quad \frac{\partial F_y}{\partial x} - \frac{\partial F_x}{\partial y} \right]^T \quad [3.3]$$

Mass conservation equation

$$\frac{\partial \rho}{\partial t} + \nabla \cdot (\rho \vec{u}) = S_m \quad [3.4]$$

states the rate of change in mass concentration, plus mass convection out of the cell, is equal to the volumetric mass source. Fluid density, ρ [kgm^{-3}], time, t [s], fluid velocity, \vec{u} [ms^{-1}], mass source term, S_m [$\text{kgm}^{-3}\text{s}^{-1}$]. The mass source term is used to record the increase in fluid mass in a CV due to the mass from a source outside of the continuum translating into the fluid phase. An example might be gaseous release from a solid particle, in which mass tracked in the Lagrangian frame has translated into the Eulerian cell. The mass conservation equation is also commonly referred to as the continuity equation since it enforces the condition of a fluid continuum.

Momentum conservation equation

$$\frac{\partial}{\partial t}(\rho \vec{u}) + \nabla \cdot (\rho \vec{u} \vec{u}) = -\nabla p + \nabla \cdot (\bar{\tau}) + \rho \vec{g} + \vec{F} \quad [3.5]$$

the rate of change of momentum concentration, plus momentum convection out of the cell, is equal to the opposite of the momentum concentration due to the pressure gradient, plus momentum concentration due to stress divergence, plus momentum concentration to due gravity, plus momentum concentration due to body forces. Pressure, p [Pa], stress tensor, $\bar{\tau}$ [Pa] (see equation [3.5]), gravimetric acceleration, \vec{g} [ms^{-2}], body forces, \vec{F} [Nm^{-3}]. The body force term represents the sum of all body forces, examples would be the drag force from interaction with immersed particles or the resultant magnetic force.

$$\bar{\tau} = \mu \left[(\nabla \vec{u} + \nabla \vec{u}^T) - \frac{2}{3} \nabla \cdot \vec{u} \mathbf{I} \right] \quad [3.6]$$

where μ [$\text{kgm}^{-1}\text{s}^{-1}$] is the molecular viscosity. The stress tensor is 3D and 2nd order (3×3). \mathbf{I} is the identity matrix, so the last term of equation [3.6] is only present in the three principal directions.

Energy conservation equation

For isothermal flows the energy conservation need not be calculated,

$$\frac{\partial}{\partial t}(\rho E) + \nabla \cdot (\vec{u}(\rho E + p)) = \nabla \cdot \left(k_{\text{eff}} \nabla T - \sum_j H_j \vec{J}_j + (\bar{\tau}_{\text{eff}} \cdot \vec{u}) \right) + S_h \quad [3.7]$$

where the terms represent: specific total sensible enthalpy, T [J], effective conductivity, k_{eff} [$\text{Wm}^{-1}\text{K}^{-1}$], fluid temperature, T [K], enthalpy of species j , H_j [J], specific diffusive flux of species j , \vec{J}_j [$\text{m}^{-2}\text{s}^{-1}$] (equation [3.11]), effective stress tensor, $\bar{\tau}_{\text{eff}}$ [Pa], volumetric power source term, S_h [Wm^{-3}]. The multi-species concept is introduced in the next section 3.1.3. The total specific enthalpy is defined below:

$$E = h - \frac{p}{\rho} + \frac{|\vec{u}|^2}{2} \quad [3.8]$$

where h is the specific enthalpy [Jkg^{-1}].

For incompressible flows, work done by the pressure, kinetic energy and viscous heating are negligible, and so the energy equation takes the following form:

$$\frac{\partial}{\partial t}(\rho E) + \nabla \cdot (\rho \vec{u} e) = \nabla \cdot \left(k_{\text{eff}} \nabla T - \sum_j H_j \vec{J}_j \right) + S_h \quad [3.9]$$

where e is the specific internal energy [Jkg^{-1}]. The rate of change in enthalpy concentration, plus the specific sensible energy convection out of the cell, is equal to the energy concentration due to conduction, minus the energy concentration due to diffusion, plus the volumetric power source term. This source term includes the heat of reaction and heat of radiation.

The equations may be discretised in different forms and solved sequentially or coupled. The segregated pressure-based method within Fluent (ANSYS, 2009a) has been used for calculations presented in this thesis. The segregated pressure-based method solves the directional components of the momentum equation sequentially and formulates a pressure correction which automatically satisfies continuity, thereafter the other scalar transport equations, such as energy and turbulent properties are iterated sequentially. Sequential (segregated) rather than coupled solution of the transport equations slows convergence (increases the number of iterations) as the equations are

inter-dependent, but reduces the primary memory requirements and this benefit has been exploited since the full scale furnace simulations use millions of cells.

3.1.3 Gaseous Reactions

There are several methods available to model gaseous reactions in finite volume simulations (ANSYS, 2009a). For large scale combustion of complex volatile species a reasonable, moderately computationally expensive method is that of eddy-dissipation with pseudo-species transport. The transport of the most significant species, such as N₂, O₂, CO, CO₂ and fuel-volatiles, is simulated using a convection-diffusion equation for their mass fraction in the following form:

$$\frac{\partial}{\partial t}(\rho Y_j) + \nabla \cdot (\rho \bar{u} y_j) = -\nabla \cdot \bar{J}_j + R_j + S_j \quad [3.10]$$

this states that the rate of change of mass of species j , plus the convection of the mass of species j out of the cell, is equal to the diffusion flux of mass of species j into the cell, plus the volumetric source of mass of species j from the reactions, plus the volumetric source of mass of species j from the discrete phase. Mass fraction of species j , Y_j , specific mass fraction of species j , y_j [kg⁻¹], reaction source term for species j , R_j [kgm⁻³s⁻¹], discrete source term for species j , S_j [kgm⁻³s⁻¹]. The reaction source term introduces new mass of a species when that species is a product of the chemical reactions, the discrete reaction source term introduces the mass when the species is released from outside the fluid continuum, such as from devolatilisation.

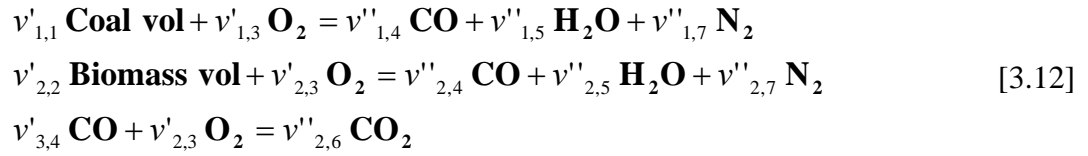
The diffusive flux of species j , \bar{J}_j , in a turbulent flow is determined as follows:

$$\bar{J}_j = -\rho(D_{m,j} + D_t)\nabla y_j - D_{T,j}\frac{\nabla T}{T} \quad [3.11]$$

the equation simply states the coefficients of the flux against the species gradient and normalised temperature gradient. Mass diffusivity of species j , $D_{m,j}$ [m²s⁻¹], turbulent diffusivity, D_t [m²s⁻¹], volumetric thermal diffusivity of species j , $D_{T,j}$ [m⁻¹s⁻¹].

A set of volumetric reactions describe the stoichiometric conditions, the lower calorific value (of converting the pseudo-species volatiles into higher state products) must also be calculated for the heat of reactions.

For sulphurless coal and biomass combustion there would be three equations in the form:



where $v'_{r,j}$ [mol] represents the stoichiometric coefficient of reactant species j in reaction r , and $v''_{r,j}$ [mol] represents the stoichiometric coefficient of product species j in reaction r . In equation [3.12] the species must be numbered; 1, coal volatile, 2, biomass volatile, 3, \mathbf{O}_2 , 4, \mathbf{CO} , 5, $\mathbf{H}_2\mathbf{O}$, 6, \mathbf{CO}_2 and 7, \mathbf{N}_2 . The coal and biomass volatiles pseudo-species are a polymer vapour of carbon, hydrogen, oxygen and nitrogen, and the structure of their combination determines the stoichiometric ratios of the reaction. Typically, the volatiles will be grouped per carbon so $v'_{1,1}$, $v'_{2,2}$, $v''_{1,4}$ and $v''_{2,4}$ will be unity. The first six species mass fractions evolutions are solved using equations [3.10] and [3.11], the \mathbf{N}_2 mass fraction is then the difference from unity. Ambient air intake ensures \mathbf{N}_2 will be the dominant species and so this method minimises rounding error.

The eddy-dissipation reaction method is mixing limited and so the rate of production (and consumption) of a species is controlled by the lesser rate, from the following equations, which represent, respectively, the transport of necessary reactant species and transport of hot product species required for ignition:

$$R_{r,j} = Av'_{r,j} M_j \rho \frac{\varepsilon}{k} \min_R \left(\frac{y_R}{v'_{r,R} M_R} \right) \quad [3.13]$$

$$R_{r,j} = ABv'_{r,j} M_j \rho \frac{\varepsilon}{k} \frac{\sum_P y_P}{\sum_i^N v''_{r,i} M_i} \quad [3.14]$$

where the terms represent: volumetric rate of production of species j in reaction r , $R_{r,j}$ [$\text{m}^{-3}\text{s}^{-1}$], mixing constant, $A = 4$, molar mass of species j , M_j [$\text{kg}\cdot\text{mol}^{-1}$], turbulent dissipation rate, ε [m^2s^{-3}], turbulent kinetic energy, k [m^2s^{-2}], mixing constant, $B = 0.5$. Subscripts i and j mean any species, subscript R means a reactant species and subscript p means a product species. Therefore it can be seen that the final term in equation [3.13] is the minimum ratio from all reactant species and the final term in

equation [3.14] is the sum of all product mass fractions over the total mass of products from all species ($v''_{r,i}$ will be zero for each species that is not a product in reaction r).

3.2 Computational Particle Dynamics

3.2.1 Lagrangian Particle Treatment

As previously discussed, in Chapter 1, there are two methods of modelling particles submerged in a fluid continuum, namely in the Lagrangian and Eulerian frames of reference. The naming convention comes from the renowned mathematicians' disparate use of local or global reference frames for fluid mechanics. Lagrange considered a reference frame that moves with the fluid particle, likened to a river from an observer in an unmoored boat, and Euler considered a reference frame that was fixed but the fluid flowed past, likened to a river from an observer on a bridge. Solid or fluid (droplet or bubble) particles can be handled by either method, however the interface between the particle and the fluid is not simulated in either case. In practical engineering cases the designation of particle would be an object too small and numerous to be included in a dynamic mesh for direct numerical simulation (DNS), which is why the modelling methods were developed.

The focus of the thesis is upon Lagrangian particle tracking. In this method particles are point-masses which travel through the FVM mesh but are separate to the continuum in the Eulerian fluid calculations. To describe the problem physically, mass, momentum and energy conservations must be calculated for the particles. In simple non-reacting particle suspensions only the drag, which is the acceleration due to momentum sources from the fluid, is required. Conversely the impact of the particle on the fluid must be reflected by source terms in the fluid's conservation equations for strict physical accountability. In practice the physical problem is truncated so that phenomena of lesser significance are not modelled. For example, the pressure effects within the fluid due to the particles' volume are not calculated and in general the fluid momentum sink that the "dragged" particles represent is not relayed back to the flow. It is also standard in Lagrangian particle tracking for an individual particle trajectory calculation, considered representative, to be used for multiple identical particles.

Essentially the continuous particle size distribution is “meshed” by choosing nodes in the form of representative particles.

The governing equation for the motion of a particle in Lagrangian coordinates is given by:

$$\frac{d\vec{u}_p}{dt} = \vec{f}_G + \vec{f}_D + \vec{f}_L \quad [3.15]$$

where the mass of the particle, m_p [kg], has been omitted as it would be common to all terms. The terms on the right hand side (RHS) are respectively, the specific gravimetric force, specific drag force and specific lift force.

The specific gravitational force is given by:

$$\vec{f}_G = \vec{g} \left(1 - \frac{\rho_f}{\rho_p} \right) \quad [3.16]$$

where ρ_f [kgm⁻³], is the fluid density and ρ_p [kgm⁻³], is the particle density.

A basic discretisation of Newton’s second law of motion, considering the forces upon the particle in equation [3.15] is the Euler implicit scheme presented as follows (ANSYS, 2009a):

$$\vec{u}_p^{n+1} = \frac{\vec{u}_p^n + \Delta t \left(\vec{f}_G + \vec{f}_L + \frac{\vec{u}_p^n}{\tau_p} \right)}{1 + \frac{\Delta t}{\tau_p}} \quad [3.17]$$

where \vec{u}_p [ms⁻¹], is the particle velocity [ms⁻¹], the superscripts n and $n+1$ represent “at the present time” (timestep n) and “after the next timestep” (timestep $n+1$), respectively, Δt [s], is the timestep, and τ_p [s], is the particle relaxation time based on Stokes’ drag given below:

$$\tau_p = \frac{\rho_p d_p^2}{18\mu} \quad [3.18]$$

where d_p [m], is the particle diameter, and μ [kgm⁻¹s⁻¹], is the molecular viscosity of the fluid.

3.2.2 Spherical Particle Drag

The drag force calculated for the force balance, ordinary differential equation (ODE), that is solved, assuming constant acceleration over minimal timesteps (Laín and Sommerfeld, 2008), is:

$$\vec{F}_D = \frac{3}{4} \frac{\rho_f}{\rho_p d_p} m_p C_D \vec{U} |\vec{U}| \quad [3.19]$$

where \vec{U} [ms^{-1}] is the relative velocity of the fluid to the particle ($\vec{U} = \vec{u}_f - \vec{u}_p$). The drag coefficient, C_D , is dependent upon the flow behaviour which is broadly split into two different ‘turbulence regimes’ characterised by the particle Reynolds number, Re_p , namely:

$$\text{Re}_p \equiv \frac{\rho_f d_p |\vec{U}|}{\mu} \quad [3.20]$$

introduced as analogue to Reynolds’ dimensional analysis of pipe flow. ρ_f [kgm^{-3}], is the fluid density.

The two regimes are high (also called Newton’s or ballistic) and low (otherwise Stokes’ or creeping) Reynolds numbers. Although spheres have a simple shape, and are seen to find stable direct relationships to the square of the relative velocity within Newton’s regime, the behaviour of the drag coefficient in Stokes’ (low Re_p) regime must always be divulged to the numerical model by way of an empirical data fit. Combining equations [3.19] and [3.20] the specific drag force, \vec{f}_D , as it is usually formed is given by:

$$\vec{f}_D = \frac{\vec{F}_D}{m_p} = \frac{18\mu}{\rho_p d_p^2} \frac{C_D \text{Re}_p}{24} \vec{U} \quad [3.21]$$

the unsimplified fractional coefficient is retained since the second factor on the RHS cancels to unity with input of the drag coefficient under Stokesian flow.

The different empirical functions used to describe the coefficient of drag in the most common drag laws over the usual practical range of Reynolds numbers are presented in Figure 3.1.

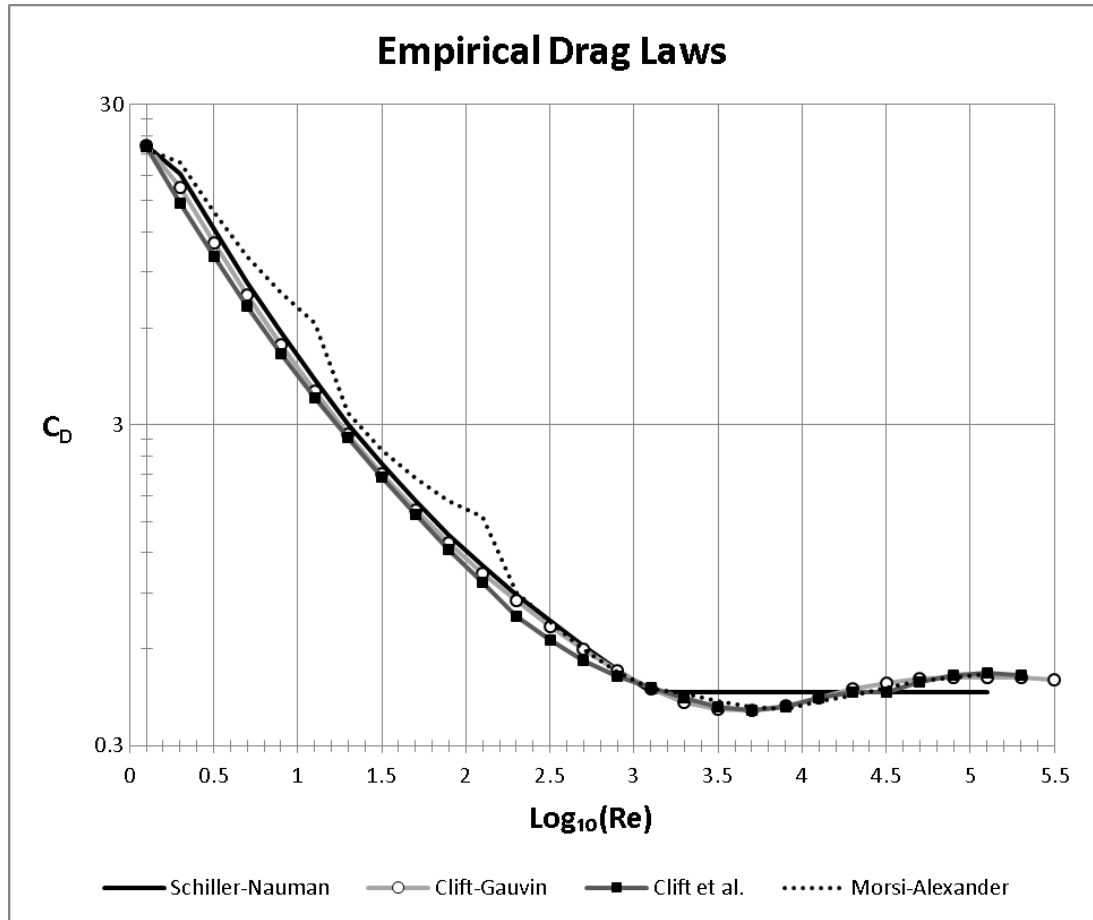


Figure 3.1 Empirical drag laws.

Describing the coefficient of drag as a function of particle Reynolds number.

The default drag law in ANSYS Fluent (for spherical particles) is that of Morsi and Alexander (1972), which uses a piecewise set of quadratic equations (argument: Re_p^{-1}) given by:

$$C_D = \begin{bmatrix} 0 & 24 & 0 \\ 3.69 & 22.73 & 0.0903 \\ 1.222 & 29.1667 & -3.8889 \\ 0.6167 & 46.5 & -116.67 \\ 0.3644 & 98.33 & -2778 \\ 0.357 & 148.62 & -4.75 \times 10^4 \\ 0.46 & -490.546 & 5.787 \times 10^5 \\ 0.5191 & -1662.5 & 5.4167 \times 10^6 \end{bmatrix} \times \begin{cases} 1 \\ Re_p^{-1} \\ Re_p^{-2} \end{cases} \quad [3.22]$$

each piecewise row is individually multiplied by the parameter vector depicted. As can be seen, the first set corresponds to Stokes' solution ($24 Re_p^{-1}$).

However, probably the most popular drag law (Yasuna *et al.*, 1995, Rundqvist *et al.*, 2005, Saffar-Avval *et al.*, 2007, and Loth, 2008), due to its single equation covering the transitional spectrum of particle Reynolds numbers is the Schiller-Naumann, given by:

$$\begin{aligned} C_D &= 24 \text{Re}_p^{-1} \left(1 + 0.15 \text{Re}_p^{0.687}\right) = 24 \text{Re}_p^{-1} k_S & [0 < \text{Re}_p \leq 10^3] \\ C_D &= 0.44 & [10^3 \leq \text{Re}_p < 10^5] \end{aligned} \quad [3.23]$$

the multiple of the Stokes' drag coefficient (in parentheses) can be considered the Stokes' drag correction, k_S , as this is used to extend the Reynolds number limit, beneath which the drag law is applicable, beyond the linear drag regime limit. Strictly the limit for application of the Schiller-Naumann is given as $\text{Re}_p \leq 800$, however the range is regularly extended up to 10^3 . This is still inappropriate for certain engineering applications so an additional piecewise condition, for higher values of Re_p by the use of the empirically measured approximately constant Newton's drag coefficient of 0.44 for $10^3 \leq \text{Re}_p < 10^5$ (Laín and Sommerfeld, 2008) is implemented. It is feasible to disregard the upper limit of 10^5 as particle multiphase flow applications do not reach the critical transition at the upper end of Newton's regime, $\text{Re}_p > 10^5$ (Loth, 2008). On this point, the termination of Morsi and Alexander's (1972) piecewise drag law, at $\text{Re}_p = 10^5$, safely within subcritical flow, is presumably due to the practical range of interest (particle collisions with bluff aerofoils). The Schiller-Naumann itself is still used beyond the recommended range to bridge the transition between the Stokes' and Newton's regimes with a negligible discontinuous 'dog leg' behaviour at $\text{Re}_p = 10^3$. Therefore the lower Reynolds number range in equation [3.23] may instead be considered to be $\text{Re}_p < 10^3$. A further law that spans the sub-critical regimes is the Clift-Gauvin drag law is given by:

$$C_D = 24 \text{Re}_p^{-1} \left(1 + 0.1 \text{Re}_p^{0.687}\right) + \frac{0.42}{1 + 4.25 \times 10^4 \text{Re}_p^{-1.16}} \quad [0 < \text{Re}_p \leq 10^5] \quad [3.24]$$

this is a correction to the Schiller-Naumann drag law and covers the same particle Reynolds number domain, in a single continuous function, as the discrete Schiller-Naumann (equation [3.22]), with similar accuracy to the original (Clift *et al.*, 1978).

Clift *et al.* (1978) also give a ten interval piecewise fit (with discontinuities at interval boundaries of less than 1%) for the full range of values of Re_p , certain intervals of which have been adopted for the individual application of interest (Arsenijovic *et al.*, 1999, and Göz *et al.*, 2004). Eight intervals, bounded by finite non-zero extents, span $[10^{-2} < Re_p < 10^6]$, below this range of values of Re_p Oseen's inverse linear fit is suitable and above this range another inverse linear fit is used. A presumed dearth of experimental data prevents further compartmentalisation of the range but also reflects sensible constraints upon the investigation.

3.2.3 Non-Spherical Drag

A number of methods of modelling the drag experienced by a non-spherical particle may be employed depending on the shape description used, as discussed in section 2.2.

Haider and Levenspiel's (1989) non-spherical drag law is popular for fixed-orientation particles. As described in section 2.2.2 it augments the spherical drag relative to the particle's sphericity, Φ , defined below:

$$\Phi \equiv \frac{A_{EVS}}{A_s} \quad [3.25]$$

where sphericity is the ratio of the surface area of an equivalent volume sphere (EVS), A_{EVS} [m^2], to the surface area of the non-spherical particle, A_s [m^2].

The amplification of drag response is fully accounted in the coefficient of drag:

$$C_D = \frac{24}{Re_p} \left(1 + e^a Re_p^b \right) + \frac{e^c Re_p}{e^d + Re_p} \quad [3.26]$$

$$a = 2.3288 - 6.4581\Phi + 2.4486\Phi^2$$

$$b = 0.0964 + 0.5565\Phi$$

$$c = 4.9050 - 13.8944\Phi + 18.4222\Phi^2 - 10.2599\Phi^3$$

$$d = 1.4681 + 12.2580\Phi - 20.7322\Phi^2 + 15.8855\Phi^3 \quad [3.27]$$

Ganser (1993) provides an alternative method based on the normalised drag response of the particle under Stokes' and Newton's regimes:

$$\frac{C_D}{K_2} = \frac{24}{\text{Re}_K} \left(1 + 0.1118 \text{Re}_K^{0.6567} \right) + \frac{0.4305 \text{Re}_K}{3305 + \text{Re}_K} \quad [3.28]$$

$$\text{Re}_K \equiv \text{Re}_p K_1 K_2 \quad [3.29]$$

where Re_K is the effective Reynolds number and K_1 and K_2 are, respectively, the Stokes' and Newton's shape factors, which can be directly determined by experiment. Their definitions follow:

$$C_{D,S} \equiv \frac{C_{\text{EVS},S}}{K_1} = \frac{24}{\text{Re}_p K_1} \quad [\text{Re}_p \ll 1] \quad [3.30]$$

$$C_{D,N} \equiv K_2 C_{\text{EVS},N} = 0.463 K_2 \quad [\text{Re}_p = 10^4] \quad [3.31]$$

where the subscripts, $_S$ and $_N$, after the drag coefficients denote under the Stokes' and Newton's drag regimes respectively. C_{EVS} is the drag coefficient of the particles' equivalent volume sphere. As sphericity, Φ , is the more widely used shape factor, Ganser also includes predictions for the Stokes' and Newton's shape factors, K_1 and K_2 respectively, from this for a general non-spherical shape:

$$K_1 = \left(\frac{1}{3} \frac{d_{\text{EPS}}}{d_{\text{EVS}}} + \frac{2}{3} \Phi^{-0.5} \right)^{-1} - 2.25 \frac{d_{\text{EVS}}}{D} \quad [3.32]$$

$$\log_{10}(K_2) = 1.8148(-\log \Phi)^{0.5743} \quad [3.33]$$

where d_{EPS} and d_{EVS} are the equivalent projected area sphere diameter and equivalent volume sphere diameter. The ratio of these two lengths is a measure of the projected area of the non-spherical particle (perpendicular to the relative flow velocity) to that of its EVS. In this way the orientation of the particle in the flow affects its drag. D [m], is the tube diameter of the settling device used in the experiments. This value is not generally recorded in computational domains and may be time consuming to obtain for complex geometries, however the last term of equation [3.32] will be $\approx 10^{-2}$ for PF in centimetre diameter pipes (which could be expected to have high carrier fluid velocities

and therefore correspondingly high Re_p) whereas the first term on the RHS will be unity for spheres and generally greater for non-spheres.

3.2.4 Spherical Rotation

As seen in sections 3.2.2 and 3.2.3 on spherical and non-spherical drag, instantaneous forces are modelled by an empirical fit or theoretical equation. Force balances, by which the particle's kinetics is described, are performed at discretised points. The calculated acceleration is assumed constant until the next force balance. To incorporate particle rotation simulation into this approach, torque balances must also be conducted. The characteristic of response in time for angular momentum exchange between the fluid and particle phases is described by the particle rotational relaxation time, τ_ω [s]. This is the inverse of the logarithmic rate for the relative angular velocity between the fluid and particle to decay to $\bar{\omega}_0 e^{-1}$ due to viscous interaction. Where $\bar{\omega}_0$ [s^{-1}] is the initial angular velocity. This response characteristic is used as the maximum stable timestep length for numerical modelling. The rotational relaxation time under Stokes' rotation and Newton's rotation regimes (these do not coincide with the translational drag regimes) are presented below:

$$\tau_\omega = \frac{\rho_p d_p^2}{60\mu} \quad [Re_r \leq 32] \quad [3.34]$$

$$\tau_\omega = \frac{\pi\rho_p d_p^2}{120.375\mu k_R} \quad [32 < Re_r \leq 1000] \quad [3.35]$$

the derivations of equations [3.34] and [3.35] are provided in Appendix I.

The particle rotation can be influenced by the fluid phase in a similar manner to translation, such as angular drag and instantaneous relative angular velocity due to turbulent fluctuations, through tangential forces at the surface of the particle in a laminar boundary layer or turbulent wake.

As the viscous fluid tends to damp the particle rotation, as with translational drag, the pertinent dimension for the rate of this phenomenon is the relative angular velocity between the particle surface and contact layer of fluid. Laín and Sommerfeld (2008)

define the fluid angular velocity as half the fluid vorticity, this can be facilitated by assuming rigidly rotational flow at the particle surface:

$$\vec{\zeta} \equiv \nabla \times \vec{u}_f = 2\vec{\omega}_f \quad [3.36]$$

where $\vec{\zeta}$ [$^{\circ}\text{s}^{-1}$], is the fluid vorticity and $\vec{\omega}_f$ [$^{\circ}\text{s}^{-1}$], is the fluid angular velocity.

The fluid rotation relative to the particle is then simply:

$$\vec{\Omega} \equiv \vec{\omega}_f - \vec{\omega}_p \quad [3.37]$$

where $\vec{\Omega}$ [$^{\circ}\text{s}^{-1}$] is the relative angular velocity and $\vec{\omega}_p$ [$^{\circ}\text{s}^{-1}$] is the particle angular velocity.

A new flow parameter, the rotational Reynolds number (Re_r), is fashioned for dimensional analysis of ‘angular drag’:

$$\text{Re}_r \equiv \frac{\rho_f d_p^2 |\vec{\Omega}|}{\mu} \quad [3.38]$$

Rubinow and Keller (1961) do not explicitly state a coefficient of rotation, for creeping rotational flow, but it is instead found by the factor through which the standard torque equation must be multiplied to agree with the linear relationship presented in their paper, namely equation [3.39]:

$$\vec{T}_{\text{L\&S}} = \frac{\rho_f}{2} \left(\frac{d_p}{2} \right)^5 C_R \vec{\Omega} |\vec{\Omega}| = \frac{\rho_f d_p^5}{64} C_R \vec{\Omega} |\vec{\Omega}| \quad \vec{\Omega} = \vec{\omega}_f - \vec{\omega}_p \quad [3.39]$$

$$\vec{T}_{\text{R\&K}} = -8\pi\mu a^3 \vec{\Omega} = -\pi\mu d_p^3 \vec{\Omega} \quad \vec{\Omega} = \vec{\omega}_p \quad [3.40]$$

$$\begin{aligned} \text{if } \vec{T}_{\text{L\&S}} &= \vec{T}_{\text{R\&K}} \\ \Rightarrow \frac{\rho_f d_p^5}{64} C_R \vec{\Omega} |\vec{\Omega}| &= \pi\mu d_p^3 \vec{\Omega} \quad \vec{\Omega} = \vec{\omega}_f - \vec{\omega}_p \quad [3.41] \end{aligned}$$

$$\Rightarrow C_R = \frac{64\pi\mu d^3 \vec{\Omega}}{\rho_f d_p^5 \vec{\Omega} |\vec{\Omega}|} = \frac{64\pi\mu}{\rho_f d_p^2 |\vec{\Omega}|} = \frac{64\pi}{\text{Re}_r} \quad [0 < \text{Re}_r \leq 32]$$

where \vec{T} [Nm] is the torque due to viscous damping, the subscripts $_{\text{L\&S}}$ and $_{\text{R\&K}}$ denote Laín and Sommerfeld (2008), and Rubinow and Keller (1961), respectively, a [m] is the particle radius and C_R is the coefficient of rotation. The different selection of

definition for the effective rotation, $\vec{\Omega}$, in these two studies causes the same symbol to have opposing sign as can be seen from the right-aligned conditions. Rubinow and Keller (1961) used an assumption of irrotational fluid, $\vec{\omega}_f = 0$, under the creeping flow conditions considered.

A higher Reynolds number rotational drag regime is taken from Dennis *et al.* (1980) and is the result of an empirical fit, which is equated below to the result presented by Laín and Sommerfeld (2008):

$$C_R = \frac{6.45}{\text{Re}_{r(D)}^{0.5}} + \frac{32.1}{\text{Re}_{r(D)}} = \frac{12.9}{\text{Re}_{r(L\&S)}^{0.5}} + \frac{128.4}{\text{Re}_{r(L\&S)}} \quad [32 < \text{Re}_{r(L\&S)} \leq 1000] \quad [3.42]$$

where the subscripts _(D) and _(L&S) denote Dennis *et al.* (1980) and Laín and Sommerfeld (2008), respectively. The differing notation that results in equation [3.42] is discussed in section 2.1.5. Adopting Laín and Sommerfeld's (2008) notation and implementing a Schiller-Naumann style "Stokes' correction to rotation", k_R , the following form is taken forwards:

$$C_R = \frac{12.9}{\text{Re}_r^{0.5}} + \frac{128.4}{\text{Re}_r} = \frac{128.4}{\text{Re}_r} k_R \quad [32 < \text{Re}_r \leq 1000] \quad [3.43]$$

$$k_R = \left(1 + \frac{12.9}{128.4} \text{Re}_r^{0.5} \right)$$

3.2.5 Spherical Lift

Saffman Lift Force

The form of the Saffman lift force is taken from Mei's (1992) extension to Saffman's creeping experiments (Laín and Sommerfeld, 2008). Saffman presented, "*The lift [force] on a small sphere in a slow shear flow.*" Which is recast into the conventional nomenclature below:

$$\vec{F}_S = 1.615(\rho_f \mu)^{0.5} d_p^2 |\vec{\omega}_f|^{0.5} \vec{U} \times \text{sign}(\vec{\omega}_f) \quad [3.44]$$

where \vec{F}_S [N], is the Saffman lift force. Fluid elements are induced to spin by the viscous interaction of shear layers and therefore the vorticity of the fluid is related to the gradient of its translational velocity. Since the fluid vorticity is the curl of the fluid translational velocity, from equation [3.36], the cross product on the RHS of equation

[3.44] gives the velocity shear in the correct direction which will be perpendicular to the flow in the plane described by this direction and the normal to the closer wall.

Mei (1992) assigned a correction to Saffman's classical result to account for lift behaviour at greater Re_p . Initially an additional dimensionless number is introduced:

$$Re_s = \frac{\rho_f d_p^2 |\vec{\omega}_f|}{\mu} \quad [3.45]$$

this is a dimensionless number to characterise the shearing velocity gradient in the order of the particle, here named the shear Reynolds number, Re_s . It was introduced by Mei (1992). A clarification of the notation used in this thesis and by Mei (1992) is presented here: the notation " Re_s " was used by Mei (1992) in place of " Re_p " (particle Re) as used in this study. Mei's (1992) Re_G (perhaps gradient Re) is that which relates to the current Re_s (shear Re). It is seen that Mei's (1992) correction varies with a dimensionless shear rate, Σ , which was implemented by Dandy and Dwyer (1990) and defined below:

$$\Sigma = \frac{Re_s}{2Re_p} = \frac{d_p |\vec{\omega}_f|}{2|\vec{U}|} \quad [3.46]$$

here capital sigma, Σ , has been selected for a unique symbol with mnemonic "s" towards shear. Dandy and Dwyer (1990) and Mei (1992) selected α , whilst Laín and Sommerfeld (2008) chose β , and Oesterlé and Bui Dinh (1998) γ , for this parameter as well as separate definitions which are at first unrecognisable as the same item.

Following this discussion it is understood that Laín and Sommerfeld (2008) include a coefficient of Saffman lift, C_s , which must be unity under the creeping shear flow conditions of the previous experimental work. Therefore combining equations [3.44] and [3.45]:

$$\vec{F}_S = 1.615 \mu Re_s^{0.5} d_p C_s \frac{\vec{U} \times \vec{\omega}_f}{|\vec{\omega}_f|} \quad [3.47]$$

the empirical coefficient at the start of the RHS, 1.615, is the lift coefficient from the earlier, low Re_s , expression brought forward from equation [3.44], so the lift coefficient, C_s , is actually Mei's (1992) ratio of lift coefficient to that of Saffman. The

functions for C_S were solved to fit the known tendency to unity as $Re_p \rightarrow 0$ with the numerical results at higher Re_p (Dandy and Dwyer, 1990) given below:

$$C_S = \left(1 - 0.3314\Sigma^{0.5}\right)e^{(-0.1Re_p)} + 0.3314\Sigma^{0.5} \quad [0 < Re_p \leq 40] \quad [3.48]$$

[0.005 < Σ ≤ 0.4]

$$C_S = 0.0524(Re_p \Sigma)^{0.5} \quad [40 < Re_p] \quad [3.49]$$

[0.005 < Σ ≤ 0.4]

Magnus Lift Force

As with the ‘angular drag’, in the previous section 2.2.4, Rubinow and Keller’s (1961) formation was adjusted to include the angular velocity of the fluid relative to the particle. Oesterlé and Bui Dinh (1998) found a coefficient of Magnus lift, C_M , which is stated to have fair application for $Re_p \leq 2000$, however the graphical comparison only contains data in the range of $10 \leq Re_p < 140$ and therefore its implementation beyond these limits is not endorsed. Due to lack of investigation Laín and Sommerfeld (2008) adopted the higher ($Re_p < 2000$) limit and assumed validity extending to no relative motion. The resulting Magnus lift force is given by:

$$\vec{F}_M = \frac{\pi}{8} \rho_f d_p^3 \frac{Re_p}{Re_r} C_M (\vec{U} \times \vec{\Omega}) \quad [3.50]$$

where \vec{F}_M [N] is the Magnus lift force and C_M is the coefficient of Magnus lift.

It is difficult to fully track the adjustment between Laín and Sommerfeld’s (2008) force formation and coefficient of Magnus lift expression and those presented in Rubinow and Keller (1961) and Oesterlé and Bui Dinh (1998). This is because dependence is shifted from the shear (Re_s) to the rotational (Re_r) Reynolds number which uses relative angular velocity as the characteristic (inverse) time instead of absolute fluid angular velocity. Respecting this thesis’ conventions the force expressed in Rubinow and Keller (1961) is found to be identical, to equation [3.50], except for the lift coefficient and ratio of translational to rotational particle Re ($C_M Re_p / Re_r$).

Next will be presented Oesterlé and Bui Dinh's (1998) followed by Laín and Sommerfeld's (2008) declarations of C_M :

$$\log\left(\frac{C_M}{0.45}\right) = -0.075\Sigma^{0.4} \text{Re}_p^{0.7} \log(2\Sigma - 0.45) \quad [10 \leq \text{Re}_p < 140] \quad [3.51]$$

$$\log\left(\frac{C_M}{0.45}\right) = -0.05684 \text{Re}_r^{0.4} \text{Re}_p^{0.3} \log\left(\frac{\text{Re}_r}{\text{Re}_p} - 0.45\right) \quad [0 \leq \text{Re}_p < 2 \times 10^3] \quad [3.52]$$

where Σ is given in equation [3.46]. Equations [3.51] and [3.52] are equivalent when $\text{Re}_s = \text{Re}_r$, which is true under irrotational particle conditions.

3.2.6 Inter-particle Collisions

This section outlines the mathematical equations for a stochastic inter-particle collision method akin to that of Sommerfeld (1991). Four steps are followed during the particle trajectory calculation: Probability, Randomisation, Collision and Resolution.

At each calculation step a stochastically prescribed collision object (characteristic local particle) is provided, for which a probability of collision by the potential collisions subject (tracked particle) can be made. Relevant particle variables are stored in the Eulerian fluid cells as if they were field variables so that they may be accessible to the Lagrangian particle during trajectory calculations. Velocity, size and density of the collision object in addition to the local particle concentration are necessary for the calculation of collision probability. The probability of collision within a timestep is simply the collision frequency multiplied by the timestep in question. This requires that the timesteps are short enough in length to allow probability of below unity:

$$P_c = f_c \Delta t = \frac{\pi}{4} (d_s + d_o)^2 |\vec{u}_s - \vec{u}_o| n_p \Delta t \quad \Delta t \ll \frac{1}{f_c} \quad [3.53]$$

where P_c is the probability of collision, f_c [Hz] is the frequency of collision, Δt [s] is the particle timestep, d_s and d_o [m] are the collision subject and object diameters, respectively, \vec{u}_s and \vec{u}_o [ms^{-1}] are the collision subject and object velocities, respectively, and n_p [m^{-3}] is the particle concentration. The beginning of the right-most RHS in equation [3.53], $0.25\pi(d_s + d_o)^2$, describes the circular area about the centre of a local particle (collision object) in which a collision would occur. Also $|\vec{u}_s - \vec{u}_o| \Delta t$ may

be considered as the displacement of the tracked particle (collision subject) during a timestep. Therefore the full RHS is the sum of collision cylinder volumes apparent before all the collision objects on a volumetric basis. The binary collision assumption introduced in section 2.1.6 requires that no collision cylinders overlap and should be facilitated by limiting the timestep. This is seen in the right-aligned condition to equation [3.53]. The sum of collision cylinder volumes exceeding the cell volume or the probability exceeding unity are equivalent consequences of violation.

Sommerfeld (2003) gives a method to correlate the instantaneous velocities of the collision subject and object:

$$\vec{u}_o = \mathbf{R}(\text{St})\vec{u}_s + \vec{u}_{rms} \sqrt{1 - \mathbf{R}(\text{St})^2} \xi_N \quad [3.54]$$

where \vec{u}_s represents the instantaneous velocity, $\mathbf{R}(\text{St})$ is a correlation to the Stokes number given below, \vec{u}_{rms} [ms^{-1}] is the average of the velocity fluctuation and ξ_N is a random number sampled from a normal distribution.

$$\begin{aligned} \log \mathbf{R}(\text{St}) &= -0.55\text{St}^{0.4} \\ \text{St} &= \frac{\tau_p}{T_t} \end{aligned} \quad [3.55]$$

where τ_p [s] is the particle relaxation time and T_t [s] the integral timescale of turbulence (Sommerfeld, 2003).

If no collision is randomly determined the collision scheme ends for that particle trajectory calculation. However, following a true evaluation of the collision criterion, P_c , (uniform random number of interval [0 1] is less than collision probability) the collision subject (currently tracked particle) is given a stochastic radial and angular displacement within the ‘collision cylinder’. The random cylindrical coordinates, r [m] and ϕ [°], of the collision are given by:

$$r = R_c \xi_{U1} \quad [3.56]$$

$$\phi = 2\pi \xi_{U2} \quad [3.57]$$

where ξ_U is a uniform random number interval [0 1], the numbered subscripts simply denote separate value-generations of uniform random number, and R_c [m] is the collision cylinder radius, this is equal to the sum of the collision subject and collision

object radii, however its value is not required. Equation [3.56] will be superseded by equation [3.58].

The motion of the collision subject is resolved in the direction of relative velocity between the colliding particles with stationary collision object. This yields the axial direction of the collision cylinder, perpendicular to which a circular cross-section is described by a locus equal to the sum of the colliding particles' radii about the axis (R_c). Only one coordinate must be provided stochastically, the axial position of the collision subject within the collision cylinder, at point of contact with the collision object, is directly dependent upon its radial displacement. The relative velocity (in the axial direction) is then decomposed into radial and tangential components at the collision subject's surface (spherical particle's radial direction, not collision cylinder's). These collision coordinates are used to resolve the post collision velocity back into global coordinates and also the collision angle which determines the normal and tangential components at pre-collision is found below:

$$\theta = \sin^{-1}\left(\frac{r}{R_c}\right) = \sin^{-1} \xi_{U_1} \quad [3.58]$$

$$u_n = |\vec{U}| \cos \theta \quad [3.59]$$

$$u_t = |\vec{U}| \sin \theta \quad [3.60]$$

where θ [$^\circ$] is the angle of incidence of the collision, u_n and u_t [ms^{-1}] are the normal and tangential velocities, respectively, and $|\vec{U}|$ is the magnitude of the relative velocity of the collision. The uniform random number, ξ_{U_1} , is the same value as in equation [3.56]. The velocity components, u_n and u_t , have dropped the bar because they are considered scalar existing as they do only in their individual fixed vectoral direction. In three dimensions there must be three principal directions, in general the tangential motion might contain two components in the plane described by the normal direction. In fact it has already been seen in equations [3.59] and [3.60], the magnitudes of translational velocity components may be resolved in a 2D plane, however, the impulsive equations presented below have maintained Oesterlé and Petitjean's (1993) local 3D form. This is aligned to the normal and tangential collision directions that

account for the full pre-collision translational motion. However, a second tangential direction, perpendicular to both of these, must also be included. At the pre-collision stage this secondary tangential direction will contain zero translational velocity but the instantaneous velocity at the colliding particle's surface may have a component in this direction due to particle rotation. Unless indexed the subscript i is to mean the magnitude acting in the resultant tangential direction.

The post collision velocities are calculated using the following equations as functions of the three translational impulses (Oesterlé and Petitjean, 1993):

$$u_n = u_{n0} + \frac{J_n}{m_s} = u_{n0} \left(1 - \frac{1+e}{1+M} \right) \quad [3.61]$$

$$u_{ti} = u_{ti0} + \frac{J_{ti}}{m_s} \quad [3.62]$$

$$u_{tj} = u_{tj0} + \frac{J_{tj}}{m_s} \quad [3.63]$$

$$\omega_n = \omega_{n0} \quad [3.64]$$

$$\omega_{ti} = \omega_{ti0} - \frac{5J_{tj}}{m_s d_s} \quad [3.65]$$

$$\omega_{tj} = \omega_{tj0} + \frac{5J_{ti}}{m_s d_s} \quad [3.66]$$

$$M = \frac{m_s}{m_o} \quad [3.67]$$

where the subscript $_0$ denotes the pre-collision property, subscripts, i and j , are appended to the tangential velocity as there are two perpendicular tangential velocities acting in three dimensional space, J_n [Ns], is the normal impulse, m_s [kg], is the mass of the collision subject, M , is the ratio of the masses of the collision subject to collision object, J_i [Ns], is the tangential impulse and, ω_n and ω_i [$^c s^{-1}$], are normal and tangential angular speeds, respectively. Note the opposing indices of the impulses in the angular velocity equations [3.65]&[3.66] because the perpendicular impulse induces angular motion.

In three dimensions the rotating case is simplified by considering a rotated frame of reference with a component collinear to the displacement vector between the colliding particles' centres (as described for the 'collision cylinder' above), whereby rotation about this is perfectly elastically conserved (small contact patch hypothesis of Oesterlé and Petitjean (1993), manifest in the trivial equation [3.64]).

Applying Coulomb's law of friction, two different modes of collision are assumed to exist, sliding and non-sliding, depending on the tangential momentum (Sommerfeld, 2001). In a collision cylinder of radius R_c , a radial displacement of 0 would instigate a direct collision with normal (radial in particle coordinates) velocity equal to the relative velocity, whereas a radial displacement of R_c would lead to a skimming collision with tangential velocity equal to the relative velocity. Less oblique collisions (a thick angle using snooker terminology) ensure the normal force for full tangential and angular momentum exchange due to friction, whereas glancing (thin) collisions can transfer only a proportion of the tangential and angular momentum relative to the dynamic friction.

For rotational particles, the non-sliding condition requires adjustment to represent the absolute tangential velocity at the particle surface as shown below (Oerstelé and Petitjean, 1993):

$$\frac{2u_{t0} - d_s \omega_{t0}}{2u_{n0}} < \frac{7}{2} \mu_s (1 + e) \quad [3.68]$$

where μ_s is the coefficient of static friction between the two particle surfaces and e is the coefficient of restitution and it is understood that u_t and ω_t are the, respective, resultant magnitudes of the relative tangential translational velocity and angular velocity about this resultant direction. The form of equation [3.68] comes from comparison of the relative magnitudes of the normal and tangential impulses, these being directly proportional the normal and friction forces, respectively. Therefore a non-sliding collision takes place if the tangential impulse is less than the friction transmitted due to the normal impulse.

The components of collision impulse are given here:

$$J_n = -(1+e)u_{n0} \frac{m_s}{1+M} \quad [3.69]$$

$$J_{ti} = -\frac{1}{7}(W_i) \frac{m_s}{1+M} \quad \frac{2u_{t0} - d_s \omega_{t0}}{2u_{n0}} < \frac{7}{2} \mu_s (1+e) \quad [3.70]$$

$$J_{tj} = -\frac{1}{7}(W_j) \frac{m_s}{1+M} \quad \frac{2u_{t0} - d_s \omega_{t0}}{2u_{n0}} < \frac{7}{2} \mu_s (1+e) \quad [3.71]$$

$$J_{ti} = -\mu_d \left| (1+e)u_{n0} \frac{m_s}{1+M} \right| Y_i \quad \frac{7}{2} \mu_s (1+e) < \frac{2u_{t0} - d_s \omega_{t0}}{2u_{n0}} \quad [3.72]$$

$$J_{tj} = -\mu_d \left| (1+e)u_{n0} \frac{m_s}{1+M} \right| Y_j \quad \frac{7}{2} \mu_s (1+e) < \frac{2u_{t0} - d_s \omega_{t0}}{2u_{n0}} \quad [3.73]$$

where W_i [ms^{-1}], is the instantaneous particle surface speed at the contact patch in the indexed (tangential) direction, μ_d is the coefficient of dynamic friction, $\omega_{s(i/j)}$ and $\omega_{o(i/j)}$ are, respectively, the angular speeds of the collision subject and object about the indexed (tangential) components and, $Y_{(i/j)}$ is the ratio of the instantaneous particle surface velocity at the contact patch in the indexed (tangential) component direction to the magnitude of particle surface velocity at the contact patch:

$$Y_i = \frac{W_i}{\sqrt{W_i^2 + W_j^2}} \quad [3.74]$$

$$W_i = 2u_{ti0} + d_s \omega_{sj} + d_o \omega_{oj} \quad [3.75]$$

$$W_j = 2u_{tj0} - d_s \omega_{si} - d_o \omega_{oi} \quad [3.76]$$

all terms have previously been introduced in this section. Note that the perpendicular tangential velocities are present in the surface speed terms, $W_{(i/j)}$ and that those about the i direction are negative in the j direction. This is an artefact of rotations about the right-handed coordinate system, n - t_i - t_j .

The normal and primary tangential (t_i) velocity components can be easily resolved back into relative velocity coordinates, through $-\theta$ [°], defined in equation [3.58]:

$$u_A = u_n \cos \theta + u_{t_i} \sin \theta \quad [3.77]$$

$$u_B = u_n \sin \theta + u_{t_i} \cos \theta \quad [3.78]$$

These relative velocity coordinates are then resolved into an arbitrarily aligned plane in global coordinates. This is acceptable as long as it is consistent. Therefore an ‘A’ direction considered parallel to the relative velocity and a ‘B’ direction perpendicular to the relative velocity and parallel to the y-direction are formed, giving:

$$\hat{B} = \begin{bmatrix} -\hat{A}_x \frac{\hat{A}_y}{\hat{B}_y} & -\sqrt{\hat{A}_x^2 + \hat{A}_z^2} & -\hat{A}_z \frac{\hat{A}_y}{\hat{B}_y} \end{bmatrix}^T \quad [3.79]$$

where \hat{A} and \hat{B} are the unit vectors in directions A and B.

From this arbitrary coordinate system the perpendicular ‘B’ direction is rotated by the random roll angle ϕ [°] (equation [3.57]) which is facilitated by rotation matrix C which rotates ϕ radians about axis \hat{A} :

$$\hat{B}' = C \times \hat{B}$$

$$C = \begin{bmatrix} (1 - \cos \phi) \hat{A}_x^2 & (1 - \cos \phi) \hat{A}_x \hat{A}_y & (1 - \cos \phi) \hat{A}_x \hat{A}_z \\ (1 - \cos \phi) \hat{A}_x \hat{A}_y & (1 - \cos \phi) \hat{A}_y^2 & (1 - \cos \phi) \hat{A}_y \hat{A}_z \\ (1 - \cos \phi) \hat{A}_x \hat{A}_z & (1 - \cos \phi) \hat{A}_y \hat{A}_z & (1 - \cos \phi) \hat{A}_z^2 \end{bmatrix} + \begin{bmatrix} \cos \phi & \hat{A}_z \sin \phi & -\hat{A}_y \sin \phi \\ -\hat{A}_z \sin \phi & \cos \phi & \hat{A}_x \sin \phi \\ \hat{A}_y \sin \phi & -\hat{A}_x \sin \phi & \cos \phi \end{bmatrix} \quad [3.80]$$

note the prime, ', denoting the rotated unit vector.

At length the resultant relative velocity in global coordinates, \vec{U} [ms⁻¹], is found:

$$\vec{U} = u_A \hat{A} + u_B \hat{B}' + u_{t_j} \hat{A} \times \hat{B}' \quad [3.81]$$

where u_A and u_B [ms⁻¹] are evidently the normal velocity magnitude and primary tangential velocity magnitude (equations [3.77] and [3.78]), respectively, \hat{A} , is the unit vector parallel to the relative velocity in global coordinates, \hat{B}' , is the unit vector

perpendicular to the relative velocity at a randomly determined orientation. The final term represents the scalar product of the magnitude of secondary tangential velocity, u_{ij} [ms^{-1}], and a unit vector that forms a right-handed triad with the previously defined unit vectors, $\hat{\mathbf{A}} \times \hat{\mathbf{B}}'$.

The new velocity of the collision subject is determined by the momentum exchange of the two particles, equations [3.61]-[3.66], being resolved back into global coordinates from the revolved and relative coordinate system of the collision by equation [3.81], the momentum change upon the collision object, when dispersed through the entire local concentration, is taken as negligible.

3.2.7 Wall Collisions

Wall collisions may be handled as a simplified case of inter-particle collisions. They are deterministic as they are known to occur due to a particle reaching the wall face so no probability of collision is involved, and no representative collision object is required as the wall is struck. The properties recorded at this point are the relative velocity, \vec{U} [ms^{-1}], (simply particle velocity for stationary walls) and the local wall normal, $\hat{\mathbf{N}}$. The projection of the relative velocity on the wall normal gives the proportion of relative velocity in the normal direction:

$$u_n = \vec{U} \cdot \hat{\mathbf{N}} \quad [3.82]$$

The components of tangential velocity are found by subtracting the normal velocity:

$$\vec{u}_t = \vec{U} - u_n \hat{\mathbf{N}} \quad [3.83]$$

From this the tangential unit vector, $\hat{\mathbf{T}}$, is determined:

$$\hat{\mathbf{T}} = \frac{\vec{u}_t}{|\vec{u}_t|} \quad [3.84]$$

this is to be used in the coordinate resolution. The magnitude of the tangential velocity vector is taken to be the pre-collision tangential velocity and the methodology of section

3.2.6 is followed from equation [3.61], however the coefficients of restitution, e , and dynamic friction, μ_d , are randomised as below to model wall roughness:

$$\theta = \tan^{-1}\left(\frac{u_n}{u_t}\right) \quad [3.85]$$

$$e = \max(0.7, 1 - 0.0136\theta) \quad [3.86]$$

$$\mu_d = \max(0.15, 0.5 - 0.0175\theta) \quad [3.87]$$

Rotation of the collision object is zero and the relative mass of the particle to the wall is assumed to be zero, $M = 0$. The coefficient of static friction, μ_s , is assumed to be equal to the maximum possible dynamic value, 0.5. These values are taken from Sommerfeld (2001) for glass particles and steel walls as it is difficult to find more relevant data.

When the post collision normal and tangential velocities are found they are resolved to global coordinates as below (assuming a stationary wall):

$$\vec{u}_p = u_n \hat{N} + u_t \hat{T} \quad [3.88]$$

3.3 Combustion of a Single Fuel Particle

The numerical process of solid particle combustion, pertaining to coal and biomass, has been previously described in section 2.3. In this section the mathematical handling of the sequential behaviours of a particle during combustion are introduced as implemented in Fluent (ANSYS, 2009a). These behaviour models set the particle continuity and energy conservation equations. The typical discretisation scheme, to integrate the particle conservation equations, is analytical assuming constant mass and temperature over a timestep. By default Fluent does not take into account the moisture of the particles, but its effect has been enabled in the description below.

Taking the numbered laws, as used by Fluent, in parentheses, and recalling the combustion sequence from section 2.3 gives: inert heating {1a}, evaporation {2&3}, inert heating {1b}, devolatilisation {4}, volatile combustion, char combustion (surface combustion {5}) and inert heating {6}. Due to the historical development of these

models Fluent in fact handles the evaporation by injecting water droplets and removing moisture mass from the parent particle. In this way the moisture content of the solid particle is removed and attributed to a coincident droplet particle. The momentum calculations use the total mass of the solid and droplet particles, but whilst the coincident droplet exists the solid particle experiences no heat or mass transfer and the coupled mass is used in heat transfer equations for the droplet. Volatile combustion takes place within the fluid phase and as such there is no special particle model. Gaseous reactions are described in section 3.1.3. Both forms of inert heating Laws {1&6} are identical, but the selection conditions differ. Law {1} occurs below a 'vapour temperature' and {6} occurs after the fixed carbon (FC) content of the particle is reduced to zero (ash particle remains). Vapour temperature refers to the moisture in {1a}, meaning vaporisation temperature of the droplet particle, and volatiles in {1b}, meaning devolatilisation temperature of the solid particle.

Under mass transfer conditions the particle density decreases to reflect the reduction in particle mass as particle diameter is unchanged. This is simply provided by the relationship below, which automatically accounts for changes in particle diameter due to swelling as well:

$$\rho_p = \frac{6m_p}{\pi d_p^3} \quad [3.89]$$

Sections 3.3.1-3.3.6 describe the individual behaviour models. They have a common format where the behaviour and conditions for commencement and suspension of the model are presented followed by the mathematical mass transfer and heat transfer equations, included a sentence explaining the meaning and definition of new terms. A definition is only given once for each parameter, although many terms are common to multiple equations within these sections.

3.3.1 Inert Heating {1a}{1b}{6}

The same heat transfer equation is used in the different inert heating laws, their numbering represents the various instances, in which manners the particle behaves. For droplet particles {1a} inert heating takes place if the particle temperature is below the vaporisation temperature. Above this, Law 2, evaporation, is enforced. When a wet solid particle is being modelled the combined mass of the dry solid particle and a coincident droplet representing the moisture fraction is used in the inert heating heat transfer equation. Similarly, for solid particles {1b} inert heating takes place if the particle temperature is below the volatile vaporisation temperature, above this Law 4, devolatilisation, is enforced. As mentioned in the introduction to section 3.3, laws {1a&b} are respectively on different particle types and {6} is enforced after char combustion is complete.

Mass transfer

Constant mass

Heat transfer

$$m_p c_p \frac{dT_p}{dt} = h A_s (T_\infty - T_p) + \varepsilon_p A_s \sigma (\theta_R^4 - T_p^4) \quad [3.90]$$

states the heating power is equal to the rate of heat due to convection plus the rate of heat due to radiation. Particle mass, m_p [kg], specific heat capacity, c_p [$\text{Jkg}^{-1}\text{K}^{-1}$], particle temperature, T_p [K], convective heat transfer coefficient, h [$\text{Wm}^{-2}\text{K}^{-1}$], particle surface area, A_s [m^2], local temperature of carrier fluid, T_∞ [K], particle emissivity, ε_p [-], Stefan-Boltzmann constant, σ ($5.67 \times 10^{-8} \text{ Wm}^{-2}\text{K}^{-4}$), radiation temperature, θ_R [K]. The radiation temperature is calculated from the incident radiation at the particle.

3.3.2 Evaporation {2}

The evaporation can only be applied to droplet particles. For solid particles with a moisture component the combined mass of the parent particle and droplet is used in the heat transfer equation [3.92]. Evaporation begins when the particle temperature rises to the vaporisation temperature and continues so long as the particle temperature is (a) below the boiling point and (b) the particle mass is greater than the initial particle mass multiplied by, unity minus the initial moisture content (dry condition). If the boiling point is reached, Law 3, boiling, is enforced, if the dry condition is reached the droplet particle is extinguished (evaporated) so the parent solid particle switches to Law 1b, inert heating.

Mass transfer

$$N_i = k_c (C_{i,s} - C_{i,\infty}) \quad [3.91]$$

states that the volumetric mass release of vapour, is equal to the vapour potential between the particle surface and the carrier fluid. Molar flux of vapour, N_i [$\text{mol.m}^{-2}\text{s}^{-1}$], specific mass transfer coefficient, k_c [ms^{-1}], vapour concentration at particle surface, $C_{i,s}$ [mol.m^{-3}], vapour concentration in fluid cell, $C_{i,\infty}$ [mol.m^{-3}].

Heat transfer

$$m_p c_p \frac{dT_p}{dt} = h A_s (T_\infty - T_p) + \varepsilon_p A_s \sigma (\theta_R^4 - T_p^4) + \frac{dm_p}{dt} h_{fg} \quad [3.92]$$

where all terms are as in the description given for inert heating, equation [3.90], with an additional term for the latent heat of the mass loss due to evaporation. Latent heat of evaporation for the droplet material, h_{fg} [Jkg^{-1}].

3.3.3 Boiling {3}

Boiling is initiated if the droplet particle temperature rises to the boiling point and continues until the droplet particle mass is depleted (meaning the droplet has evaporated). Once the droplet is extinguished the solid parent particle begins Law 1b, inert heating.

Mass transfer

$$-\frac{dm_p}{dt} h_{fg} = hA_s(T_\infty - T_p) + \varepsilon_p A_s \sigma (\theta_R^4 - T_p^4) \quad [3.93]$$

states that the rate of energy absorption (rate of mass loss multiplied by latent heat value of that mass), is equal to convective heat transfer, plus radiative heat transfer.

Heat transfer

Constant Temperature. Heat transfer to the particle directly balances the latent heat of the liberated mass. Equation [3.93] is identical to equation [3.92] under this condition.

3.3.4 Devolatilisation {4}

Devolatilisation is initiated by the particle temperature rising to the devolatilisation temperature and continues until the particle mass is reduced below the initial particle mass multiplied by, unity minus the sum of initial moisture content and initial volatile content (char condition).

There are several options in Fluent for the devolatilisation model. Following the expertise of Williams *et al.* (2002) and Ma *et al.* (2009), the Single Rate (Arrhenius) method has been followed in this thesis.

Mass transfer

$$-\frac{dm_p}{dt} = k_1 (m_p - (1 - f_{V0})(1 - f_{M0})m_{p0}) \quad [3.94]$$

states that the rate of mass loss, is equal to the devolatilisation rate multiplied by the fraction of volatiles remaining. Devolatilisation rate, k_1 [s^{-1}], initial mass fraction of volatile matter, f_{V0} [-], initial mass fraction of moisture, f_{M0} [-], initial particle mass, m_{p0} [kg].

Where the devolatilisation rate has the form:

$$k_1 = A_1 e^{-\frac{E_1}{RT}} \quad [3.95]$$

where the values of the pre-exponential constant, A_1 [s^{-1}], and activation energy, E_1 [$J \cdot mol^{-1}$], are determined empirically for each fuel.

Heat transfer is identical to that under evaporation, equation [3.92].

Some bituminous coals have a high propensity for swelling during devolatilisation. The devolatilisation swelling model was developed especially for these, it is given here:

$$\frac{d_p}{d_{pV0}} = 1 + (C_{sv} - 1) \frac{(1 - f_{M0})m_{p0} - m_p}{f_{V0}(1 - f_{M0})m_{p0}} \quad [3.96]$$

this is essentially a linear relationship between particle diameter rate of change and mass rate of change. The ratio of particle diameter to initial particle diameter during devolatilisation is varied linearly from unity to the swelling coefficient as the volatile fraction approaches zero. Particle diameter at the start of devolatilisation, d_{pV0} [m], devolatilisation swelling coefficient, C_{sv} . The final term of equation [3.93] is the ratio of volatile mass to initial volatile mass (the numerator is the difference between the initial particle mass excluding moisture mass and the current particle mass, which is equivalent to the mass of volatiles released).

3.3.5 Volatile Combustion

The combustion of volatiles is not tracked in the Lagrangian frame. Due to computational accounting, the mass of volatiles is attributed to the Eulerian cell, in which the particle presently resides, and subtracted from the Lagrangian particle during devolatilisation. Therefore it is not meaningful to state a mass or heat transfer equation during volatile combustion as this is concurrent with the separate particle behaviour, that follows one of the particle combustion laws. The mathematics of volatile combustion is presented in section 3.1.3, gaseous reactions.

3.3.6 Char Combustion {5}

Ignition of the char begins immediately after devolatilisation has halted, due to the expulsion of all volatile matter, and continues until the particle mass drops below the initial particle mass multiplied by the initial ash content (ash condition), at which point Law 6, inert heating, is enforced on the ash particle. The reaction may be written generically, and in the case of pure carbon_(s) char first step oxidation, as follows:



The rate of the combustion of the char is limited by oxidant diffusion to the particle surface (physical rate), D_0 [m^{-1}s], as well as the char reactivity (chemical rate), \mathfrak{R} [m^{-1}s]. These rates are given with the equivalent units of [$\text{kgm}^{-2}\text{s}^{-1}\text{Pa}^{-1}$] by Baum and Street (1971). Some models assume that the surface reactivity will be much greater than the bulk diffusion, however the common method for coal chars uses Smith's (1982) Intrinsic Model:

Mass transfer

$$-\frac{dm_p}{dt} = A_s \frac{\rho_f RT_\infty Y_{\text{ox}}}{M_{\text{ox}}} \frac{D_0 \mathfrak{R}}{D_0 + \mathfrak{R}} \quad [3.98]$$

where the terms represent the species mass fraction of oxidant, Y_{ox} , and molar mass of oxidant, M_{ox} [$\text{kg}\cdot\text{mol}^{-1}$]. The controlling rates are combined in parallel addition as represented by the final term on the RHS (Baum and Street, 1971).

$$D_0 = \frac{C_1}{d_p} \left(\frac{T_p + T_\infty}{2} \right)^{0.75} \quad [3.99]$$

where the diffusion coefficient, C_1 [$\text{sK}^{-0.75}$] is found assuming binary $\text{O}_2\text{-N}_2$ diffusion at the reference temperature and pressure (Baum and Street, 1971).

$$\mathfrak{R} = \eta \frac{d_p}{6} \rho_p A_g A_i e^{-\frac{E_i}{RT_p}} \quad [3.100]$$

where the terms represent the effective reaction rate, η , specific internal surface area, A_g [m^2kg^{-1}], intrinsic pre-exponential term, A_i [m^{-1}s], and intrinsic activation energy,

E_i [$\text{J}\cdot\text{mol}^{-1}$]. The effective reaction rate describes the proportional reaction rate relative to the maximum that would exist without any resistance to pore diffusion. There are further equations presented in the Fluent Theory Guide (ANSYS, 2009a) that describe how this value is obtained based on the propensity for the oxidant to diffuse to the active sites within the particle pores. The original method is given by Smith (1982).

Heat transfer

$$m_p c_p \frac{dT_p}{dt} = hA_p (T_\infty - T_p) + \varepsilon_p A_p \sigma (\theta_R^4 - T_p^4) - f_h \frac{dm_p}{dt} H_{\text{reac}} \quad [3.101]$$

this is equivalent to the heat transfer during evaporation, equation [3.92], however the total heat (including latent) from the mass reacted is positive. The final term on the RHS represents this with the fraction of heat, f_h , and heat of reaction, H_{reac} [Jkg^{-1}] – this is the specific heat of converting the solid char into gaseous products. f_h is unity for coal char oxidising to CO, the term is included in equation [3.101] so that, if a single step char oxidation reaction, with the product CO_2 , were considered, a smaller fraction of the heat of reaction would be included in the particle heat transfer and the remainder included in the cell energy equation instead.

Chapter 4

Biomass Fuel Particle Aerodynamics in a Pipeline

4.1 Introduction

An important but often neglected area of pulverised biomass combustion modelling for power generation is the pre-burner transportation of biomass. A uniform distribution of particles at the entry to the burner (inlet of numerical domain) is often assumed, however flame instability may be induced by asymmetry in the particle distribution. In the present study, a combination of computational modelling and online particle flow measurement techniques have been employed to investigate the gas-biomass particulate flow in a pipeline. The main objectives of this chapter are twofold. Firstly, to validate the computational fluid dynamics (CFD) models with the novel online particulate flow measurements for their applicability and accuracy, and secondly to obtain a quantitative characterisation and detailed insight of the flow in the pipeline investigated. The investigation has been performed in a relatively small scale pipeline system to enable reliable experimental measurement in a well controlled laboratory environment. The Reynolds number range is still useful for industrial applications. All experimental data, presented in this chapter has been obtained and provided by Mr Xianchen Qian and Prof Yong Yan at the University of Kent using a novel measurement technique consisting of a series of annular and arc-shaped electrostatic sensors. The experimental velocities and spatial distributions from their work are reproduced here for convenience since the accepted paper, Gubba *et al.* (2012a), is not yet published. The collaborative work is undertaken as part of the EPSRC UK-China research programme ‘Optimisation of biomass/coal co-firing processes through integrated monitoring and computational modelling’.

Biomass is considered a renewable source of energy and CO₂ neutral, leading to a significant effort being applied to many successful co-firing demonstrations throughout the world over the last decade or so. However, due to incomplete knowledge of the physical and chemical properties and operating conditions of burners and boilers



(a) Willow



(b) Wood



(c) Bark

Figure 4.1 Biomass images.

Typical images of various biomass samples used in the present chapter are presented on the left-hand-side of each image. The corresponding microscopic images are shown on the right-hand-side for (a) willow chips, (b) wood, and (c) bark.

these demonstrations have been restricted to a limited menu of categories of biomass (McKendry, 2002, Robinson *et al.*, 2003, Baxter, 2005, Hansson *et al.*, 2009). The prolific and substantial demonstrations of coal combustion modelling provide an appealing platform for other solid fuel simulations, however, distinctive mechanical and chemical characteristics of biomass fuels must be borne in mind during the adaptation of these models to biomass applications. The chemical properties of these biomass dominate during the reaction phase in the furnace (Vassilev *et al.*, 2010), but the physical properties, such as particle size and shape, of a given biomass have great impact upon aerodynamics and these evolve from the pre-treatment and milling or pulverising process used in a particular power station. Most biomass particles in use, such as wood and straw, tend to be larger and more irregular than coal dust, due to the difficulty in milling, as well as fibrous in shape. Consequently, the site specific fuel processing and feeding hardware, all extraneous to a typical numerical domain, influence the coal-biomass mixture and this in turn influences the pneumatic transportation of particles to the burner. As has been discussed in section 1.3 the chemical properties of biomass are very variable in nature, whereas the physical properties are mainly dependent on the milling equipment and rate for a given sample of biomass. Figure 4.1 shows photographs and the microscopic images of typical biomass samples considered in this chapter. It is interesting to note that these particles are topologically in contrast to the sizes and shapes of those typical in pulverised coal power applications (Williams *et al.*, 2000b).

In the case of co-firing, biomass can be introduced at various stages with relatively high fuel mass loadings, between 25 to 40% at about 20 to 40ms⁻¹ of conveying velocity in typical industrial power stations (Wang *et al.*, 2011). Frequently the biomass is blended after milling and shares the same infrastructure as the coal. On the other hand, biomass may be injected through dedicated burners using separate infrastructure (Wang *et al.*, 2011). Conveying biomass to the burners in both ways can produce undesirable phenomena, such as roping, trapping, deposition, clogging, etc. due to their high moisture content. Above all, the fuel mass distribution at the burner implies a significant impact on the burner conditions and the subsequent complex flow and combustion

processes in the furnace. Therefore the physical behaviour of the particulate biomass must be understood correctly.

The measurement of the dispersed gas-solid transportation flow parameters is a challenging research area (Yan, 2001). In the past, the absence of reliable particle velocity metering and on-line particle sizing equipment have made it difficult to study dispersed gas-solid phase flow. Recent advances in the development of various on-line sensing techniques, such as electrostatic (Shao *et al.*, 2007, and Shao *et al.*, 2010) and digital imaging (Carter *et al.*, 2005), have, to some extent, enabled the acquisition of experimental data on an industrial scale combustion test facilities. Despite the above mentioned advancements in monitoring systems, the knowledge gained is limited and only restricted to 100% pulverised coal flows.

Numerical simulations of particle-laden flows in reacting and non-reacting cases have been performed by many researchers in the past (Maxey and Patel, 2001, Apte *et al.*, 2003, Ferrante and Elghobashi, 2003, Kurose and Makino, 2003, Lu *et al.*, 2009, and Pozorski and Apte, 2009). However, the majority of these studies were investigated by assuming an homogeneous shape (in general spherical) with equivalent volume sphere diameters (d_{EVS}) of less than 200 μm . Abundant proportions of milled biomass fuel particles in the fuel pipeline exceed a millimetre in their shortest dimension. In addition, the prevailing focus of some studies is in understanding combustion dynamics in the near burner region (Kurose and Makino 2003). Recently, Chinnayya *et al.* (2009) have successfully modelled high Reynolds number (86,000) particulate transportation using Large Eddy Simulations (LES) in a semi-industrial pulverised power plant pipe. This study was limited to a typical power plant pulverised coal, having particles which are less than about 300 μm , of spherical diameter, and travelling within a short pipe length (0.396m).

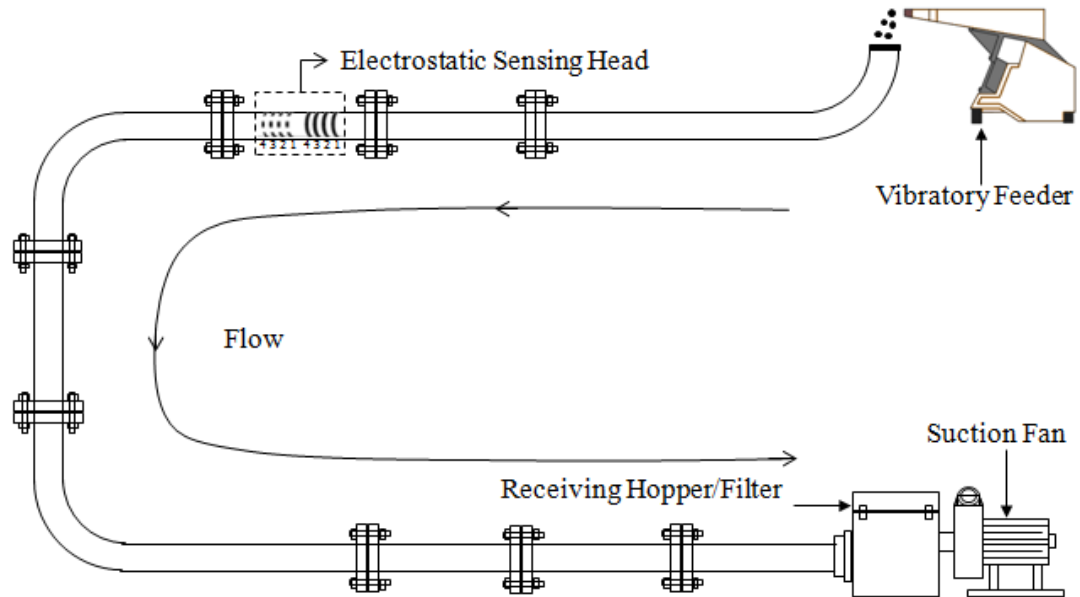


Figure 4.2 A schematic diagram of the gas-solid flow measurement system at the University of Kent.

4.2 Experimental Measurement System

All tests were undertaken on the test rig in the Instrumentation Laboratory at the University of Kent, as shown in Figure 4.2. An industrial vacuum system is connected to the lower right hand side of the stainless steel pipeline to generate a stable air flow and a vibratory feeder at the top right hand side of the rig is used to feed the particles into the rig. Both the suction power of the vacuum system and the feeding rate of the vibratory feeder can be adjusted. The conveying air velocity was measured using a digital hot-wire anemometer with $\pm 2\%$ standard error. In order to control the air velocity precisely, the loading tank of the industrial vacuum cleaner was cleaned after every six tests of approximately 2 minutes each and the suction power of the vacuum cleaner was adjusted after each test according to the measured air velocity. In this way various particle flow conditions, such as different conveying air velocity and mass flow rate, could be created.

The movement of particulate materials in a pneumatic pipeline generates a net electrostatic charge on the particles through their interactions with each other, the conveying air and the pipe itself (Yan *et al.*, 1995). Two banks of electrostatic sensors,

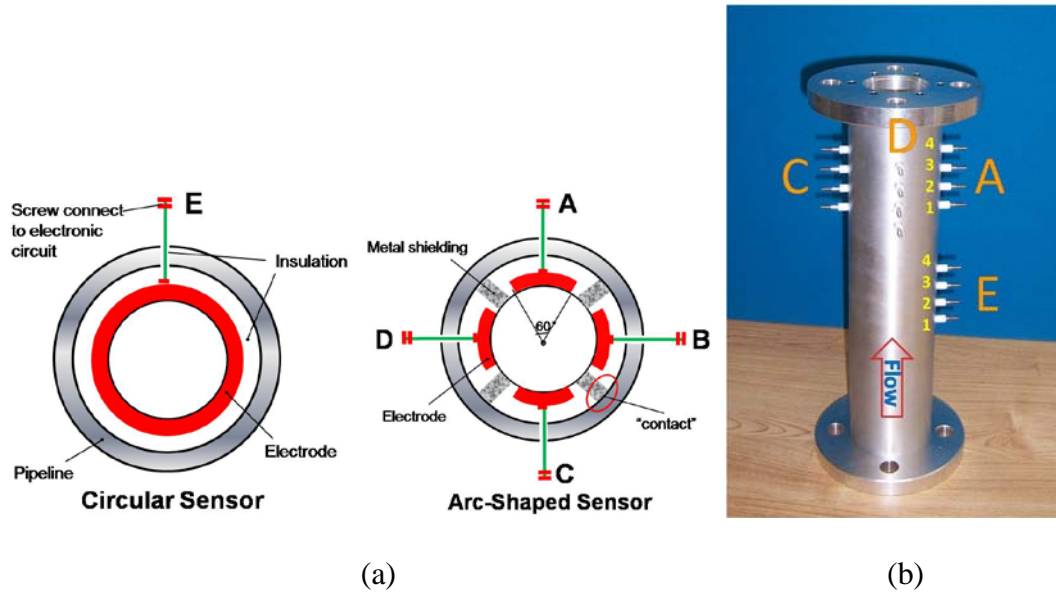


Figure 4.3 Structure of the Multi-Channel Electrostatic Sensors.

(a) Cross-section of the electrostatic sensors with the circular sensors in group E to the left and arc shaped sensors in groups A-D, and (b) The layout of the electrostatic sensors within the spool piece showing the direction of the air flow.

the one with annular shape and the other in the form of four arcs about the same centre, were used in the experiment. Figure 4.3 shows the structure of the multi-channel electrostatic sensors. Each bank contains four sensors with a fixed lateral displacement between them, in this way correlation of the signals from each annular sensor could determine the time at which a highly charged particle was detected by each and the velocity inferred. There are six combinations to forming a correlated pair from the four signals. In a similar manner, the lateral location of the particle, to within a quarter circle, is also inferred from the strength of the signal from each arc in the other bank of sensors. The structures of the sensing heads in the two different types of sensor, including the electrodes, insulation material and connection terminals, are shown in Figure 4.3(a). These are incorporated into a spool piece, which houses the total of five sets of electrodes and each of them is composed of four identical non-intrusive electrodes, Figure 4.3(b). The annular electrodes (Group E) are mounted flush to the inner pipe wall to measure the mean velocity and the overall root mean square (RMS) charge levels of the solid particles. Qian *et al.* (2011) indicate four groups of arc-shaped electrodes that are evenly distributed around the pipe wall (Group A on the highest edge

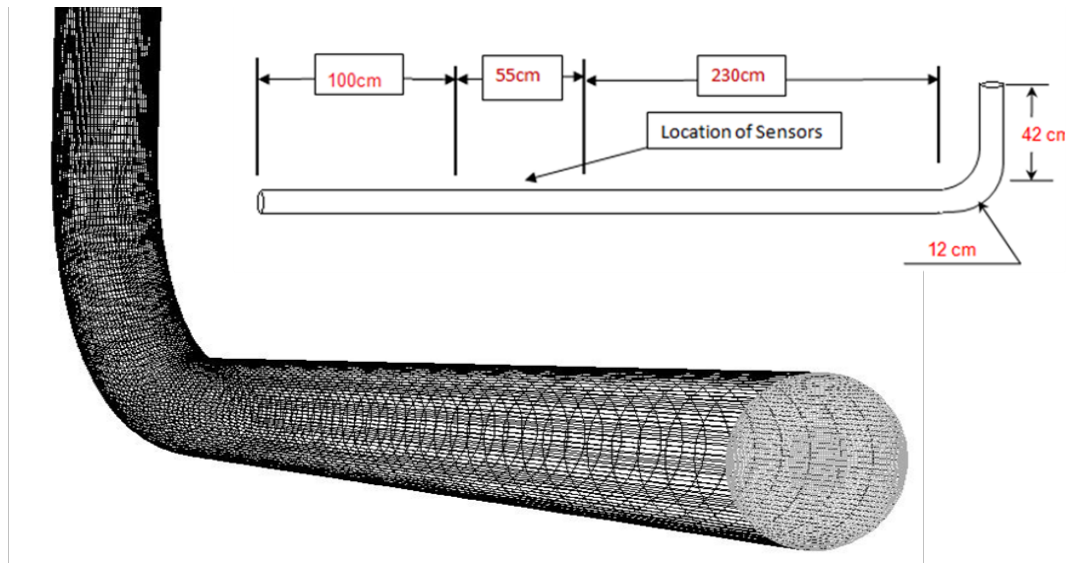


Figure 4.4 Schematic of numerical domain and example of the mesh.

of the pipe, Groups B and D in the middle and Group C at the bottom) to measure the localised parameters of the particles.

4.3 Numerical Modelling

The computational domain considered in the CFD modelling mimics the experimental setup, shown in Figure 4.2, but truncated to the elbow and sensor locations. The region to be simulated consists of a pipe of 49mm diameter with length, after the elbow, of 3.85m. A schematic diagram of the computational domain employed, including the full dimensions and an image of the mesh are presented in Figure 4.4. As seen in Figure 4.2, the return bend in the pipe, which is after the measuring location, is redundant and therefore it is not considered in the CFD modelling. However, the pipe has been extended to 1m in length past the measuring location in order to isolate the pressure-outlet boundary condition from influence upon the test section. Five different meshes, ranging in size from 72k to 1.1M cells, are used for grid sensitivity studies. For brevity, suffice it that this has been performed in a similar manner to the description of grid independency to be given in section 6.3. The grid density is much greater in the radial and angular directions compared to the axial, in which direction lower velocity gradients are expected. Higher grid densities in the radial and angular directions will

assist in resolving the boundary layer flow and hence, the particulate flow can be simulated more accurately.

The continuous phase CFD modelling approach has been carried out using Reynolds-averaged Navier Stokes (RANS) methodology using ANSYS Fluent v. 12.0. Due to the high Reynolds number in the test cases chosen (53550 to 83860), the standard $k-\omega$ model for the turbulence is found to perform better than the standard $k-\epsilon$ model (ANSYS, 2009c). Second-order upwind discretisation schemes are used, with the SIMPLE pressure-velocity coupling.

The particulate phase has been modelled using the discrete phase model (DPM) in Fluent. The DPM method uses a Lagrangian approach to calculate the position and trajectories of individual particles. In RANS no turbulent structure is simulated in the fluid phase, its averaged effects are modelled through the transportation of the eddy viscosity and turbulent properties. Therefore the dispersion of particles due to turbulence must also be modelled. This has been performed by application of the discrete random walk (DRW) model (section 2.1.2). The drag, as a function of the relative velocity, is already handled within the DPM. However, due to the eddy viscosity method (EVM), the fluid velocity available to the particles is the steady averaged value. Therefore the DRW model adds an additional force upon the particle to represent the additional drag, due to the instantaneous component of the fluid velocity, that the particle would experience in turbulent flow. Separate randomly generated directional components to the instantaneous velocity are employed predicted from the isotropic turbulent energy, k , within the cell. In addition the DRW model allows all injected streams of particles to be split into N ‘tries’. These are identical streams with an N^{th} of the prescribed original flow rate injected at the same point. Since a different standard trajectory calculation as well as dispersion calculation is performed for each ‘try’ a more refined simulation of the particles is facilitated. In this investigation the number of ‘tries’ was taken to be 10. The value has been found to be sufficient for a statistically accurate particle trajectory to be determined.

In-house user-defined functions (UDFs) are developed to account for inter-particle interactions and the irregular shape of biomass fuels. Their implementation is discussed in sections 4.3.1-2 and full mathematical description given in section 3.2. It is important

to mention here, as biomass particles are of different shapes and sizes, their aerodynamic behaviour may severely influence the entire gas phase. Based on the samples of the biomass particles investigated, their estimated shape factors are calculated for a representative population of particle-classes by a UDF (DEFINE_DPM_INJECTION_INIT). The number of injections required (30-70, based on the particle distribution) are initialised at the inlet surface in the CFD simulations. The ratio of the particle density to the gas density is about 400 and the average volume fraction of the particles is less than 10% in all cases. Local particle concentrations may well exceed this value, and in such regions inter-particle collisions may become significant. In order to account for inter-particle collisions, a theory developed by Laín and Sommerfeld (2008), described in section 3.2.6, has been employed using UDFs. The pipe wall and particles are assumed to be smooth and wall collisions are assumed to be perfectly elastic. This appears to be a reasonable assumption, bearing in mind that no information about the true values of the coefficients of restitution and friction are available for the materials.

4.3.1 Non-Spherical Drag

Various shapes and sizes of the biomass particles considered in this investigation can be seen in Figure 4.1. It can be appreciated that these shapes are highly non-spherical and suggests that using spherical drag models to account for the particle drag may be inaccurate and pose problems to the gas and particulate phase. Hence, detailed information on the shape, volume, density, surface area and drag coefficient are required to improve the understanding of the transport phenomena of these irregularly shaped particles. As an initial and valid approximation, a fixed orientation non-spherical drag model, based on an estimated particle shape factor, has been used in this investigation (Haider and Levenspiel, 1989, Ma *et al.*, 2009). Haider and Levenspiel's (1989) non-spherical drag law is a well established method using the widely known sphericity as the shape factor. However, as discussed in section 2.2.1, the surface area of a real non-spherical particle is, in general, unknown as the methods to measure the parameter are non-trivial. The solution employed in this investigation is to assume a non-spherical mathematical shape for the particle, whose surface area can be calculated

from more easily measured parameters (lengths and widths). Hence, in the present study, a cylindrical shape is assumed.

A representative selection of particles from each sieve-sized class is scanned optically, in an identical manner to the method for measuring the Corey shape factor (CSF) described in section 2.2.1. Imaging software automatically identifies particles against the high contrast background and then measures the greatest apparent dimension and the greatest width perpendicular to this. These two dimensions are taken as the length and diameter of the cylinder, respectively. It is assumed that slight excitation of the field of particles will reduce a statistically significant proportion of the particles to their lowest gravimetric potential and therefore the greatest dimensions will be observed by the 2D scan. The numerical population of particles consists of different groups of identical particles. The sphericity of the particle is assigned at initialisation along with its nominal diameter, that of its equivalent volume sphere (EVS), velocity, point of injection and mass flow rate as introduced in section 4.3. The sphericity and nominal diameter are required for execution of the Haider and Levenspiel drag method. This is presented in section 3.2.3. Where equation [3.25] defines the sphericity, Φ , and equation [3.26] is the drag coefficient, C_D .

4.3.2 Inter Particle Collisions

As with asphericity, the modelling of inter-particle behaviour presents multiple choices based on the degree of complexity applied to approximate the real process. It is common in particle transport problems that the ‘dilute discrete phase’ assumption is applied to justify the effects of inter-particle processes as being rare enough to be neglected. However, it is important to note that despite a dilute global particle concentration, the local particle concentration, such as near to the bend and the bottom of the pipeline transporting the large particles, may be greatly condensed and the probability of collisions increased. Due to interrelated physical processes, the significance of such inter-particle collisions cannot necessarily be taken as negligible. For example, alterations to the pattern of wall collisions due to inter-particle collisions have been observed by Lin and Liu (1997) and identified as an important mechanism for particle suspension. With respect to the above, it is also worth mentioning that the

dilute loading regime present in this investigation is well under the limit used by Lin and Liu (1997).

A 2D stochastic inter-particle collision method (Laín and Sommerfeld, 2008), applicable to a dilute monodisperse particle phase, is modified to model size variations within the particle phase in 3D and used in this investigation, after extension the model can handle size-disperse particles but assumes spherical shape and a constant particle density. The mathematical basis of the 3D collision prediction and resolution has been described in section 3.2.6. The extension to size variation is described later in this section. Equation [3.53] handles collision probability and the post collision translational velocities are presented in equations [3.61]-[3.63]. Angular momentum is conserved in this method and therefore equations [3.64]-[3.66] are not implemented. For simplicity, a single “representative local particle” class is considered by treating all “local particles” as identical within a cell. This is similar to monodisperse flows, but diverges as the size of the “local particle” may change from cell to cell, as well as differ from the tracked particle, along with the particle concentration and velocities. Under monodisperse conditions all particles are identical and so are equal in size, and the only distribution is in velocity and concentration.

In order to reduce the computational expense of particle tracking, individual particle trajectories that are calculated represent multiple actual particles. In steady particle tracking, the particle trajectory is a stream of particles flowing at a constant mass flow rate. These streams are tracked sequentially, however the particle streams are oblivious to other streams in a Lagrangian frame. The only communication between separate particle streams is indirectly through their interaction with the fluid phase. To facilitate inter-particle interactions, properties of the Lagrangian particle stream must instead be stored in the Eulerian cell. In this investigation storage for a single class of local particle is employed so that the concentration, mass-weighted mean diameter and velocity components are obtained using information from all particle streams that pass through the cell plus the assumption of constant density and spherical shape. In this way a “local particle” is spawned to exist in each fluid cell. If a fluid cell is unvisited by any particles then no properties are calculated (remain zero) and no collisions will be predicted. Exploiting the constant flow rate, the mass of particles within the cell from a

particular stream, termed its static mass, is directly proportional to the period of time a stream takes to traverse the cell, termed its dwell. Also the displacement between the points of entry and exit of that stream to and from the cell and the dwell give the stream velocity through the cell:

$$p_{\text{cell},k} = \sum_i \frac{\dot{m}_i}{m_{pi}} D_{i,k} \quad [4.1]$$

$$m_{\text{mass},k} = \sum_i \dot{m}_i D_{i,k} \quad [4.2]$$

$$\vec{u}_{\text{mass},k} = \sum_i \dot{m}_i \vec{s}_{i,k} \quad [4.3]$$

where the subscripts $_i$ and $_k$, denote, respectively, particle stream i and cell k . If k is omitted on the right hand side (RHS), the property is constant for stream i . p_{cell} , is the population of particles in the cell, \dot{m} [$\text{kg}\cdot\text{s}^{-1}$], is the mass flow rate of the particle stream, m_p [kg], is the mass of an individual particle, D [s], is the dwell of the particle stream, m_{mass} [kg], is the static mass of particles in the cell, \vec{u}_{mass} [$\text{kg}\cdot\text{m}\cdot\text{s}^{-1}$], is the sum-product of mass and velocity and, \vec{s} [m], is the displacement of the particle stream within the cell. Physically equation [4.1] states that the cell population is equal to the sum of each stream's mass flow rate over the mass of an individual particle in the stream multiplied by the dwell of that stream in the cell. Equation [4.2] expresses that the mass of particles in a cell is equal to the sum of each stream's product of mass flow rate and dwell. Equation [4.3] states that the velocity-mass of particles in a cell is equal to the sum of each stream's product of mass flow rate and displacement through the cell. As a particle leaves a cell, the accumulative variables are updated in the vacated cell with the effect of summing over all streams (more correctly all passes of streams, in the case of a particle stream traversing a cell multiple times), the mathematical result is equivalent to equations [4.1]-[4.3], the numerical method overwrites the previous value with the sum of the previous value and the latest contribution.

In terms of the operation within Fluent the implementation of the inter-particle collision model is split between UDF templates. Assessment of the collision probability during a timestep, and the subsequent velocity alteration as a consequence, is performed during `DEFINE_DPM_SCALAR_UPDATE`. This macro is called once per timestep,

whereas the DEFINE_DPM_DRAG define macro may be called multiple times within a timestep for trajectory accuracy control, after all one of the default DPM discretisation schemes is the two-step trapezoidal, and the DEFINE_DPM_BODY_FORCE macro is called for each dimension of the problem in every drag assessment. Identification of entrance to a new cell, by the particle, is best performed in the DEFINE_DPM_DRAG. This is to ensure the correct particle location, at the entrance to a new cell, is recorded when calculating the cell displacement, $\vec{s}_{i,k}$ [m], as used in equation [4.3]. If the condition of a new cell were assessed within the SCALAR_UPDATE macro then particle displacement due to the drag and body forces for that timestep would already have occurred. If a new cell is detected then an additional stream is added to equations [4.1]-[4.3] where cell k is the cell vacated by the currently tracked particle i . A manually called EXECUTE_ON_DEMAND macro is required to perform the final averaging step:

$$c_{p,k} = \frac{P_{\text{cell},k}}{V_{\text{cell},k}} \quad [4.4]$$

$$d_{p0,k} = \sqrt[3]{\frac{6}{\pi} \frac{m_{\text{mass},k}}{\rho_p P_{\text{cell},k}}} \quad [4.5]$$

$$\vec{u}_{p0,k} = \frac{\vec{u}_{\text{mass},k}}{m_{\text{mass},k}} \quad [4.6]$$

where c_p [m^{-3}], is the concentration of particles, V_{cell} [m^3], is the volume of the cell, d_{p0} [m], is the local particle diameter, ρ_p [kgm^{-3}], is the particle density and, \vec{u}_{p0} [ms^{-1}] is the local particle velocity. Equation [4.5] assumes a spherical shape of the local particle.

The local particle values are stored in the Eulerian cells in Fluent via user-defined memory (UDM). Those of the cumulative variables, updated during particle tracking, are designated “unseen” and stored in the “upper memory locations” these have no sensible meaning and are only stored to later determine the averaged properties. After a complete injection of steady streams has been calculated the unseen values are converted into meaningful averaged values and transported into “lower memory locations”. In the next run these are the “seen” variables and the inter-particle collision

modelling of the tracked particles uses these values for the local particle. After conversion to the “seen” variables the upper memory locations are reset to zero so that the “unseen” variables may again accumulate.

The accumulative variables are converted into the useful “seen” properties after all stream trajectory calculations have ended. The, respective, changes are ‘the population of particles in the cell’ to ‘the concentration of particles in the cell’ (equations [4.1] and [4.4]), the ‘accumulated mass of particles in the cell’ to ‘the average diameter of the local particles’ (equations [4.2] and [4.5]) and ‘the accumulated mass-navigated distance of particles in the cell’ to ‘the average velocity of local particles’ (equations [4.3] and [4.6]). The effect of the method described is for the total volume of particles “in a cell” to be normalised by the particle population to calculate the average volume (and therefore diameter) which gives a mean particle population and diameter based on the spherical assumption. This property of local particle diameter will be an indication of the distribution of particle sizes at that point in the Eulerian grid. In addition the resultant local particle velocity is the mass average of all streams that pass through the cell.

4.4 Results and Discussion

In this section the experimental and numerical results obtained for the air transportation of the different particulate materials; flour, willow, wood and bark in a pipeline with a 90° elbow, are presented. Various particle mass loading conditions have been established by varying the air mass flow rate and maintaining a constant biomass mass flow rate. Table 4.1 gives the average values of the pertinent properties of the different materials used in this investigation. Flour was selected as a substitute for coal dust. Coal itself was excluded for reasons of safety. It can readily be seen from Table 4.1 that the flour particles are considerably smaller than those of the biomass types, willow, wood and bark. In addition, the biomass particles have a greater aspect ratio and less sphericity. Although greater asphericity implies greater surface area due to shape, the much smaller flour particles have a greater surface area than the other materials on a specific basis and this is due to more particles per kilogramme. Note that the diameter presented in Table 4.1 is that of a cylinder, not the EVS. Therefore similar

mean diameters of the particles do not necessarily entail similar volumes if the aspect ratios are in contrast. Details of the measured air velocities, particle mass flow rates and type of material used in the different test cases are presented in Table 4.2.

Table 4.1 Mean properties of the particles investigated.

Material	Flour	Willow	Wood	Bark
Cylindrical diameter (μm)	321	2531	2285	2458
Aspect ratio	1.37	2.26	1.72	1.70
Sphericity, Φ	0.864	0.818	0.847	0.848
Specific surface area (m^2kg^{-1})	32.71	4.02	4.52	4.21

Table 4.2 Test parameters.

Case	Material	Mass flow rate (gmin^{-1}) (kgs^{-1})	Density (kgm^{-3})	Measured air velocity (ms^{-1})	Loading (%)
1				25	2.0
2	Flour	$54 9 \times 10^{-4}$	520	21	2.5
3				16	3.0
4				24	1.0
5	Willow	$25 4.2 \times 10^{-4}$	480	20	1.1
6				17	1.3
7				Flour & Willow	$54 9.0 \times 10^{-4}$ & $1 1.7 \times 10^{-5}$
8		$54 9.0 \times 10^{-4}$ & $6 1.0 \times 10^{-4}$	480	25	2.2
9				24	1.0
10	Wood	$25 4.2 \times 10^{-4}$	500	20	1.1
11				16	1.4
12				24	1.0
13	Bark	$25 4.2 \times 10^{-4}$	500	20	1.1
14				16	1.4

4.4.1 Validation Data

Figure 4.5 depicts the experimental velocity measured by the first two electrodes of each electrode group under different flow conditions, in which 'F54W1' means the mass flow rate of flour and willow are 54gmin^{-1} and 1gmin^{-1} , respectively. This shows that the correlation velocity of the mixture flow is consistently lower than that of the pure flour flow and that the correlation velocity decreases with the mass ratio of willow in the mixture. The radial distribution of the particles is inferred from the relative charge levels received by the banks of arc sensors in Figure 4.6. Due to their different physical properties and the gravitational effect, the biomass flow travels slower in the vicinity of the bottom of the pipe, but the flour flows slightly slower near the sides of the pipe compared to the central portion. Figure 4.6(a) shows the RMS charge readings from the annular electrostatic sensor. It is reasonable that the charge levels measured from the circular electrodes (Group E) are considerably higher than that measured from the arc-shaped electrodes because the circular electrodes sense the flow circumferentially while the arc-shaped electrodes measure the "local" particle charges. Therefore Figure 4.6(a) cannot be compared to the other readings, in Figures 4.6(b)-(d), but shows the general increase in charge readings with air velocity and that the charge levels increase when a higher total flow rate of particles is used. This is most likely due to a greater number of higher velocity wall collisions increasing the electrostatic charge on the particles. Figures 4.6(b)&(c) also present the trend of increasing charge with mass flow rate and conveyor velocity, except for the 20ms^{-1} 54 and 1gmin^{-1} case which is acceptable considering the measurement tolerances. As can be seen from the RMS values, more flour particles travel in the sides of the pipe than in other parts of the pipe whilst biomass particles are distributed relatively uniformly across the pipe. In addition these figures show a trend for low readings in the lower quadrant, suggesting gravitational stratification of the particles. Comparing the cases of 54F and 54F1W, one reason why less than a 2% increase in the total flow rate adding willow, a material that is expected to have a lower charge than the flour, causes such a magnitude change to the residual charge readings, particularly in the middle and lower quadrants is that the large willow particles may agglomerate a coating of smaller flour particles causing large but

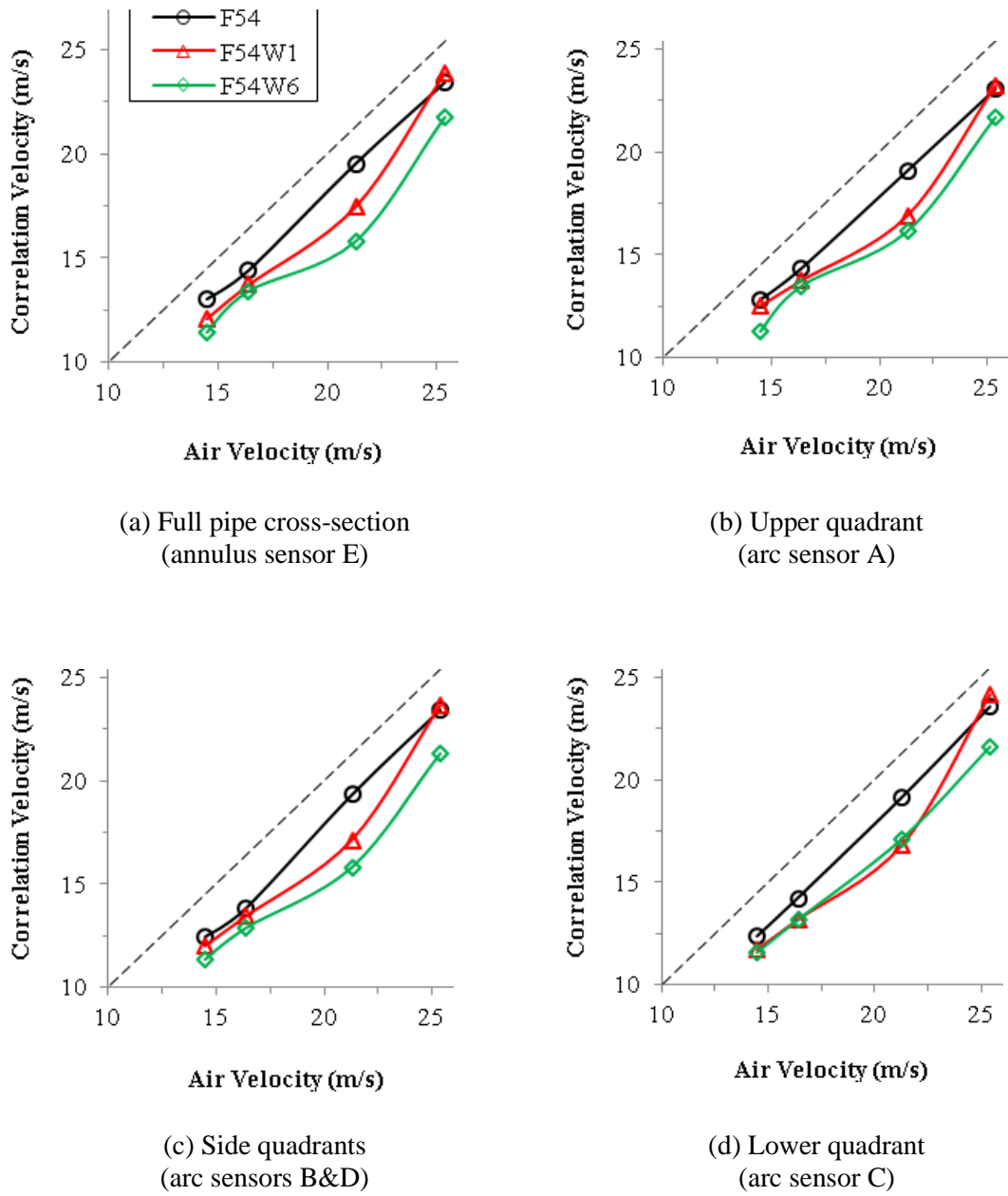
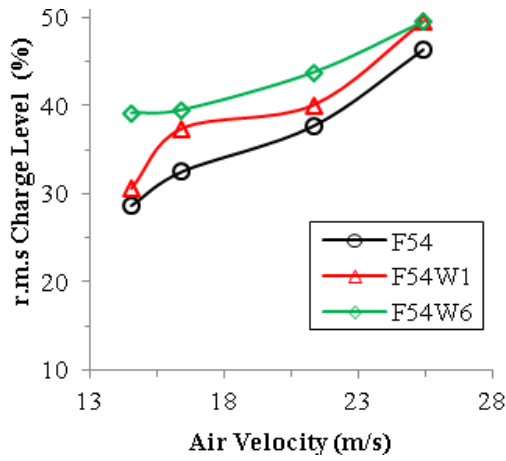
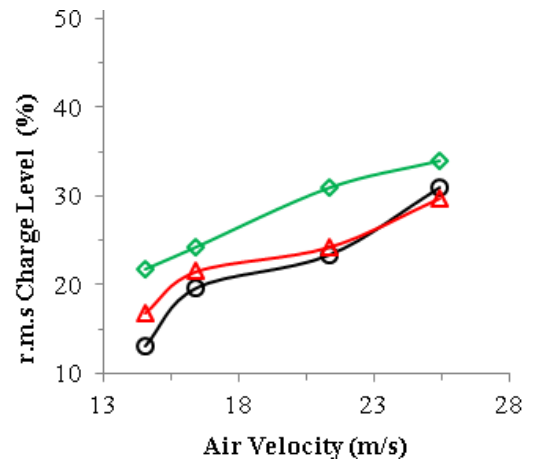


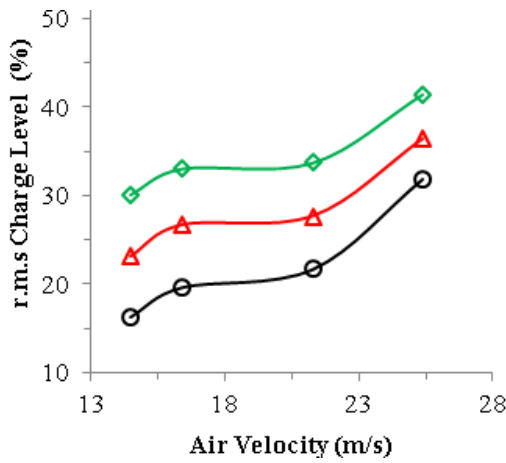
Figure 4.5 Flour and willow experimental velocities.



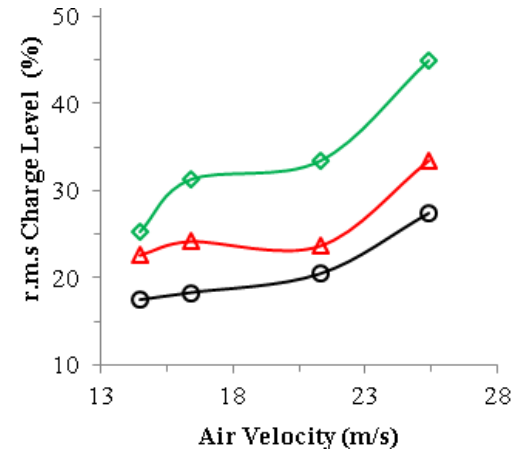
(a) Full pipe cross-section
(annulus sensor E)



(b) Upper quadrant
(arc sensor A)



(c) Side quadrants
(arc sensors B&D)



(d) Lower quadrant
(arc sensor C)

Figure 4.6 Flour and willow experimental charge levels.

infrequent peaks in the charge reading. This would be less pronounced in the upper quadrant due to the scarcity of the heavy willow particles in this region.

4.4.2 Modelling Results

There are eight different cross-sectional locations, at regular intervals, within the measurement section of the pipe, which represent the annular and arc electrodes, as shown in Figure 4.3. This representation mimics the experiments, in data collection from the CFD simulations, serving two purposes, firstly to provide detailed information about the particles in any chosen plane, and secondly the relative particle behaviour between planes. Figure 4.7 shows the eight axial locations considered in the CFD domain and the respective air velocity vector and contour plots at individual planes. The plane names, z350, z366 etc. denote the axial pipe distance from the start of the measurement section to the plane in mm.

Prior to presenting the particulate data, it is important to ensure that the gas phase is correctly resolved. From the CFD simulations, it is observed that within the measuring locations/planes of the pipe, the flow is not fully developed. Hence, comparing the air velocities within this region may be inappropriate. However, beyond the measuring locations, i.e. about 2.8m after the elbow, the flow is identified to be fully developed. This has been confirmed by comparing the gas phase velocity profiles at various axial locations for various cases investigated. Figure 4.8(a) presents air velocity predictions for six cases described in Table 4.2, in which the experimental velocities, in order of cases 1-6, are 25, 21, 16, 24, 20 and 17ms^{-1} . The numerical predictions show excellent agreement with these values at the centreline. In order to validate the CFD calculations, the gas phase axial velocities are compared against the experimental measurements of Perry *et al.* (1986), at similar Reynolds numbers to those investigated, as presented in Figure 4.8(b). The numerical predictions near the walls are slightly under predicted and this can be mainly attributed to the presence of higher shear stresses at the wall which does not impose a significant impact on the particulate flow.

In the following sections, data collected from the CFD simulations are grouped into different sets based on the biomass material and the results obtained are compared with the available experimental data. In each set, an additional CFD simulation at the

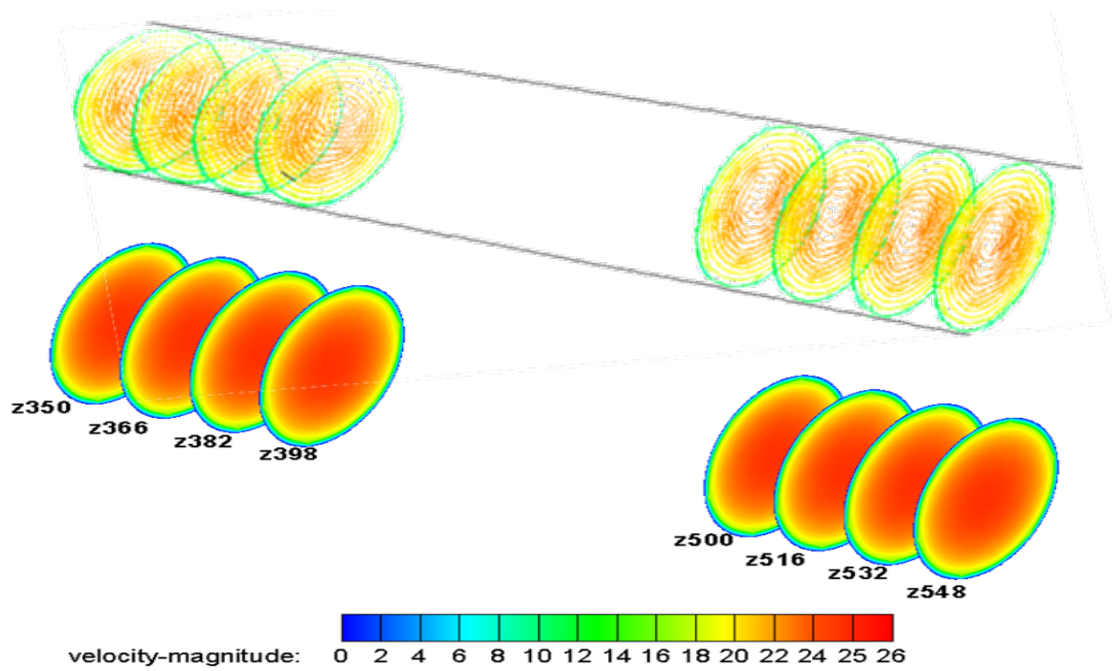


Figure 4.7 Numerical fluid phase velocity vectors and contour plots at the sensor planes.

Plane names, z350, z366, z382, z398, z500, z516, z532 and z548 denote the displacement of the plane from the start of the measurement section (mm). The first four represent annular sensor and the latter four the arc sensor locations.

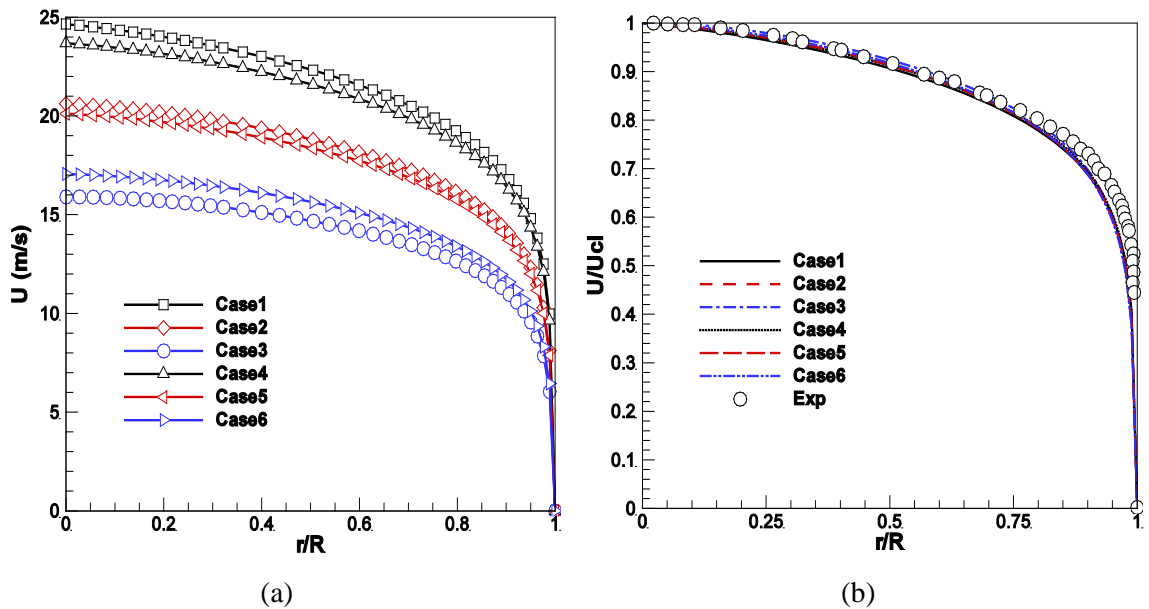


Figure 4.8 Air velocity predictions and measurements.

(a) Axial velocity profiles of the air for the six different cases investigated are plotted against the non-dimensionalised radial location. (b) Axial velocity, non-dimensionalised by the centre line axial velocity, against the non-dimensionalised radial location. The experimental measurements from Lin and Liu (1997) are plotted and denoted by circles.

highest conveying velocity has been repeated using spherical drag models and those are named as the case number appended by “Spherical”. The reason for doing this is to investigate the relative improvement in the predictions when using a non-spherical drag model and therefore the influence of particle shape.

4.4.3 Results - Flour

Table 4.3 provides details of the particle diameters, aspect ratios and their corresponding percentage volume contribution for a typical flour sample as investigated. This information has been obtained by using an optical scanner, based on static imaging techniques at the University of Kent. Using these data, 30 different particle streams with estimated shape factors are injected into the inlet of the CFD domain. For simplicity particles having an aspect ratio of unity are assumed to be of spherical shape and all other particles are assumed to be cylindrical in shape due to a lack of detailed information. It is worth mentioning that 47.6 % of the volume of flour particles is therefore modelled as spheres.

Three Cases, i.e. 1, 2, and 3, at different conveying velocities (25, 21 and 16ms⁻¹) and particle loadings (2.0, 2.5 and 3.0% by mass) have been investigated. In addition Case 1 has been repeated using spherical particle physics, labelled 1-Spherical. Particle phase simulations are performed by considering approximately 10⁵ representative particle streams. As mentioned earlier in section 4.3, regarding the DRW model, ten ‘tries’ of each particle stream are simulated, i.e. about 10⁶ trajectories are tracked using

Table 4.3 Percentage by volume of the contribution of flour particles.

Particle diameter (μm)	Aspect ratio					% of Volume
	1.0	1.5	2.0	2.5	3.0	
180	5.6644	4.1888	1.5232	0.4284	0.0952	11.9
250	20.6584	15.2768	5.5552	1.5624	0.3472	43.4
355	14.7084	10.8768	3.9552	1.1124	0.2472	30.9
500	4.8076	3.5552	1.2928	0.3636	0.0808	10.1
710	1.0472	0.7744	0.2816	0.0792	0.0176	2.2
1000	0.7140	0.5280	0.1920	0.0540	0.0120	1.5
% of Volume	47.6	35.2	12.8	3.6	0.8	100

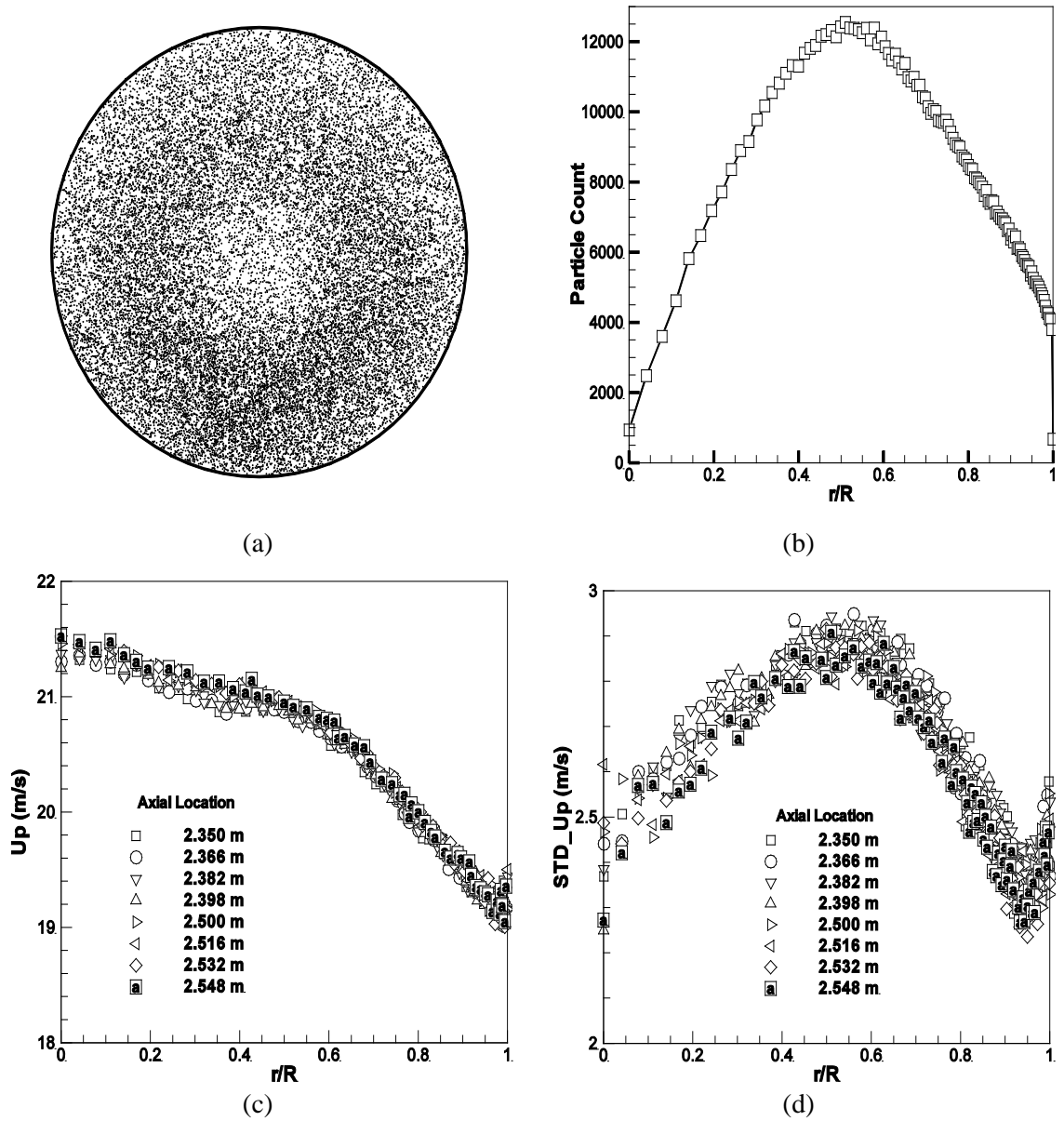


Figure 4.9 Numerical prediction of Case 1 – 54gmin⁻¹ flour.

(a) Particle distribution across the pipe at 2.5m after the pipe elbow. (b) Number distribution of the particles in the pipe in a plane at 2.5m after the pipe elbow. (c) Numerical predictions of the particle axial velocity for Case 1 plotted against the non-dimensionalised radial location at various axial locations. (d) Numerical predictions of the standard deviation of the particle axial velocity for Case 1 plotted against the non-dimensionalised radial location at various axial locations.

Lagrangian particle tracking to calculate the position, velocity and wall interactions of the particles. However, it should be noted that the true number of particles in the system is of the order of 6×10^8 per second of residence time.

Figures 4.9(a)&(b) present typical particle location distributions and radial particle count in an axial plane at 2.5m after the elbow for Case 1, flour particles. It is interesting to note that the central portion of the pipe is less dense with particles compared to annular cross-section at the central radius. Although particles are not settling at the bottom of the pipe at this location, a higher concentration of particles are observed towards the lower part of the pipe when compared to the upper part of the pipe. The particle distribution on other planes is not presented here because there is similar particle behaviour at all measurement locations. The particle concentration stratification may be due to the inclusion of gravitational effects in the CFD simulations. Figure 4.9(c) depicts the mean axial velocity of the particles at various planes within the measuring portion of the pipe. It is very interesting to note that the mean particle axial velocity presented in Figure 4.9(c) is identical and represents the same velocity profile at all the planes.

Figure 4.9(c) presents the behaviour of the particles near pipe walls. It should also be noted that some of the near wall particles are transported at higher velocities compared to their neighbouring particles. However, a close investigation reveals that two velocity profiles exist, one corresponds to that near the bottom wall and the other corresponds to the upper wall portion. This may be that the particles near the upper wall are being transported at a higher velocity compared to their neighbouring particles. Chinnayya *et al.* (2009) identify an analogous behaviour to that observed here. One explanation is that the presence of lighter particles near the top wall being conveyed at a slightly higher velocity compared to the heavier particles are observed. Figure 4.9(d) presents the standard deviation in the particle velocities at various axial locations.

Figures 4.10(a)&(b) present the mean axial velocity of the particles and their standard deviations from all the measuring planes for Cases 1, 2, 3 and 1-Spherical. This representation is expected to identify the relative behaviour of the particles at different conveying velocities and the influence of particle loading. The particle velocity profiles, and their standard deviations, in Cases 1, 2 and 3, are consistent and follow the

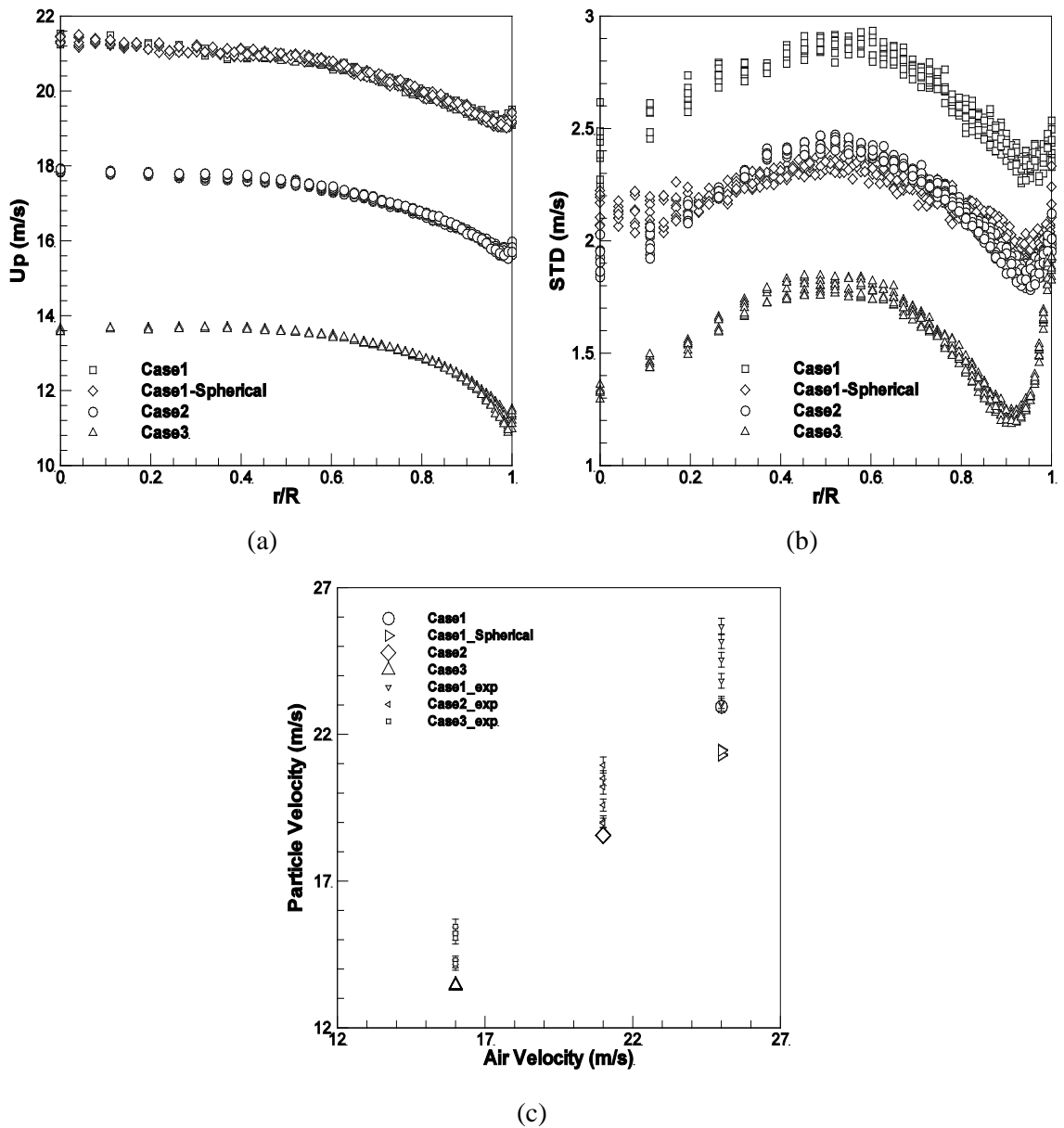


Figure 4.10 CFD predictions and experimental measurements for Cases 1, 2, 3 and 1-Spherical involved in flour transportation.

(a) Mean axial velocity of the particles against the radial location (r), non-dimensionalised by the pipe radius (R). (b) The standard deviation of particle velocity across the plane against the radial location (r), non-dimensionalised by the pipe radius (R). (c) Predicted mean particle velocity against mean cross-correlated velocity from measured data with corresponding error bars.

same general trends. Subtle differences in the particle velocity trends may be observed in Cases 1 to 3 and this may be due to the Reynolds number. The mean axial velocity trends of particles for Cases 1 and 1-Spherical are identical and are as shown in Figure 4.10(a). The reason for this identical behaviour is postulated to be the highly spherical shape of the particles considered in Case 1, since 47.6 % of the mass of particles have an aspect ratio of about 1.0 and a further 35.2 % of the particles have an aspect ratio of about 1.5. Figure 4.10(c) presents the mean cross-correlated velocities obtained from experiments with respective error bars for Cases 1, 2, and 3. It should be noted that the exact radial and tangential locations of the detected particles are unidentifiable by experiments, although, in general, the highest charge carrying particles are sensed. The predicted mean axial velocities at the centreline of the pipe in every measuring plane are also presented in Figure 4.10(c). It is interesting to note that the CFD predictions of the mean particle axial velocities are in reasonable agreement with the experimental measurements, including when using the spherical drag model for the flour particles.

4.4.4 Results - Willow

As seen in Figure 4.1(a), and the data from Table 4.4, willow particles range in size from 500 to 5600 μm , and many willow particles are highly acicular. Due to the large range of particle sizes of willow, 40 different particle streams are injected into the inlet. Cases 4, 5 and 6 are simulated with a constant willow mass flow rate of 25 gmin^{-1} and conveying velocities of 24, 20 and 17 ms^{-1} , respectively. A CFD simulation assuming that the willow particles are spherical is also performed using the same conditions as for Case 4 and this is named 'Case 4-Spherical'. These results are of assistance in understanding the influence of the non-spherical drag model for particles that represent a greater divergence from sphericity than for the case of flour. Figures 4.11(a)&(b) present the mean axial velocities of the willow particles and their standard deviations at various conveying velocities. We observe that the velocity profiles of willow particles are following the same general trend at various conveying velocities. Although the velocity profile from Case 4-Spherical is also found to follow the same trend as of Case 4, it severely under predicts the particle mean axial velocity.

Figure 4.11(c) presents the mean cross-correlated velocities from the experiments for Cases 4, 5 and 6 along with error bars. The predicted mean particle velocities on the centreline of the pipe are plotted for all the cases investigated. It is evident that the computed mean velocities for the Cases 4, 5 and 6 are in good agreement with the measurement data. It is also clear from Figure 4.11(c) that the particle velocities, as calculated using the spherical drag model, are severely under predicted compared to the results obtained from the non-spherical drag model and the experimental data. It is found in both Cases 4 and 4-Spherical that the particle Reynolds numbers range between 300 and 12000 at the measuring locations of the pipe. The assumption of spherical particles reduces the drag coefficient, compared to the fixed-orientation non-spherical method, at all Reynolds numbers. This results in a higher lag velocity but also more inertial particle response. The standard deviation of the particle axial velocity presented in Figure 4.11(b) for Case 4-Spherical is higher than in Case 4, and this establishes the range of particle velocities predicted in both cases.

Table 4.4 Percentage by volume of the contribution of willow particles.

Particle diameter (μm)	Aspect ratio					% of Volume
	1.0	1.5	2.0	2.5	3.0	
500	0.0715	0.2431	0.3601	0.1950	0.4303	1.3
710	0.1100	0.3740	0.5540	0.3000	0.6620	2.0
1000	0.2860	0.9724	1.4404	0.7800	1.7212	5.2
1400	0.6765	2.3001	3.4071	1.8450	4.0713	12.3
2000	1.3200	4.4880	6.6480	3.6000	7.9440	24.0
2800	2.1120	7.1808	10.6368	5.7600	12.7104	38.4
4000	0.7205	2.4497	3.6287	1.9650	4.3361	13.1
5600	0.2035	0.6919	1.0249	0.5550	1.2247	3.7
% of Volume	5.5	18.7	27.7	15.0	33.1	100

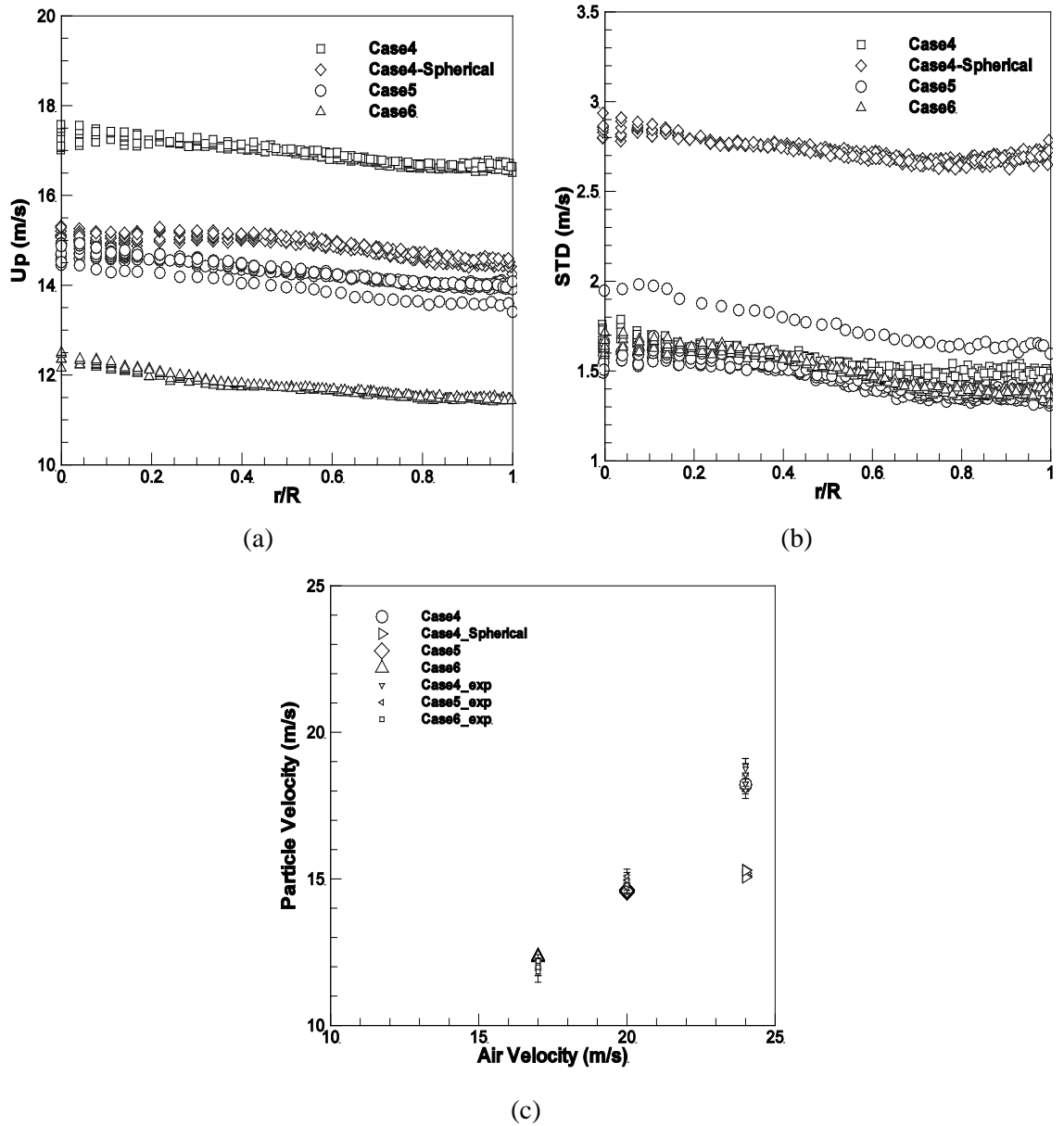


Figure 4.11 CFD predictions and experimental measurements for Cases 4, 5, 6 and 6-Spherical involved in willow transportation.

(a) Mean axial velocity of the particles against the radial location (r), non-dimensionalised by the pipe radius (R). (b) The standard deviation of particle velocity across the plane against the radial location (r), non-dimensionalised by the pipe radius (R). (c) Predicted mean particle velocity against mean cross-correlated velocity from measured data with corresponding error bars.

4.4.5 Results – Mixture of Flour and Willow

Cases 7 and 8 as described in Table 4.2, are investigated using a mixture of flour and willow. The mass flow rate of the flour is kept constant at 54gmin^{-1} and the mass flow rate of the willow is 1 and 6gmin^{-1} in the Cases 7 and 8, respectively. In addition, using the conditions of Case 8, the CFD simulation is performed using the spherical drag model named ‘Case 8-Spherical’.

Figure 4.12(a) presents the particle distribution in Case 8 for a mixture of flour (red) and willow (black). Figures 4.12(b)&(c) present the mean particle axial velocity and their standard deviation. The velocity profiles of the particles in these cases are very close to each other and follow a similar trend. Although the mass flow rate of the willow in Case 8 differs by 5gmin^{-1} , the particulate conveying velocity is the same in Cases 7 and 8 and hence this provides a platform to compare the mixture behaviour. It is interesting to note that the particle velocities predicted in the centre region of the pipe are close to each other, but higher particulate velocities have been achieved in Case 8 due to the higher mass flow rate. Differences in the particulate axial velocities in Cases 7 and 8 are clearly observed for r/R between 0.25 to 1.0. Figure 4.12(a) suggests a higher concentration of flour and willow away from the central region of the pipe. In Case 8-Spherical, the results follow a similar trend to that present in Case 8. However, a lower mean particle axial velocity from the axis of the pipe centre to the bottom wall of the pipe is observed due to the use of the spherical drag model. The differences between the particle velocity profiles in Cases 8 and 8-Spherical are due to the assumption of spherical flour and willow particles. The impact upon the conveying velocity is marked, in harmony with the change between Cases 4 and 4-Spherical, Figure 4.11(a). Comparing the predicted velocity trends of the spherical and non-spherical treatment of Case 8 indicates that the difference in particle velocity increases from the pipe axis to the pipe wall.

Although the standard deviations presented in Figure 4.12(c) for Cases 7 and 8 overlap, this confirms that small changes in the material mass flow rate have significant effects on the particle axial velocities that cannot be neglected in real flow problems.

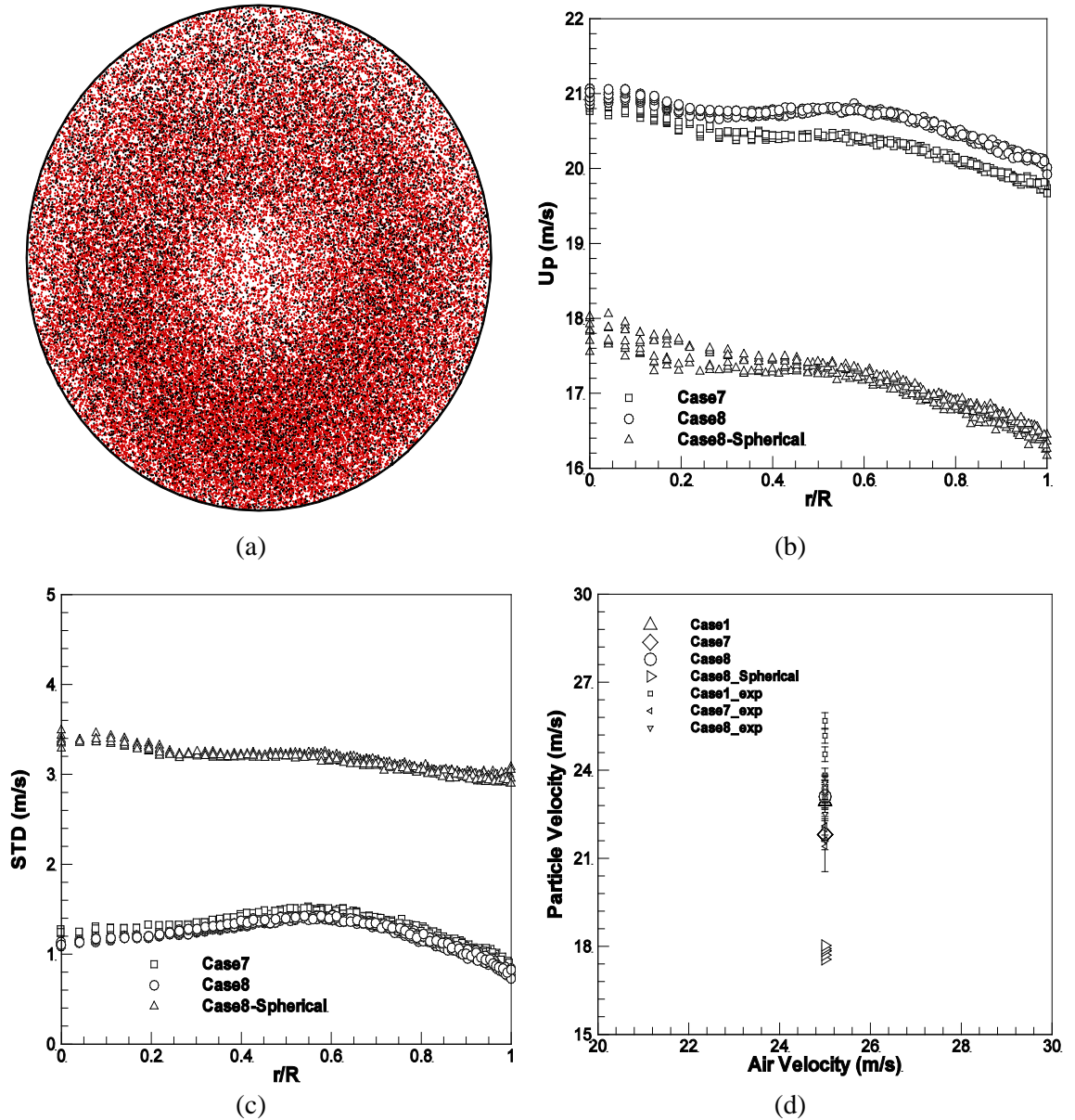


Figure 4.12 CFD predictions and experimental measurements for Cases 7, 8 and 8-Spherical involved in flour and willow transportation.

(a) Mean axial velocity of the particles against the radial location (r), non-dimensionalised by the pipe radius (R). (b) The standard deviation of particle velocity across the plane against the radial location (r), non-dimensionalised by the pipe radius (R). (c) Predicted mean particle velocity against mean cross-correlated velocity from measured data with corresponding error bars. Case 1, flour, has been included for comparison.

Figure 4.12(d) presents the mean correlated velocities obtained from experimental data and the predicted mean particle velocities at the centreline. The improvement obtained using the non-spherical drag model is once again evident by comparing the numerical predictions of Cases 8 and 8-Spherical. In general, the numerical predictions for Cases 7 and 8 are in good agreement.

Table 4.5 Percentage by volume of the contribution of wood particles.

Particle diameter (μm)	Aspect Ratio					% of Volume
	1.0	1.5	2.0	2.5	3.0	
355	1.0280	1.2880	0.920	0.4280	0.3360	4.0
500	0.3598	0.4508	0.322	0.1498	0.1176	1.4
710	0.6425	0.8050	0.575	0.2675	0.2100	2.5
1000	1.7990	2.2540	1.610	0.7490	0.5880	7.0
1400	4.2405	5.3130	3.795	1.7655	1.3860	16.5
2000	6.9390	8.6940	6.210	2.8890	2.2680	27.0
2800	5.5512	6.9552	4.968	2.3112	1.8144	21.6
4000	5.1400	6.4400	4.600	2.1400	1.6800	20.0
% of Volume	25.7	32.2	23.0	10.7	8.4	100

Table 4.6 Percentage by volume of the contribution of bark particles.

Particle diameter (μm)	Aspect ratio					% of Volume
	1.0	1.5	2.0	2.5	3.0	
355	0.3055	0.4745	0.3146	0.0988	0.1066	1.3
500	0.0940	0.1460	0.0968	0.0304	0.0328	0.4
710	0.5405	0.8395	0.5566	0.1748	0.1886	2.3
1000	1.5980	2.4820	1.6456	0.5168	0.5576	6.8
1400	4.3475	6.7525	4.4770	1.4060	1.5170	18.5
2000	5.2875	8.2125	5.4450	1.7100	1.8450	22.5
2800	5.2875	8.2125	5.4450	1.7100	1.8450	22.5
4000	6.0395	9.3805	6.2194	1.9532	2.1074	25.7
% of Volume	23.5	36.5	24.2	7.6	8.2	100

4.4.6 Results – Wood and Bark

Tables 4.5 and 4.6 provide details of the size, aspect ratio and respective volume contribution for wood and bark. Interestingly, the size distribution, volume contributions and shapes (see Figures 4.1(b)&(c)) of wood and bark are of closely related values, thus yielding similar particle populations. Moreover, the conveying velocities and mass flow rates of the particles for the two materials cannot be distinguished. That is why, although the individual material flows have been investigated, they have been incorporated into a single section. Figures 4.13 and 4.14(a)-(c), present the CFD model predicted mean axial velocity profiles, standard deviations and experimental measurements for the wood and bark particles, respectively. It is remarkable to note that irrespective of the subtle changes in the particle distributions and volume, the axial velocity profiles and their standard deviations are almost identical, except in the vicinity of the wall. It is also worth mentioning that the particulate axial velocities and their standard deviations for Cases 9-Spherical and 12-Spherical are identical and follow the trend of the non-spherical drag model.

The experimental data and numerical predictions presented in Figures 4.13(c) and 4.14(c) are in good agreement for both the materials (wood and bark). This suggests that the physical properties of the wood and bark samples employed in the experiments and CFD are very similar. As expected, the CFD simulations using the spherical drag model are found to under predict the particle velocity and produce almost identical values for both wood and bark.

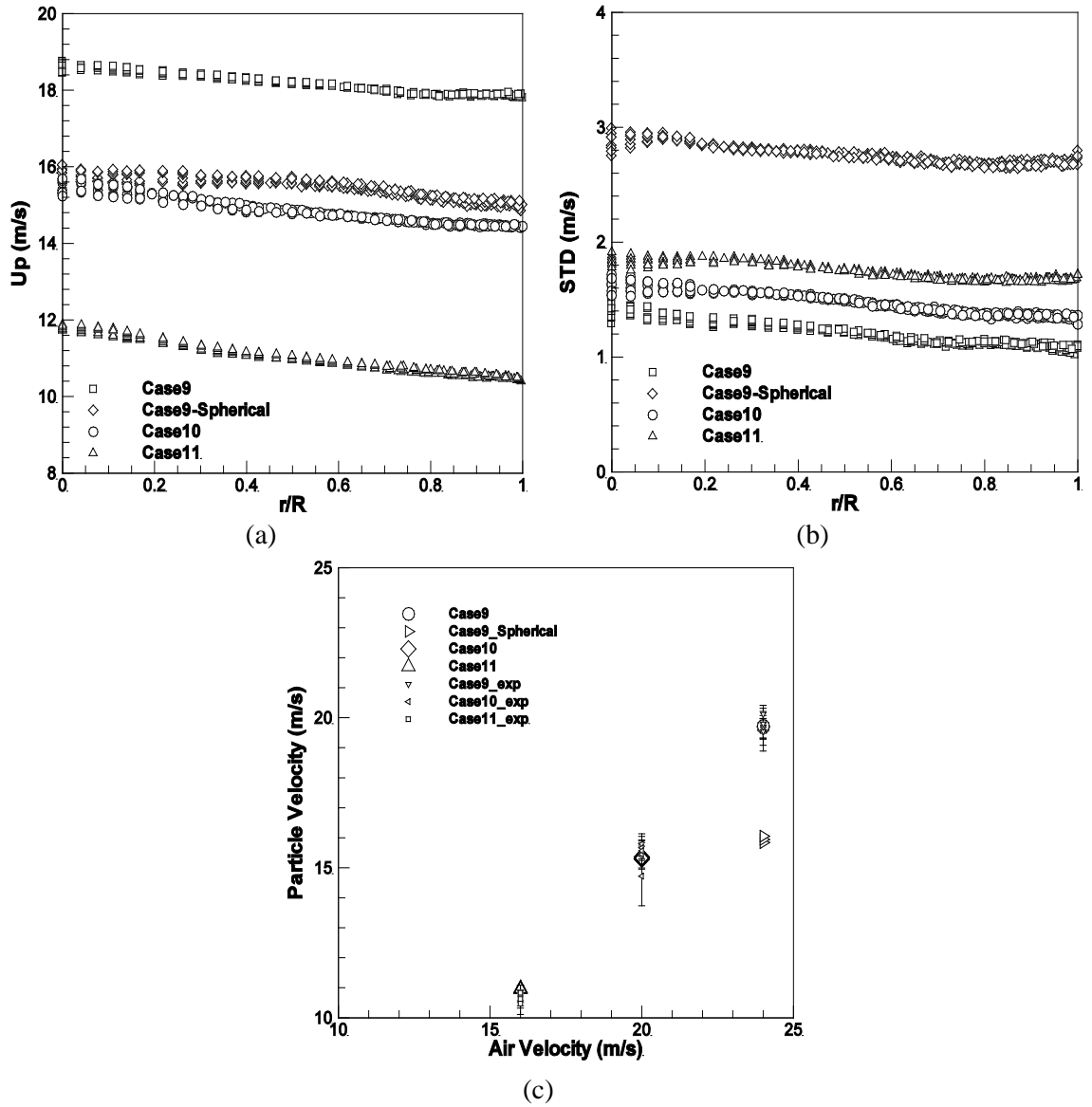


Figure 4.13 CFD predictions and experimental measurements for Cases 9, 10, 11 and 9-Spherical involved in wood transportation.

(a) Mean axial velocity of the particles against the radial location (r), non-dimensionalised by the pipe radius (R). (b) The standard deviation of particle velocity across the plane against the radial location (r), non-dimensionalised by the pipe radius (R). (c) Predicted mean particle velocity against mean cross-correlated velocity from measured data with corresponding error bars.

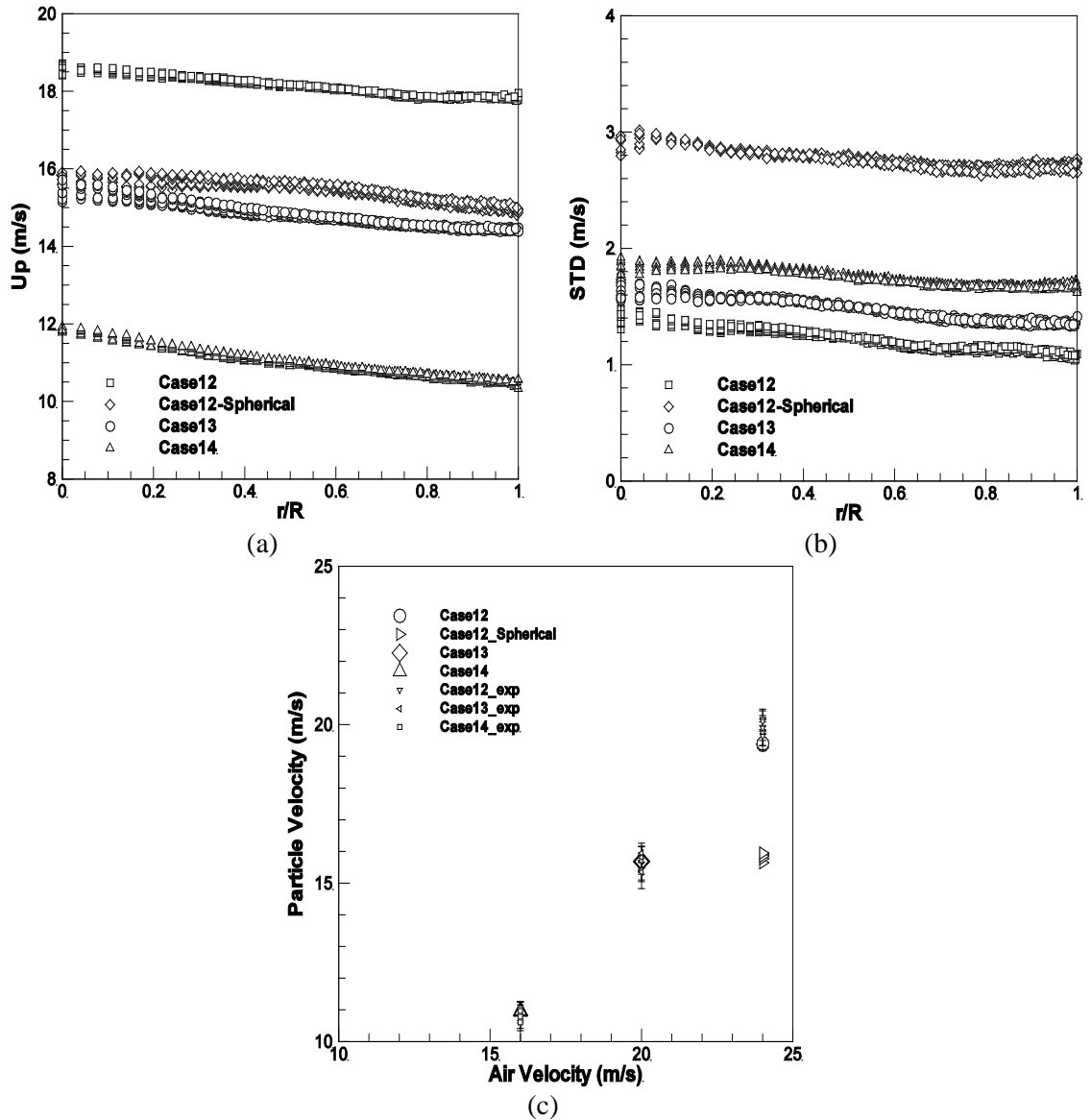


Figure 4.14 CFD predictions and experimental measurements for Cases 12, 13, 14 and 12-Spherical involved in willow transportation.

(a) Mean axial velocity of the particles against the radial location (r), non-dimensionalised by the pipe radius (R). (b) The standard deviation of particle velocity across the plane against the radial location (r), non-dimensionalised by the pipe radius (R). (c) Predicted mean particle velocity against mean cross-correlated velocity from measured data with corresponding error bars.

4.4.7 Inter-Particle Collisions

The simulation presented for Case 1 was repeated, including the UDF inter-particle collision method as described in section 3.2, in order to assess its effects. The technique is significantly more computationally expensive due to the generation of the order of 10^6 random numbers during the trajectory calculations of a full injection of particles and moreover because of the iterative particle injection process whilst the “local particle” properties field is evolved to a pseudo-steady state in the Eulerian domain. In the current study, no appreciable change in the particulate flow can be detected by including inter-particle collisions when compared to the results obtained by omitting such collisions. It is likely that the occurrence of an inter-particle collision event is too rare for a consistent change in the particle behaviour to be perceived under the present loading conditions. Another factor which diminishes the influence of inter-particle collisions is the counter rotating flow structure within the horizontal section of the pipe. Inter-particle collisions are thought to be particularly important in horizontal turbulent flows, in which gravity may be expected to dominate the transverse velocities, because they assist in maintaining the suspension above the pipe wall and out of the laminar shear layer. The closer relative axial velocity between particles, as opposed to between the particles and the wall, and the higher fluid velocities in the turbulent region of the conveying fluid assist in entraining the particles. However, in this chapter, following the pipe elbow, the axial vortices present an important mechanism for the particles to oppose gravity and induce a fully mixed suspension of the particles.

4.5 Chapter Summary

Online particle flow measurements and CFD calculations of dispersed biomass particle transportation in high Reynolds number pipe flows have been carried out using flour, willow, wood and bark. The on-line measurements are performed using a novel electrode sensor system. A perpendicular vertical→horizontal elbowed pipeline resembling a typical industrial pipeline was specifically designed for experimental measurements and modelled in CFD. Different conveying velocities were tested by varying the air mass flow rate and maintaining constant particle mass flow rate. Gravity effects, wall and inter-particle collisions were also considered.

Figure 4.15 presents the axial velocity of the particles for various cases, namely Cases 1 (flour), 4 (willow), 7 (flour & willow), 8 (flour & willow), 9 (wood) and 12 (bark). Whilst making the comparison between the cases of this plot (Figure 4.15), it is of use to note that the particles in Cases 1, 7 and 8 were conveyed at 25 ms^{-1} with various mass flow rates, whereas in Cases 4, 9 and 12 they were conveyed at 24 ms^{-1} with the same mass flow rate. Subtle differences in the conveying velocities and the particle densities in these cases are not expected to play a major role in the varying lag velocities presented.

The online experimental results presented indicate that the movement behaviours and flow characteristics of the flour/willow mixture flow differ from those of pure flour flow or pure biomass flow. The flour particles travel faster and carry higher electrostatic charges than biomass particles under the same test condition. The flour and willow particles are well mixed and travel together in the pipeline under the lower velocity conditions, while the two materials gradually separate out and run at slightly different velocities as the flow speeds up. The mixture flow becomes less stable as the conveying air velocity increases, especially in the middle and bottom regions of the pipe cross-section. In addition, the mixture flow travels slightly slower than the pure flour flow and does not have a fine linear relationship with the conveying air velocity. For the circular electrodes there are no significant differences between the pure flour flow and mixture flow.

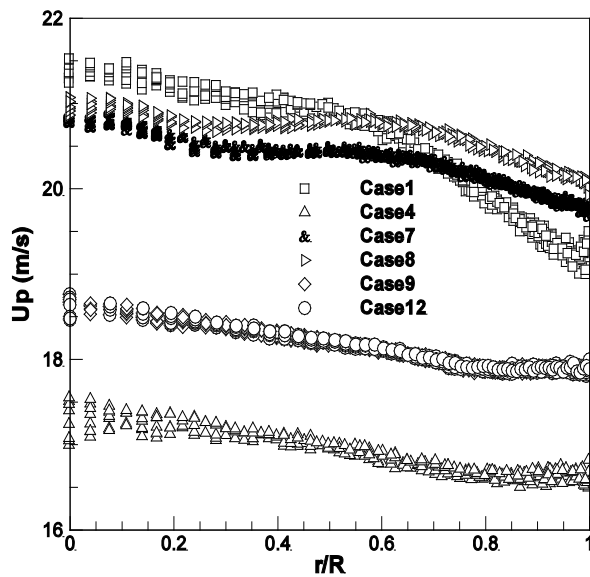


Figure 4.15 Mean axial velocity of the particles against normalised pipe radius.

Cases 1, 4, 7, 8, 9 and 12 involving the various biomass, respectively; flour, willow, flour & willow, flour & willow, wood, and bark.

The CFD calculations, in general, were found to be in very good agreement with measured particle velocities and thus show that the CFD modelling approach employed is valid for the cases studied and may be employed to deal with industrial pipelines with elbow sections. Compared to a basic non-spherical drag model, the standard spherical drag model was identified to under predict the particle velocities for all the materials except flour. This clearly demonstrates the influence of the estimated shape factor in non-spherical drag model. Particles near the top wall of the pipe were found to travel slightly faster. Physically this may be caused by a slower core of air lower in the pipe due to a faster transfer of kinetic energy between the fluid and suspended particles in regions of greater particle concentration. However, two-way coupling was not employed numerically and so an identical effect must have been caused by preferential separation of the particles of lowest mass and greatest specific surface area. Such particles assume the highest velocities opposing gravity, due to their greater obedience to the transverse fluid velocity, in order to separate into the higher regions of the pipe. In addition these same particles will present the lowest lag velocity, behind the fluid, of all the particles. The low Stokes' numbers of these particles ensure that they would also slow the most rapidly in proximity to the pipe walls. However, the tests have been performed under

high turbulence conditions and the upper quadrant, as defined by the experiments, is the whole semi-circular cross-section, therefore the boundary layer will not penetrate so far as to preclude the increased particle velocities.

Case 1 has the fastest conveying velocity at the centre of the pipe. As seen in Table 4.2, flour has the smallest particles with a significantly larger specific surface area compared to that of the other materials investigated. This presents the least inertial response to the fluid and this is clearly influenced by the lower fluid velocities in the near wall region. The willow particles, Case 4, are on average the largest and least spherical particles, although size must dominate as they also possess marginally the lowest specific surface area. This case represents the highest lag velocity and a flatter profile than for the flour cases. Considering that Cases 7 and 8 have respective mixture compositions of 98% and 90% flour by mass (the remainder being willow), the marked difference between their profile behaviours and that of Case 1 is surprising. This may be due to the ensemble averaging having a greater refinement of the unusual willow particle spectrum, considering the respective mass flow rates of the mixture components may emphasise the willow's contribution. Also observing the materials' individual responses and properties, a mass weighted average of the expected particle axial velocities would favour Case 7 being the faster, albeit not significantly. As the velocity difference between Cases 7 and 8 is never greater than 0.5ms^{-1} , and they are very close along the centreline, which is the target area for the experimental measurement, the conclusion is that the predicted values of particle velocities are tolerably equal (see Figure 4.15).

Despite similar average diameters for the willow and bark particles, see Table 4.2, the mass of the willow is approximately 140% that of bark and this is due to the greater average aspect ratio of the willow. Opposed to this the average wood and bark particles are almost identical and have specific surface areas between those for flour and willow. The experimental data match the CFD predictions from these properties as the velocity magnitude is between that of flour and willow, the flat mean axial particle velocity profile is akin to that of willow in a more inertial response, due to greater particle relaxation times, and those of wood and bark are almost indistinguishable. Inter-particle

collisions were found to be insignificant in these tests. This is due to the low volume loading of particles and lateral recirculating flows that entrain the particles.

Chapter 5

The Modelling of Coal and Biomass Pneumatic Transportation in a Swirl Burner

5.1 Introduction

The method of pulverised coal and biomass co-firing of interest in this chapter is that of fuel premixing and injection into the furnace via shared burners. Pulverised fuels are transported pneumatically from the mills to the boiler, however in computational fluid dynamics (CFD) the extents of the computational domain are generally retracted to the furnace interior and so an assumption as to the particle distribution at this point is used as input. The behaviour of a three-phase mixture of coal particles, biomass particles and carrier air may differ from the even distribution of particles and gas phase velocity assumption that is most commonly adopted. The shared burner co-firing method is a particularly attractive low cost solution to low load co-firing and favourable to retrofit on coal power stations. The decision making for utilising a dedicated hopper or dedicated mills method, as introduced in section 1.1 is discussed here. At very low loadings of processed biomass, the fuel streams could be mixed prior to milling. At moderate loadings, and with virgin biomass, dedicated hammer mills may be required and the drying and transport air must be carefully controlled to prevent mill fires. The simplest method remains however to mix the fuels after both are milled through shared burners. Sustainable combustion of the biomass through dedicated burners, designed for coal firing, may be difficult to achieve at the thermal power of biomass injected or require additional processing of the fuel. This chapter examines the numerical prediction of three-phase modelling of coal and biomass pneumatic suspensions through a low-NO_x swirl burner. The burner geometry investigated was that of the RWE Npower test rig at Didcot. This particular burner is selected since numerical modelling of coal and biomass co-firing on a Mitsui Babcock Mark III burner has previously been undertaken by the University of Leeds, and therefore the dimensions are known. In addition, it is clearly a design that is used and further harmful emissions legislation is

ever being tightened, so such NO_x reduction hardware, as swirl burners, is likely to remain in operation.

Coal combustion modelling and simulation has received much investigation and is reasonably well understood. Historically wood and coal co-firing has also been studied with different goals. The method was implemented to, relatively inexpensively, reduce NO_x and SO_x from coal combustion. However, the simulation of biomass transport and combustion still presents challenges in that the particle aerodynamics may not follow the established assumptions for coal particles, this is due to the irregular particle shape. Also the greater size may invalidate the assumptions of uniform temperature throughout the particle and the sequential combustion stages. These problems preclude simulation to estimate the very real physical effects of slagging and fouling and also the unburnt-carbon (UBC) in ash, which can translate to wasted fuel and worthless bottom ash. Complicating matters is the vast array of materials under the label biomass and the very large variance within an individual species/product. Virgin biomass particle size and shape, and the combustion and ash properties can change according to which parts are being harvested, the climate, time of year, fuel handling and even the rate of milling.

5.1.1 Description of the Combustion Test Furnace

A photograph of the RWE 0.5MW_{th} combustion test furnace is shown in Figure 5.1 and this is superimposed with a diagram showing the internal connections of the burner duct and the CTF combustion chamber. The dimensions of the furnace and the burner details have previously been published (Edge *et al.*, 2011).

The investigation in this chapter is mainly concerned with the distributions of the fuel particle flows in the primary air tube that is schematically shown in Figure 5.2. Pulverised coal and biomass fuels are gravity fed, vertically, to the annulus of the primary air duct leading to the combustion chamber. The inner diameter of the primary air annulus is 76mm, whereas the outer diameter is reduced to 122mm following a conical reduction section. This primary air tube is surrounded by secondary and tertiary air ducts, that are not shown in this diagram, where contra-flow swirled air flows enter the combustion chamber. There is a flame holder mounted at the end of the primary air

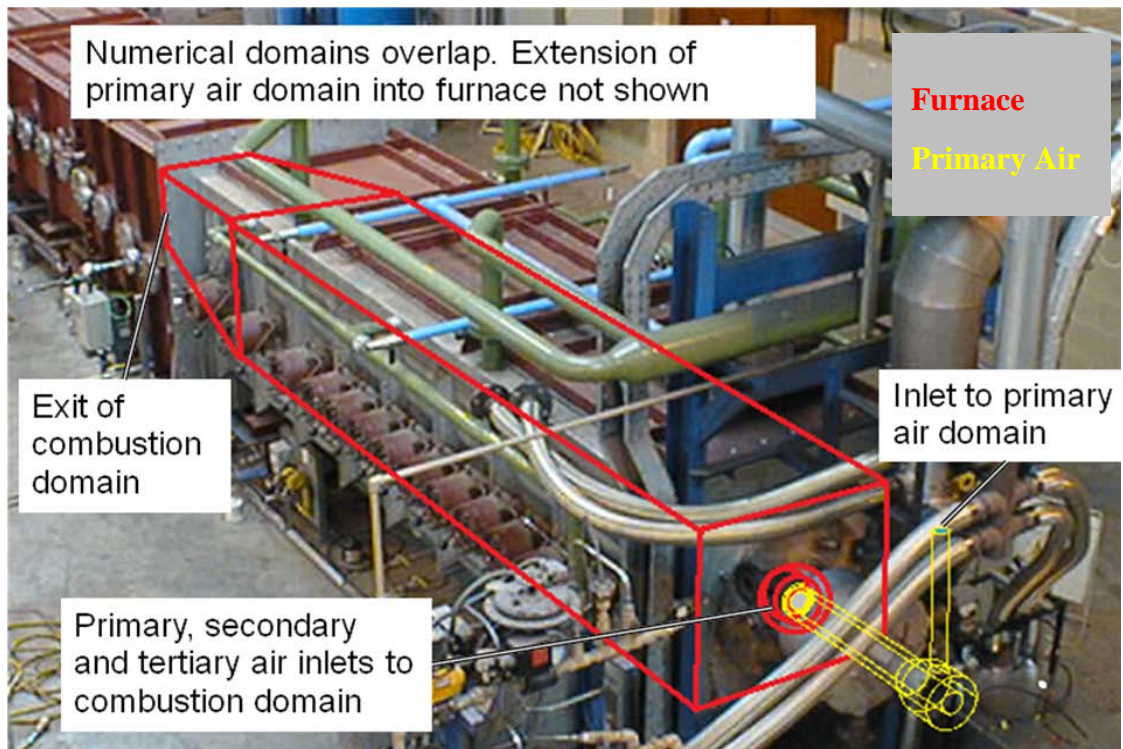


Figure 5.1 Photograph of the RWE Combustion Test Facility with numerical domains overlaid.

Shows the furnace outlined in red and the burner and air supply pipe in yellow, respectively representing the regions of dominance between combustion and particle physics.

annulus (the burner mouth), this has a slight throat reducing the outer diameter. The flame holder is L shaped, in cross-section (tangential to the pipe), with the wall between the primary and secondary air annuli meeting the centre of the bottom of the L and the back corner and edge obstructing the secondary air. A slight extension beyond the flame holder into the furnace is employed in the computational domain, shown in Figure 5.2(b), in order to remove inaccuracies that would be introduced into the computation of the flow at the burner mouth, from an immediate boundary condition (BC) of somewhat arbitrary pressure. Due to the difference in the coal and biomass particles in terms of their density, size and shape, and with a radial feed of the fuel particles, an uneven distribution of particle mass flow in the burner mouth might be anticipated.

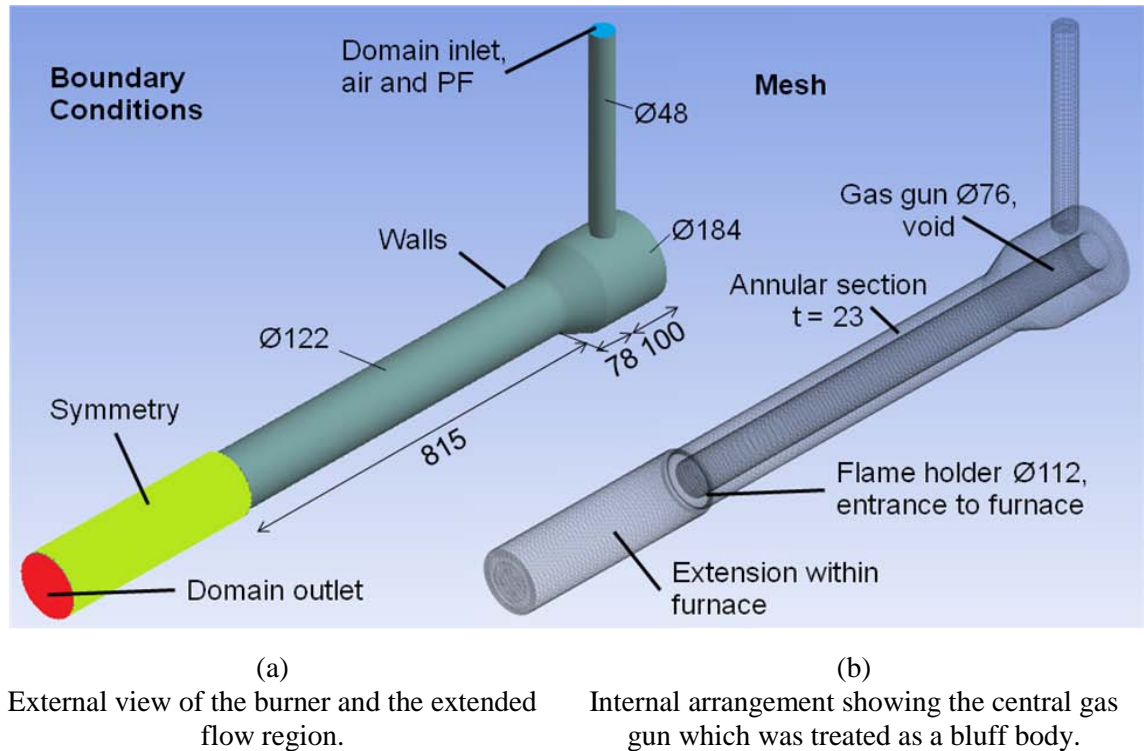


Figure 5.2 The mesh arrangement of the computational domain.

5.1.2 The Particle Flow Case Investigated

Coal particle shapes are virtually spherical with well defined size distributions. Biomass particles usually have a larger mean diameter, range of sizes and a lower density than coal, which affects their inertial behaviour. Irregularly shaped biomass particles present significant deviation from isometric shape and this results in a variable projected area depending on the orientation of the particle. These differences may induce segregation of the two dispersed phases in the burner feed tube.

The coal and biomass used in this chapter were a typical bituminous coal (Russian coal) and milled wood that are frequently used for co-firing in power stations. The primary air supply carries approximately 55% coal in mass load, corresponding to 0.04% by volume. When co-firing at 13%th biomass these will rise to 65% fuel mass load and 0.07% by volume. Although globally dilute, locally the volume fraction might be significantly greater and therefore the inter-particle collisions of importance.

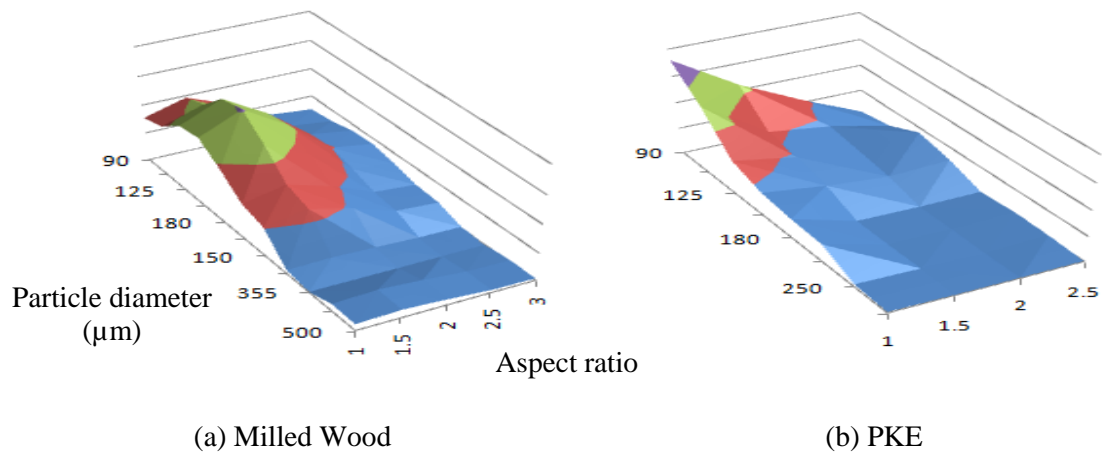


Figure 5.3 Particle normalised volume fraction against size and aspect ratio.

In the calculations, it is assumed that the fluid is incompressible air at 80°C with a mass flow rate $\dot{m}_f = 0.04\text{kgs}^{-1}$ to give a nominal air velocity of 6ms^{-1} in the primary air annulus. The coal and biomass fuel flow rates are $\dot{m}_c = 0.021\text{kgs}^{-1}$ and $\dot{m}_b = 0.005\text{kgs}^{-1}$, respectively, totalling 65% mass load. The densities of the coal and biomass considered are $\rho_c = 1300\text{kgm}^{-3}$ (dry) and $\rho_b = 500\text{kgm}^{-3}$ (dry), respectively.

The particle size distribution data for a typical pulverised coal is taken from Ma *et al.* (2009) and Edge *et al.* (2011), and those of milled wood were taken from Gubba *et al.* (2012b) and shown in Figure 5.3(a). For comparison, the particle size and shape distribution of the pulverized Palm Kernel Extruder (PKE) were also shown in Figure 5.3(b). All fuel samples were provided by the RWE. As can be seen in Figure 5.3, biomass particles, i.e. the milled wood and PKE, are significantly larger in size than pulverized coal particles that typically have a mean diameter less than $100\mu\text{m}$. Further, they are non-spherical with a high aspect ratio defined by the largest and smallest dimensions of the particle. Clearly the milled wood particles are larger and more anisotropic compared to the PKE.

5.2 Computational Modelling

The mathematical basis of the particle flow models is given in Chapter 3. In particular, models were developed for implementation in Fluent for non-spherical drag, using Ganser's method, Saffman lift, inter-particle collisions and wall collisions respectively, sections 3.2.3, 3.2.5, 3.2.6 and 3.2.7. Non spherical drag and lift are facilitated by user-defined functions (UDFs). A number of classes of the template for UDFs, known as macros are provided. These give the user access to different Eulerian flow and Lagrangian particle properties and sometimes require an output that will be used directly. The order of the arguments to these functions is strictly defined, see ANSYS (2009b) for more details. For example specific non-spherical drag and lift forces are prescribed to the force balance in the particle trajectory calculations by use of DEFINE_DPM_DRAG and DEFINE_DPM_BODY_FORCE, respectively. Separately, wall collisions are implemented in Fluent through DEFINE_DPM_BC. This UDF handles the wall collision detection, location and wall normal direction for the user but instead of a force acting on the particle the effect is of an impulsive step change in particle velocity. No direct output is used by the macro, these new velocity components are calculated within the UDF and the pre-collision particle velocity overwritten. The implementation of such models, with a pre-defined macro, is relatively straight forward. The stochastic inter-particle collisions method, introduced in section 3.2.6, requires additional steps to be executed within Fluent. These are described in full for a single representative particle class in section 4.3.2 and this section acts as a supplement to the previous discussion, for multiple particle classes. For n representative particle classes the probability of collision, equation [3.53], effectively becomes:

$$P_c = \frac{\pi}{4} \Delta t \sum_{j=1}^n (d_s + d_{oj})^2 |\vec{u}_s - \vec{u}_{oj}| n_{pj} \quad [5.1]$$

where the subscript $_j$ denotes the particle class number of the collision object. The uniform random number is generated and repetitively compared to the cumulative addition of the probability from the j^{th} particle class. If the probability of the cumulative total exceeds the random number during comparison, further particle class probability

calculations cease. At this point the particle class with which the collision has randomly been determined to occur is the j^{th} . The Eulerian local particle properties could be determined in an almost identical manner as before, equations [4.1]-[4.6]. However, the method is also extended to cover a range of particle densities. Therefore the local particle mass-density of all classes must also be recorded, as given by:

$$\rho_{\text{mass}j,k} = \sum_{i(j)} \dot{m}_{pi} D_{i,k} \rho_{pi} \quad [5.2]$$

where $\rho_{\text{mass}j,k}$ [kg^2m^{-3}], is the mass-density of class j in cell k . Sigma- $i(j)$ denotes summing streams i that are within the class j .

Also, as seen in equation [5.2], multiple local particle size classes require each property, equations [4.1]-[4.3] and [5.2], to be solved for the j particle classes. This is facilitated by appending a subscript j to all terms. For brevity, as each stream can only be in a single particle class determined by size and density, each cell property (for a particular class and cell j,k) is found by summing over the streams i within the class j and the notation of Sigma- $i(j)$ is used.

After summation the averaged density of class j in cell k , $\rho_{p0j,k}$ [kgm^{-3}] is found:

$$\rho_{p0j,k} = \frac{\rho_{\text{mass}j,k}}{m_{\text{mass}j,k}} \quad [5.3]$$

This is used to determine the local particle diameter of class j in cell k , $d_{p0j,k}$ [m]:

$$d_{p0j,k} = \sqrt[3]{\frac{6}{\pi} \frac{m_{\text{mass}j,k}}{\rho_{p0j,k} P_{\text{cell}j,k}}} \quad [5.4]$$

which replaces equation [4.5].

The computational method for updating the Eulerian properties has been described in section 4.3.2. As the local particle density is also required in this investigation, in this case the “unseen” accumulative variables, updated each time a stream exits a cell, are the population of particles in the cell, p_{cell} , the static mass of particles in the cell, m_{mass} [kg], the sum-product of mass and velocity, \vec{u}_{mass} [kgms^{-1}], and the sum-product of mass-density [kg^2m^{-3}], as given by equations [4.1]-[4.3] and [5.2], respectively. The “seen” variables, calculated once (in each cell and for each local particle class) after the

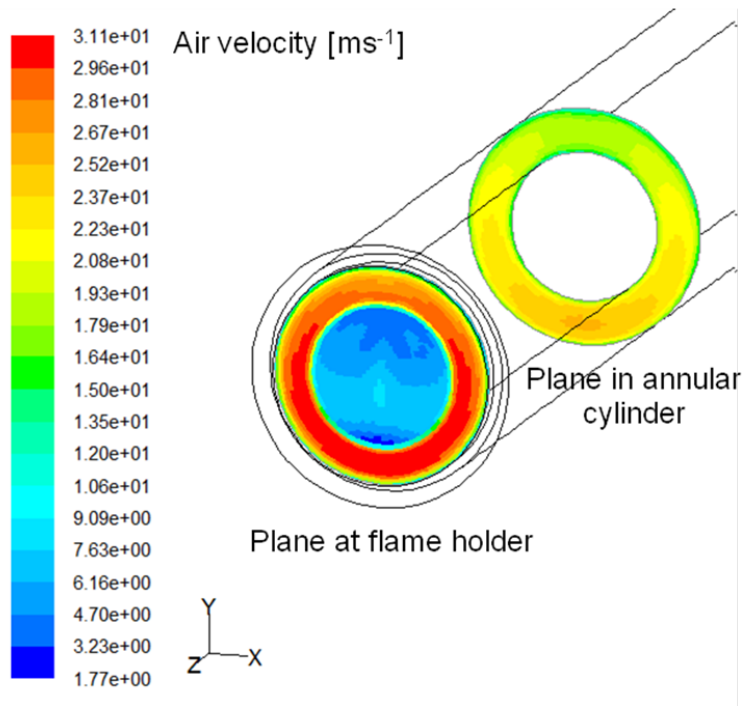


Figure 5.4 Contours of the computed magnitudes of the air velocity.

In the planes of the burner mouth of the primary air tube (lower and to the left) and a typical cross-section within the annulus (higher and to the right), (ms^{-1}).

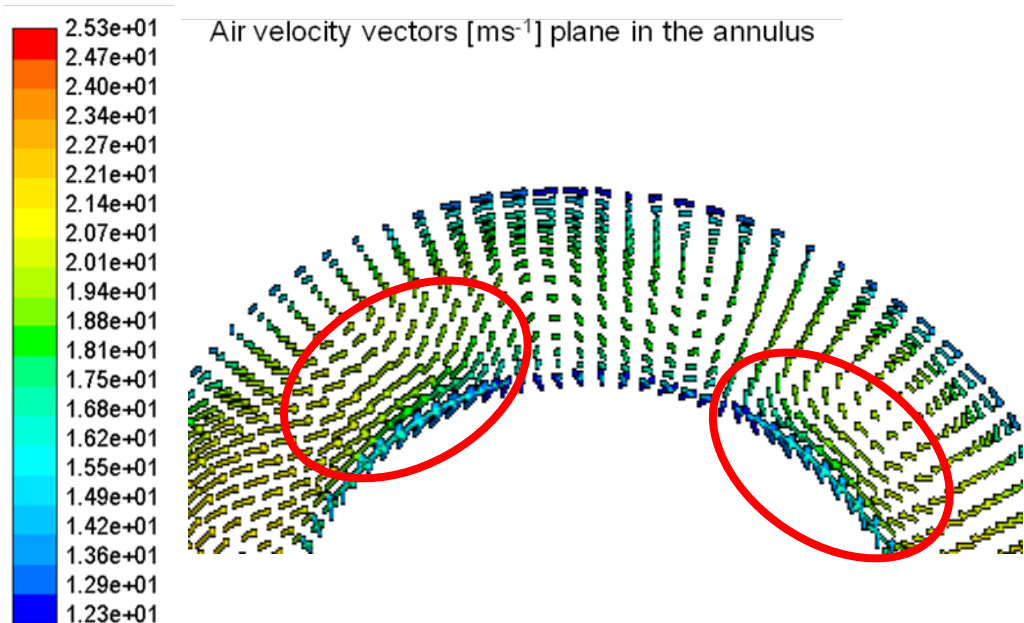


Figure 5.5 Predicted secondary air flow.

Zoomed area at the top of the representative annular plane depicted in Figure 5.4. Note the converging tangential fluid velocities at the inner wall of the annular tube.

full set of trajectory calculations of the particle streams, are the concentration of particles, c_p [m^{-3}], the local particle velocity, \vec{u}_{p0} [ms^{-1}], the local particle density, ρ_{p0} [kgm^{-3}], and local particle diameter, d_{p0} [m], given by equations [4.4], [4.6] and [5.3]-[5.4].

5.3 Computed Results and Discussions

Using the boundary conditions (BCs) and models outlined in sections 5.1 and 5.2, results for particle velocities, particle number concentrations and particle mass fluxes inside the burner tube, as well as at the burner mouth, were obtained for blends of coal/milled wood. The computed magnitudes of the air velocity in two lateral planes, these being a typical cross-section within the annulus and at the burner mouth, the location at which the flame holder sits, are shown in Figure 5.4. The average air velocity at the burner mouth is slightly higher than in the tube and this is due to the reduction in the cross-sectional area of the flame holder. Further, a slightly higher velocity is observed near to the bottom regions of the tube and this is because of the radial injection of the air from the top of the tube. This creates strong secondary flows in the tube, as shown in Figure 5.5, which have a strong influence on the motion of the fine and light particles. The contours for the computed velocity magnitudes of the coal and biomass particles at the same two planes as the air velocities in Figures 5.4, are given in Figure 5.6. It is observed that, caused by the air flow (Figure 5.4), a clear difference in velocity distribution exists inside the primary air tube where the particles flow faster near to the bottom wall and slower above the inner wall. Because of the particle mixing, inter-collision and interaction with the tube surface in particular the flame holder, the particle velocity distribution at the burner mouth is more uniform than it is inside the tube. Apparently the influences of the tube surface and the flame holder are stronger lower in the tube. In general, the velocity of the solid particles is lower than that of the carrying air.

Of greater significance than the particle collisions on solid surfaces, the secondary flows shown in Figure 5.5 have an impact on the movement and distribution of the particles inside the air annulus. Figure 5.7 shows that higher number concentrations of both coal and biomass particles are present on the top of the inner wall than the bottom

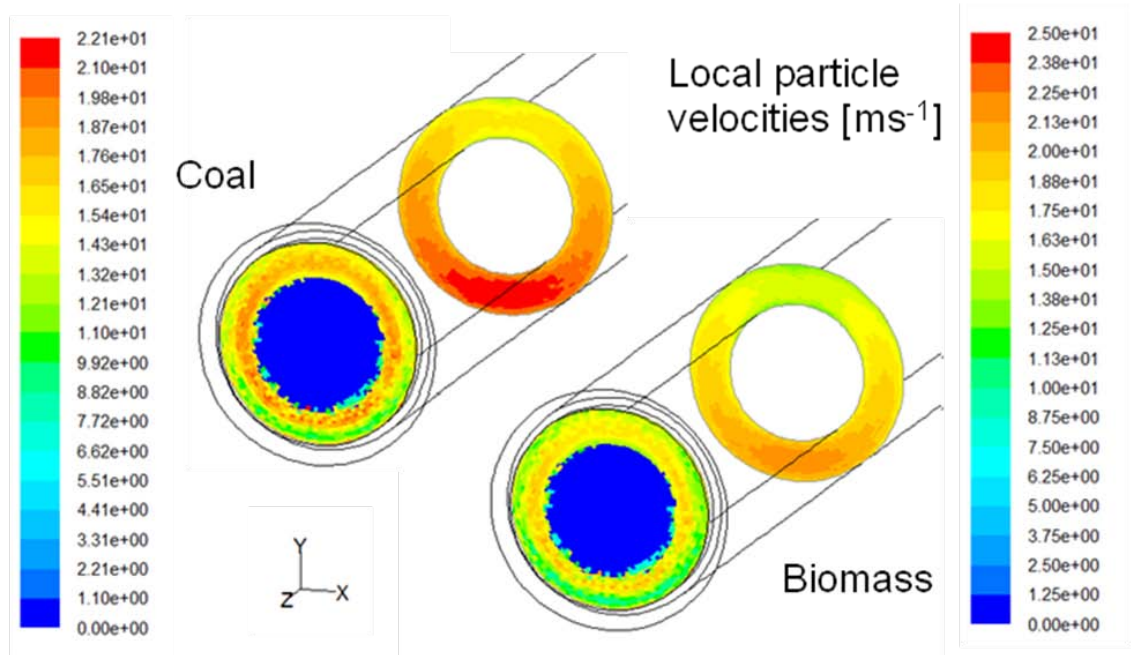


Figure 5.6 Predicted local particle velocities of coal and milled wood.

Lower and to the left is the flame holder and higher and to the right is a representative plane within the annulus.

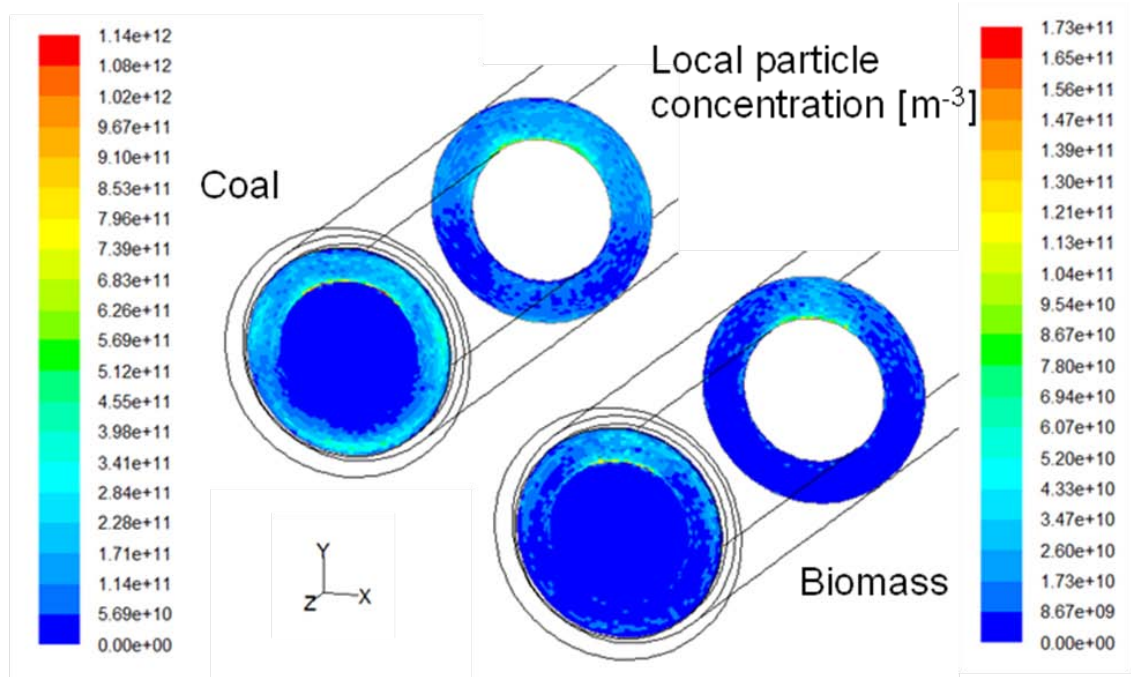
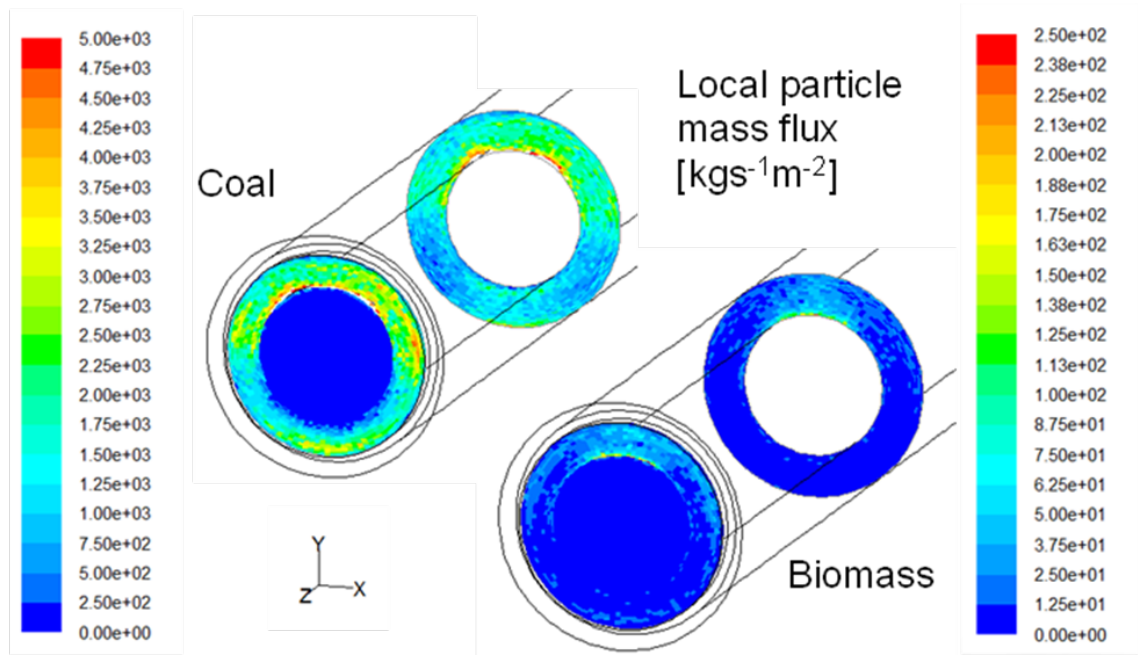


Figure 5.7 Computed local particle number concentrations of coal and milled wood.

Lower and to the left is the flame holder and higher and to the right is a representative plane within the annulus.

of the tube, although this difference in number concentrations is less significant at the burner mouth due to the further mixing taking place due to wall collisions at the flame holder. Further, no clear evidence of stratification of the particles in terms of particle sizes is shown in the calculations. The distribution of the mass flux density of the coal and biomass, as shown in Figure 5.8, are very similar to the number concentration distributions shown in Figure 5.7.

It is clear that there is a substantially uneven distribution of fuel particles in the primary air duct leading to the burner mouth and this is more evident for biomass particles. Further significant mixing takes place in the tube due to secondary flows, particle inter-collisions and interactions with the tube wall. Much stronger mixing would be expected to occur in the combustion chamber meeting the secondary and tertiary air streams. In an actual flame the particles enter a swirling gas flow and the effect of the segregation is reduced. Observation of an actual flame from the same burner does not show preferential flame holding. Indeed the position of the flame is extremely random. An instantaneous image of such a flame is shown in Figure 5.9(a) (Ma *et al.*, 2009). Computed large eddy simulation (LES) flames, Figure 5.9(b) (Edge *et al.*, 2011), assuming uniform particle distribution in the burner also shows a highly fluctuating flame. It is suggested that the magnitude of the intermittency shown in both experiments and the CFD simulated flames disperse the effects of a moderately uneven distribution of the fuel particles investigated in this chapter.



For comparison water would have a mass flux $\approx 2 \times 10^4 \text{ kgs}^{-1} \text{ m}^{-2}$

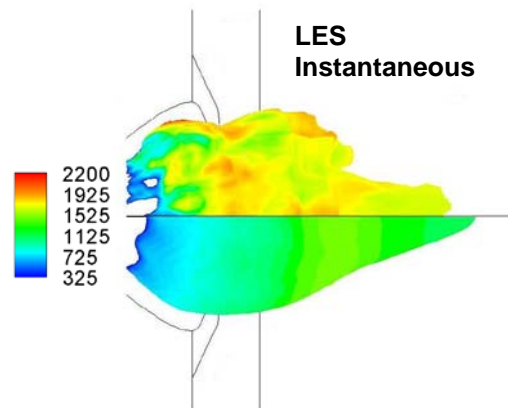
Figure 5.8 Calculated particle mass fluxes of coal and milled wood.

Lower and to the left is the flame holder and higher and to the right is a representative plane within the annulus.



(a)

Still photograph (Ma *et al.*, 2009).



(b)

LES (top) and RANS (bottom) computation of the flame zone (Edge *et al.*, 2011) showing flame intermittency.

Figure 5.9 Flame stabilised on the burner mouth of PF coal/milled wood.

5.4 Chapter Summary

A steady state air, coal and biomass three-phase particulate flow in the primary air tube of a low-NO_x swirl burner was modelled using computational fluid dynamics techniques in order to investigate the distributions of the fuel particles in the burner mouth which may have a significant impact on the flame and combustion of the fuels. The fuel particles are tracked in a Lagrangian frame to obtain Monte Carlo inter-particle collision effects for a co-fired coal/biomass blend.

Substantial variations in the particle distributions were found in the primary air tube and at the burner mouth entering the furnace. Although the two particulate phases were concentrated in the same vicinity, the effect is greater for the biomass. A significant mixing and redistribution of the fuel particles takes place in the tube due to secondary air flows, inter-particle collisions and interactions with the tube walls and this leads to a more even distribution of particles at the exit of the burner. It is believed that the substantially stronger mixing that takes place in the near burner regions with the swirling secondary and tertiary air streams, and the highly unsteady combustion flames would outweigh the effect of the non-uniformity in the particle distribution at the burner mouth. However, it is worth monitoring any possible existence of highly stratified fuel flows that may impact on the ignition and flame stability of the co-firing flame.

Chapter 6

Co-firing Chinese Straw with Coal in a 300MW_e Tangentially Fired Pulverised Fuel Furnace

6.1 Introduction

Computational fluid dynamics (CFD) becomes a truly powerful tool when it can be used to predict the behaviour of a dynamic system without the need for expensive experimental validation. With this level of confidence in the modelling, a great number of numerical test cases may be performed, at low cost, in order to select only those physical experiments that are vital. The most significant regime for these numerical experiments to test is at full scale, where the physical experiments are most challenging, and the most beneficial corollary is the full access to virtual data from regions where physical measurements may be impossible.

In this chapter, CFD combustion modelling, using parallel ANSYS Fluent v12.1, is performed to simulate three Chinese experimental cases of bituminous coal and biomass co-firing (that shall be referred to as Cases 0, 1 and 2, respectively, corresponding to 0%, 6% and 12% straw co-firing thermal loads) in a 300MW_e tangentially fired pulverised fuel (PF) furnace presented in Wang *et al.* (2011). Experimental measurements were undertaken by Dr Xuebin Wang and Prof Houzhang Tan, of Xi'an Jiaotong University, Shaanxi, China, on a 300MW_e unit at the Baoji Power station, Shaanxi, China.

The purpose of this study is to test the current modelling capabilities so that these tools are available to operators considering particular aspects of a retrofit to existing coal boilers adding the capability of co-firing. The following sections detail the furnace, which was designed for coal combustion only; the measured values and assumptions used in the modelling parameters for the experimental cases; the model selection and simulation procedure; and give a summary.

The computational modelling of full scale coal power stations, many of a similar design to that of the present study, have enjoyed numerous investigations (Backreedy *et*

al., 2005, Belosevic, 2008, Díez *et al.*, 2008, Choi and Kim, 2009, and Jones *et al.*, 2010). However, there is greater difficulty in finding such large scale experimental investigations for co-firing. A small scale test furnace employing a single low NO_x swirl burner, was investigated under co-firing conditions by Damstedt *et al.* (2007). Battista *et al.* (2000) have presented experimental measurements from a 150MW_e tangentially fired pulverised coal power unit in the USA, originally built in the 1950s, which is co-fired with up to 14% sawdust, on a thermal basis, using the “dedicated burner” technique (section 1.1). Also, Wang *et al.* (2011) have considered the effect of biomass on the coal feeding system by selecting separate injections to a set of dedicated upstream burners, this is the basis of the current chapter. Studies predict that co-firing with biomass would not reduce the fuel feed capacity and offers significant NO_x reductions with a promising economy (Battista *et al.*, 2000, Sami *et al.*, 2000, Damstedt *et al.*, 2007, Wang *et al.*, 2011). Furthermore the economic capability would increase for larger and more efficient units, provided that the biomass can be supplied and the heat transfer in the boiler is not reduced.

6.2 Experimental Facility and Fuel Properties

The experiments were performed on a 300MW_e furnace at Baoji power station, Shaanxi, China. This is a pulverised coal boiler designed to burn local bituminous Huating coal. The furnace is a wet bottom suspended π type, which is four corner fired with a cross-section $\approx 14 \times 15$ m and height of ≈ 55 m. Point heights are quoted using the boiler hall floor as datum. This means that the bottom of the ash pan is at a height of 6.9m and the platen superheaters are suspended from the ceiling at a height of 62m. The arrangement of the inlets at each corner is geometrically identical and also, under the operational conditions in the experimental work, the mass flow rates of the air and fuel are unchanged between the corners for any given case. However, the mass flow rates at the inlets differ at the individual levels and between the cases investigated. There are three distinct banks of inlets, as shown in Figure 6.1(a), each consisting of a twin primary air braced and interspaced by three secondary air, with equal-air registration, taking an alternating AA, A, AB, B, BB form where the single letters indicate primary

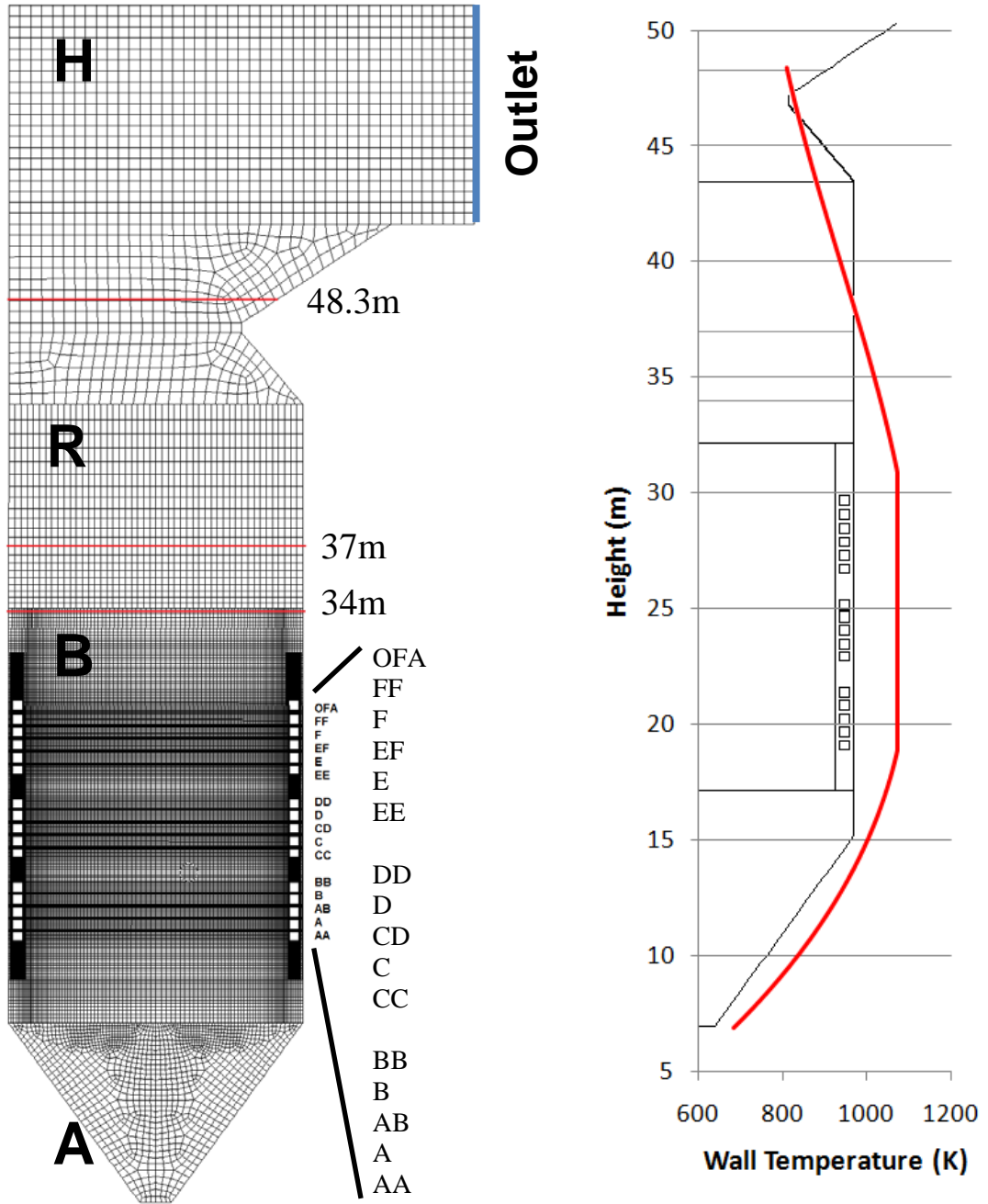


Figure 6.1 Furnace mesh details and temperature boundary conditions.

(a)
Measurement locations, inlet levels, outlet
and mesh regions:
H, hood; R, recirculation;
B, burner; A, ashpan shown on the mesh.

(b)
Wall temperature boundary condition as a
function of height.

Table 6.1 Test conditions from baseline coal and coal/biomass co-firing.

Case	Baseline Case 0	Case 1	Case 2
Total output power (MW_{th})	629	652	660
Coal mass flow rate (kgs^{-1})	31.94	31.11	29.44
Straw mass flow rate (kgs^{-1})	0.00	3.33	6.67
Percentage co-fire thermal load	0.00%	6.21%	12.35%
Excess oxygen (dry vol.)	3.0%	4.1%	3.7%

air and double letters the secondary air. The highest bank of these five inlets also includes a close coupled over fire air (OFA) so this results in 16 levels per corner totalling 64 inlets. The inlets are 635mm wide and 350-440mm in height. No more than 56 inlets are used simultaneously during the course of the experimental investigations. All the inlets are angled to give a positive rotation of the flow about the upwards direction, except the OFA which fires in the opposite direction. There are slight differences between the two pairs of diametrically opposed corners, but the radii of the swirls within the fireball are approximately 0.5m for the primary air and 3m for the secondary air and OFA. Further, no burner tilt is employed.

The highest level of primary air inlets (F), their mills, feeding system and other supplying upstream equipment were adopted for straw pellets, thus allowing direct co-firing with separate injection, in which the coal and the biomass only meet within the furnace during combustion. The straw was pelletised to alleviate the problems of transporting and handling fresh biomass. Also the long stalks must be chopped to yield particles of a suitable size for PF combustion, which the existing ball mills cannot accomplish. Instead, the large pellets, of 30mm diameter and up to 100mm in length, are ground in the mills like lump coal. Three tests were undertaken and are labelled Cases 0, 1 and 2. During the baseline, Case 0, the biomass mills and inlets were shut down. For Cases 1 and 2 these systems processed 3.33 or 6.67 kgs^{-1} of straw pellets (12 or 24 th^{-1}), respectively. Similar systems for different primary air levels handled up to 9 kgs^{-1} of coal. An overview of the test cases investigated is provided in Table 6.1. The

Table 6.2 Fuel combustion properties.

	Proximate % AR				Ultimate % DAF				HCV (MJkg ⁻¹)	Volatile yield
	FC	VM	A	M	C	H	O	N		
Huating Coal	41.6	25.1	17.3	16.0	79.5	4.6	15.1	0.8	20.65	1.6
Straw	12.2	46.9	28.3	12.6	60.3	3.0	34.1	2.6	13.15	1.1

furnace temperature measurements were made, by an infrared gun, at three different height locations, namely 34, 37 and 48.3m above the boiler hall floor – marked as horizontal lines on Figure 6.1. The NO measurements were taken by probe using a standard analyser, the Testo 350, to deduce NO_x. The concentration of O₂ in a dried flue gas sample is used to measure the excess oxygen. In addition, the unburnt carbon (UBC) in ash was inferred from the mass loss of collected fly ash during sustained heating in an oven.

The major combustion parameters, namely the proximate and ultimate analyses, on as received (AR) and dry ash-free (DAF) bases, respectively, and higher heating values (Table 6.2), along with coal particle sizes from sieving and milled straw particles from optical analysis (Table 6.3), are provided by Wang *et al.* (2011) using standard laboratory tests. The high temperature volatile yield employed for the coal is typical for a bituminous coal, for the straw the value is estimated from a study by Saddawi *et al.* (2011) which found that the char accounted for $\approx 13\%$ of the DAF particle after rapid devolatilisation. Logarithmic Rosin-Rammler particle size distributions of ten divisions were applied using the sieve and optical measurements for the milled coal and straw pellets, respectively. As the same milling equipment was used to pulverise the straw pellets in both co-firing cases, despite the mass flow rate doubling, the milling efficiency was decreased resulting in larger straw particle sizes in Case 2 relative to Case 1. This fact is related by the mean diameter used in the Rosin-Rammler size distribution in Table 6.3. Temperature measurements of the furnace wall were not performed. Therefore a height dependent function for the wall thermal BC was derived by normalising the cubic function of the furnace temperature against height, based on

Table 6.3 Particle size properties.

Rosin-Rammler Parameters		Diameters (μm)			Spread parameter
		Min	Mean	Max	
Huating Coal	All cases	50	70	300	1.2
Straw (12th ⁻¹)	Case 1	50	100	1500	1.2
Straw (24th ⁻¹)	Case 2	50	450	1500	1.3

the three experimental measurements from Case 0 and assuming that at the ash pan the temperature is 1000°C. This curve is then applied between the minimum wall temperature of 410°C (steam saturation temperature + 50K temperature lag within the wall) at the wall is made to correspond to a height of 6.9m (ashpan) and the maximum expected slag temperature of 800°C forms a plateau of the highest wall temperature in the near-burner region, of between about 17 and 30m, see Figure 6.1(b). The wall emissivity is taken to be 0.5 and the results obtained indicate that this is reasonable. Perfectly elastic wall collisions are assumed, as particles generally have very low Stokes numbers and follow the gas, or alternatively they are governed by gravimetric forces, therefore the simulation is expected to be insensitive to the collision method used.

The nitrogen conversion fraction, presented in Table 6.4, is the proportion of the total mass of fuel-N active in NO_x formation during the char and the volatile combustion. The ratios, in Table 6.4, describe the relative apportionment of the nitrogen, from the char or the volatiles, in the respective direct product species during combustion. The N-species are changed by subsequent reactions so these values do not represent the final forms of nitrogen species that exit from the numerical domain. The difference between a physical system and a numerical domain is discussed in section 3.1.1, in this instance the location at which the NO measurements would have been taken is not included in the numerical domain and instead the computational measurement is performed at the exit of the calculation space, the surface labelled “Outlet” in Figure 6.1. The rationale behind the grid formation is presented in detail in the following section 6.3.

Table 6.4 Fuel NO_x properties.

	Coal		Straw	
	Char	Volatile	Char	Volatile
Conversion fraction	0.543	0.282	0.090	0.910
NO ratio	1	0.941	1	0.000
HCN ratio	0	0.002	0	0.250
NH ₃ ratio	0	0.057	0	0.750

6.3 Numerical Grid

Much effort was expended in developing a suitable grid structure, representing the spatial discretisation of the numerical domain for use in the CFD calculations. The meshes were created in Gambit 2.4. Calculations were initially performed on 3.0M cell meshes with conformal tetrahedral cell regions between the varying levels of cell sizes. However, the level of control in the tetrahedron growth and positioning during the meshing was found to be insufficient resulting in rogue, almost two-dimensional, cells, that could not be eliminated, and led to divergence through numerical errors in their face fluxes. There is a trade off in the time to generate a good quality grid, having a smooth transition in cell sizes and shape, and the appropriate efficiency, placement of greater cell density in vital regions and the relaxing of refinement in less important regions, against the time saved during the simulation. Initially the extents of the numerical domain, that is to be meshed, must be decided. As identified in section 3.1.1 the true system is affected by the atmosphere, being open at the fuel hopper and exhaust ends. The physical topology of the grid, shown in Figure 6.1, was selected to coincide with the known dimensions of the furnace design and the dynamic region for reaction of the fuels, representing the upwards pass of the π boiler and neglecting the feedpipes and superheaters. Inlets are positioned on the chamfered corners of the burner region and the outlet is labelled in Figure 6.1. The second saving was to modify the very slight off-chamfer angles of the corner walls in the burner region to 45°, allowing only a quarter of the region to be created, then copied and mirrored. Fuel particle trajectory

calculations use these surfaces for the location of injection but the direction of injection is independent. The simulations were performed on a 4.3M cell mesh, depicted in Figure 6.1, encompassing $1.12 \times 10^4 \text{m}^3$. Interfaces are set up between the regions varying different levels of refinement, the mean cell-edge lengths being 0.10, 0.20, 0.34 and 0.50m in the burner, ashpan, recirculation and furnace hood regions, respectively. The volumes of the cells adjacent to the walls are similar to their neighbouring cells as meshing the laminar shear layer would result in a very high number of cells. The flow near the walls is not significant compared to the combustion so the shear is handled by a wall model rather than simulated. It is expected that the wall-turbulence and convective heat transfer effects are of less significance compared to combustion-turbulence and radiative heat transfer in hot combusting flows. Therefore refinement of the grid was focused on the flame locations. To improve the cell efficiency, a circular core to the burner region was created slightly larger than the nominal fireball, in which the coal combustion is known to take place in the furnace considered, in addition the area was sectioned by a path leading from the burner inlet towards the ball of flame, these can be seen in Figure 6.2. At the injection faces and within the core a greater cell refinement is used than in the rest of the burner region. Square paving was enforced across the cross-section of the burner regions and extruded in hexahedral layers in the vertical direction of the furnace, into the page as presented in Figure 6.2. The other regions of the mesh, named the hood, recirculation and ashpan are of simple shape and extruded laterally, into the page as presented in Figure 6.1, with hexahedral cells.

The burner region, where there is the highest cell refinement, was extended, in the 4.3M compared to the 3.0M meshes, to place the non-conformal interfaces away from the region in which reactions will occur. This is why the number of cells increased despite replacing tetrahedrons with hexahedrons, which have a greater equal-cell-length volume and therefore require a lower number to mesh the same volume at the same level of refinement. In addition, grid independency was investigated by performing the baseline investigation, coal only Case 0, on 6.2M and 8.4M cell meshes as well as the 4.3M cell mesh. To generate the new meshes the same structure as for 4.3M cells was

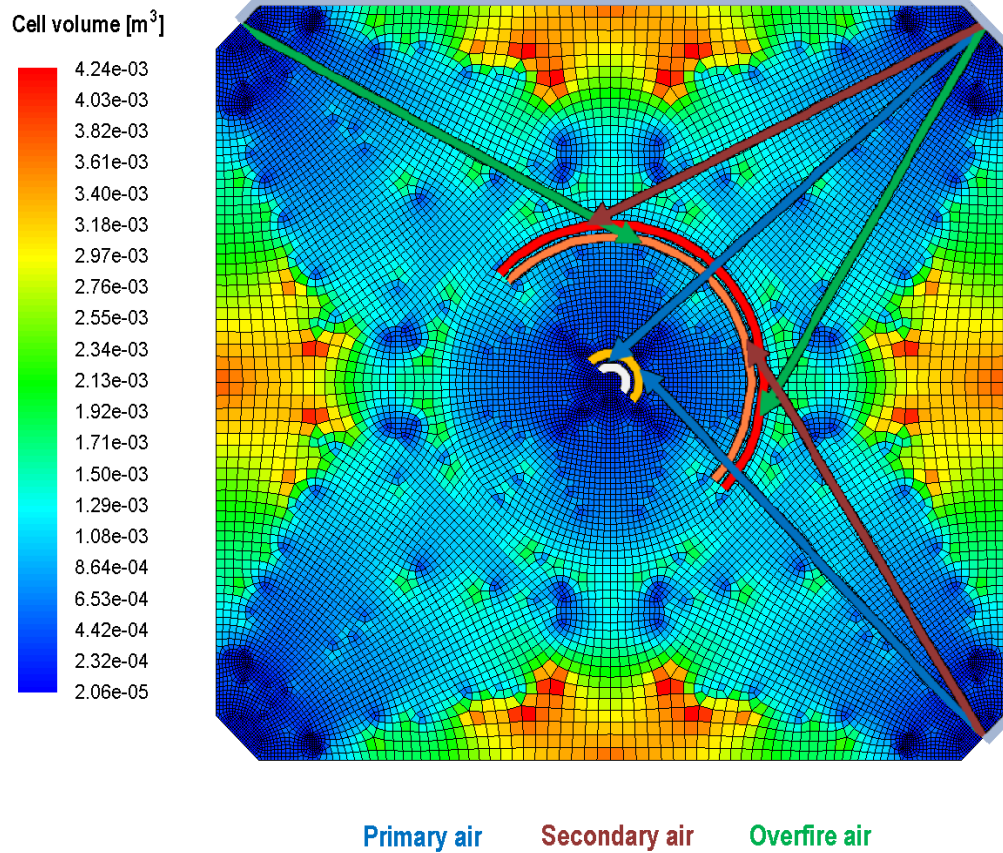


Figure 6.2 **Cross-section of the mesh in the burner region.**

Cells are coloured by cell volume, the upper right half has the particle injection directions of the primary, secondary and overfire air and the circumference of their swirl overlaid.

employed but with the cell length definitions reduced by $\sqrt[3]{1.5}$ and $\sqrt[3]{2}$ to give approximately one and a half and double the number of cells, respectively.

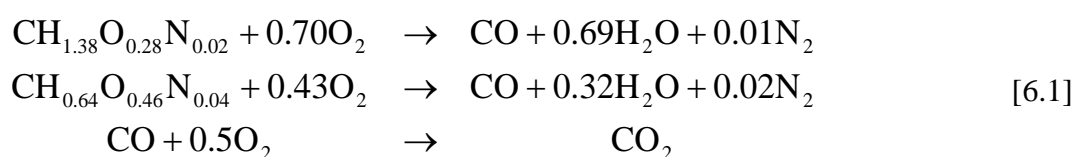
6.4 Numerical Models

The continuous and particulate phases are solved using the ANSYS Fluent V12.1 software on 8-20 parallel processors, depending upon the size of the grid and the number of particle streams, with 4GB RAM on a Sun Grid Linux cluster. Steady Reynolds-averaged Navier-Stokes (RANS) calculations were performed using the realisable $k-\varepsilon$ model (ANSYS, 2009c) with scalable wall functions to solve the continuous phase turbulence transport. Radiation is modelled by the grey discrete ordinate method, with 3 angular divisions totalling 72 discrete ray directions. The coal and biomass particles are tracked by a steady Lagrangian approach in the 3D domain, assuming that all the particles are of a spherical shape. Moisture evaporation, devolatilisation and char combustion are sequentially modelled. During evaporation and devolatilisation, the mass of the particle and, respectively, the fractions of moisture and volatiles in the particle are reduced and sources of each of the same are added to the continuous phase. During char combustion, the majority of fixed carbon is lost from the particles with the ash and the UBC remaining, this results in an O_2 sink and CO source in the numerical cell. Descriptions of the mathematical models employed during combustion are given in sections 3.1.3 and 3.3. A first-order, single step Arrhenius equation is used to determine the separate rates of devolatilisation of the coal and biomass particles; and the resultant volatile gas consists of the yield of gas and tar. The rate constants for a typical bituminous coal and measured pulverised wood, published by Ma *et al.* (2007), are used in the present chapter as presented in Table 6.5. The use of these constants is described in section 3.3.4, and presented in equation [3.95]. The rates

Table 6.5 Fuel combustion properties.

Fuel	Devolatilisation constant	
	Pre-exponential, A_1 , [s ⁻¹]	Activation energy, E_1 , [kJ.mol ⁻¹]
Coal	4.2×10^{14}	230
Straw	6.0×10^{13}	250

of coal and wood devolatilisation are similar to the bituminous coal and the wheat straw values (Williams *et al.*, 2001), respectively, although at high heating rates in real furnaces, $\approx 10^5 \text{ Ks}^{-1}$, the constants used to describe the rate of devolatilisation are less critical (Saddawi *et al.*, 2010). The wood and straw particles from the different studies were identified as having a similar size distribution. The gaseous reaction rates of the oxidation of the volatile components discharged from the solid fuels are controlled by turbulent mixing using the eddy dissipation concept. There are two initial first steps and a common CO oxidation second step, as summarised here:



Note that this has the same form as equation [3.11], but containing chemical formulae for the volatile pseudo-species (first “CHON” terms in the first two lines) and the constants for the stoichiometric coefficients.

Char combustion is modelled as a pure carbon one-step oxidation reaction. For both fuels this is limited by both the gaseous oxygen diffusion and the intrinsic reactivity of the char based on the method of Smith (1982) and using the suggested reaction properties supplied by a comprehensive study of a range of bituminous coals (Backreedy *et al.*, 2006, and Darvell *et al.*, 2010). In general, biomass char combustion is modelled as limited by the diffusion of locally depleted O_2 to the surface of the char particles, which will be much larger than those of coal (Gera *et al.*, 2001). Also the intrinsic reactivity of biomass will remain greater than that of coal (Wornat *et al.*, 1995, Gera *et al.*, 2001, Backreedy *et al.*, 2006, and Darvell *et al.*, 2010). In this chapter the straw char has been treated using the Smith model but increasing the suggested pre-exponential constant to yield a twofold increase in the reaction rate (Ma *et al.*, 2007).

The NO_x formation is predicted by post-processing using models described by Backreedy *et al.* (2006). The key sources of NO_x for solid fuel combustion at high temperatures are, in order, fuel-N and thermal-N. It has been found that the biomass chars retain a greater proportion of the original fuel-N than those of coal (Wornat *et al.*, 1995), although Glarborg *et al.* (2003) suggest that this trend is reversed at furnace temperatures. The total fuel-N is known from the ultimate analyses. The yields of the

intermediate products (NO, HCN and NH₃), from both char and volatiles, were predicted using the functional group-depolymerisation vaporisation cross-linking (FG-DVC) model for coal at the initial temperature, $T_0 = 1273\text{K}$, and heating rate, $\dot{T} = 10^5 \text{Ks}^{-1}$ by Dr Maryam Gharebaghi. Lower rank coals, which might be extended to “unranked” biomass, and larger particles tend to promote the conversion of fuel-N to NH₃ instead of HCN (Glarborg *et al.*, 2003) therefore the same effect is expected comparing the straw to the coal. The NO_x parameters for biomass are provided by Darvell *et al.* (2010) the intermediate species proportions are based on the final NO attributable to each rather than their immediate fractions. Co-firing NO_x concentration was not found to be highly sensitive to these values and the full scale furnace in the current investigation has much larger residence times than the combustion test furnace (CTF) used therein. A fuel-NO_x prediction is necessarily strongly dependent upon the fuel parameters supplied to the model, presented in section 6.2. Due to the low nitrogen concentrations, the fuel-N takes no part in the combustion. Instead, during post-processing it simply enters the gaseous domain as the pre-determined intermediate species at the rate of combustion of its source (the volatile or char). For the thermal NO_x, O radicals are predicted based on equilibrium calculations. The Zeldovich mechanism describes their interactions in the competing rate equations given here:



where the rate constants are solved using the Hanson and Salimian method (ANSYS, 2009c).

6.5 Results

A comparison of the experimental data and numerical predictions is given in Table 6.6. The disparity between the experimental and numerical values for temperatures, at the same measurement location, and the O₂ and NO_x concentrations at the exit from the domain were less than 5% in all cases. That a stable flame is found in the simulations is proved by the good agreement in the predicted excess oxygen to the nominal value used in each experimental case. Sensible estimates of the undetermined wall conditions, particularly radiative, were of supreme importance in producing quantitative predictions. As might be expected, initial adiabatic or uniform temperature wall boundary conditions were found to yield unreasonable results, furthermore applying a constant heat flux, which could be inferred from the expected power in raising the steam, proved to be instable during the radiation calculations. The thermal results follow the trend of reduced downstream temperatures comparing a co-fire to a coal flame. A continued decrease in temperature from an extended proportion of biomass fuel would be expected, however an increase is observed, albeit negligible at <10K, in the experimental values. The source of this unexpected result is probably due to the tolerances involved in ascribing a measured value to the instantaneous fluctuating temperatures and powers. Figure 6.3 presents temperature contours at the central

Table 6.6 Comparison of experimental data and numerical predictions.

Results		Case 0		Case 1		Case 2	
		Exp	Num	Exp	Num	Exp	Num
Temperature (K)	34.0	1621±25	1620	1593±25	1535	1598±25	1530
at various furnace heights*	37.0	1573±25	1545	1551±25	1490	1559±25	1485
	48.3	1388±25	1315	1378±25	1350	1381±25	1350
Excess oxygen (dry, vol.)		3.0%	3.0%	4.1%	4.0%	3.7%	3.7%
UBC in ash (mass)		0.18%	2.08%	0.47%	0.00%	0.52%	0.00%
NO _x (dry, ppm)		242	273	222	189	214	185

*The listed heights include a 6.9m displacement of the bottom of the numerical domain above the ground, therefore height 48.3m is actually ≈ 13m from the furnace ceiling).

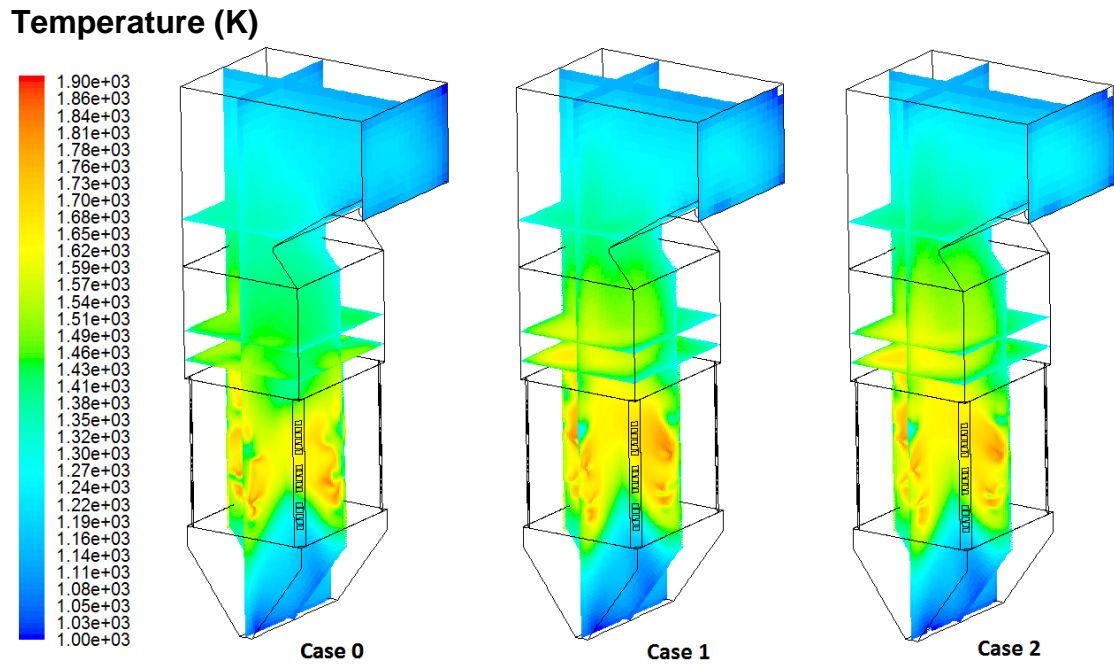


Figure 6.3 Calculated temperatures at central planes, measurement planes and outlet.

vertical planes and outlet as well as the three horizontal measurement planes at 34, 37 and 48.3m heights for all three cases.

Figure 6.4(a) shows the average temperatures at the measurement planes seen in Figure 6.3 against their heights and the linear response. Figure 6.4(b) presents comparison of the NO_x results and predictions, with a clear positive qualitative trend. The remaining experimental measurements, to be used as a yardstick to gauge the numerical results, are much more challenging. This is because the precise mass of the UBC in flyash and concentrations of NO_x are particularly dependent upon the less definite fuel properties (e.g. specific internal surface area), the physical sizes and shapes of the fuel particles and their residence histories within the furnace. In addition to these points, the temporal steadiness and necessary chemical truncation employed in the calculations have greater impact upon these more complex and sensitive predictions. Despite the challenges a positive match of predictions of NO_x emissions to the experiments is observed. Although over predicted across-the-board, the trend of higher biomass loading and lower NO_x has been reproduced and the relative difference

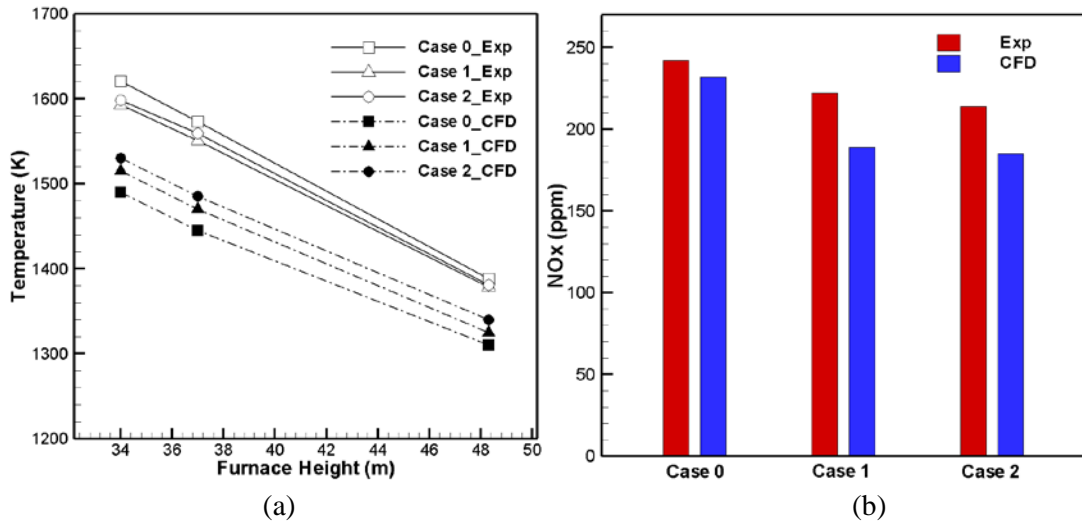


Figure 6.4 Quantitative evaluation

(a) Temperature and (b) NO_x predictions compared to experimental results

between the experimental data and the predictions is reasonable. Thermal-NO_x would self-evidently be reduced by the lower temperatures expected due to the decreased specific energy of the biomass. However, this picture is complicated, considering the full nitrogen path, by the prediction of localised hot-spots during co-firing due to the very rapid volatile release from biomass particles. Biomass contains shorter chain hydrocarbon species which are seen to dissociate at lower temperatures than coals, as well as a decreased specific carbon content. Approximately 80% of the DAF biomass mass is expected to be released as volatiles upon entrance to the hot furnace. Also it is suggested that at rapid heating rates then much of the fuel-N is liberated from the char. So, conversely, biomass may promote rapid thermal and fuel NO_x release but at localised regions and giving maximum high-temperature residence times for conversion of the N-radicals. Related to this argument, the large spherical biomass particles, considered in this chapter, would tend to retard the particle heating up, and therefore devolatilisation, since equal volume isometric shapes present greater minimum lengths to the particle core. Therefore particle shape may play a large role in accurate NO_x predictions. Separate to this discussion, synergistic NO_x reduction during co-firing is reported (Lin *et al.*, 2009), however no chemical pathways particular to the synergism were implemented in these models so this could only be achieved if occurring through

the standard mechanisms. The experiments show markedly lower UBC in flyash compared to supplementary experience (Pedersen *et al.*, 2009, and Jones *et al.*, 2010). An initial explanation might be the high ash content of the fuels diluting the carbon content of the extinct particles. However, Jones *et al.* (2010) report 3-4% UBC in flyash, in a similar furnace, from an Asturian coal whose ash content is 150% that of Huating coal's, on a dry basis. Huating coal also has a greater fraction of fixed carbon, at least in laboratory temperature proximate analysis. At the levels of UBC in flyash, as measured in the experiments (decimals of a percent), the over prediction by 100% in the numerical simulations presented in this chapter is satisfactory. Further work was undertaken examining the sensitivity of the UBC in flyash to parameters in the char combustion model. This showed that the simulation is hypersensitive to the activation energy for the intrinsic combustion model, a 22% reduction in activation energy from 180 to 140MJmol⁻¹ induced a 98% reduction in UBC in flyash.

6.6 Chapter Summary

An elaborate and extensive physical and chemical system has been modelled using CFD under real experimental test case conditions yielding adequate predictions in comparison to the measurements. The study adds to a small pool of data detailing large scale biomass and coal co-firing experiments with simulation. Reasonable numerical results have been obtained at moderate computational expense, which is required, because of the multiplicative nature of the time penalty associated with more intensive models being implemented in conjunction with a complex full scale co-firing system. There is no real distinction between the cases based on temperature, in the experimental data nor the numerical predictions. The temperature differences between the measurement locations in the same case are closely matched. UBC in flyash and NO_x predictions are influenced by the steady state field conditions and fuel properties/size/shape. The lower temperatures predicted, when compared to the experiments, supposing such conditions are prevalent throughout the furnace, would result in decreased emissions of NO_x and also increased UBC in ash through earlier particle extinction, even were perfectly accurate NO_x and char combustion models

employed. As introduced in the previous section 6.5, in real combustion, pockets of lean/rich fuel mixture and high/low temperatures, which cannot be captured under the steady RANS imposition, will have a significant effect upon the particle combustion and NO_x emissions whereas the temperature differences from such pockets will not be frozen in and the difference in concentration of oxygen at the outlet due to varying UBC and NO_x is undetectable. The models for NO_x and UBC in flyash are subject to the measurement of many fuel properties for which values are not routinely established and so the lack of knowledge of the variance of these with fuels and operating temperatures limits their application in purely numerical investigations. Future work in this field must focus on slagging and deposition, which is a primary concern amongst power station operators with regards to co-firing.

Chapter 7

Discussion and Conclusions

7.1 General Discussion

The thesis has focused on two related areas of pulverised fuel co-fire modelling, namely those of non-spherical particle aerodynamics and large scale combustion, and in both cases employing the commercial software, ANSYS Fluent. The topics were split since negligible effects of chemistry present themselves before ignition at the burner, whereas turbulent reactions were expected to dominate within the furnace, so simplified aerodynamics would be considered.

The co-firing of coal with biomass has been an important field of research for a number of years. It was initially used as a cost effective means for reducing the NO_x emissions of coal power stations and has enjoyed invigorated attention from the 1980s to the present day in application to the reduction of fossil-CO₂ emissions and later the expansion of renewable energy. Despite this, a modal shift in the production of biomass has not been seen and it remains a relatively expensive fuel, on a dry calorific basis, due to the land and labour intensive processes of cultivation and collection, so within Europe, the market is dependent upon governmental subsidies. Recently co-firing has received a renewal of interest yet again, this time as the means to SO₂ emissions reduction. In Europe, 2016 will see a drop to 1500h in the annual hours of operation for solid fuel (except biomass) plants subject to the SO₂ limit, which is 400mgNm⁻³ for an existing 500MW_{th} or greater thermal plant, or for those termed “new build” (construction licence obtained after 1987) 200mgNm⁻³ will have to be achieved by any in excess of 100MW_{th} (EC, 2001 and 2011). Biomass is legislated separately to the other solid fuels but has the same emissions limits for large scale plants, therefore the effective limit for the calorific fraction of the coal may be increased by the addition of biomass.

In contrast to this, since the initial submission of this thesis a very great financial threat to co-firing in the UK has emerged. Governmental consultation on ROC banding

has responded to reduce the RO value of co-firing based on the biomass loading (DECC, 2012). This will see the ROCs earned on less than 0.5 biomass loading drop by 40% in 2013 and is particularly problematic as no grandfathering policy exists for this lowest biomass loading band. Essentially low level co-firing has become commercially unviable and confidence in investment for co-firing will have waned, due to the lack of financial certainty.

Computational fluid dynamics (CFD) has been used for fluid flow problems, without closed form solutions, since early in the twentieth century with human computers performing the calculations. However it became a serious separate field of research in the late 1950s with the reduction in cost for electronic computational power. The code which would become Fluent started in 1961 with the Eulerian finite-difference method (FDM) for fluid flow. Fluid turbulence and combustion modelling was incorporated due to work at the University of Sheffield in the 1970s and 80s. The Lagrangian coal particle combustion model developed in the 1990s from oil spray modelling and the solid combustion models remain in the frame-work of discrete droplets. As of 2010, standard models provided within Fluent covered, amongst others, the following: convective and radiative heat transfer models, wet combustion, devolatilisation and char combustion for the solid particles and also a coal calculator tool, to automate much of the combustible particle material and multi-species fluid mixture input. This works very well where a single particulate fuel is required. In addition a fixed-orientation non-spherical drag model is available as well as a form of the Saffman lift model intended for submicron particles amongst other models for micro-scale particles, such as Brownian motion and thermophoresis. However, the standard non-spherical drag may only accept sphericity as the shape factor and uses the same value for all particle trajectory calculations. The drag model and sphericity value would have to be changed manually between separate injections of shaped particles, or more easily a journal file could be written, but neither method integrates well with the inbuilt discrete phase model (DPM) report function. Also the average particle of coal dust is around a million times the volume of the limit for the Saffman lift model included and so over predicts for PF applications. Since that time other improvements have been released, the most relevant to the work of this thesis being the dense discrete

phase model (DDPM). This uses a combination of the DPM and multiphase models (both Lagrangian and Eulerian particle phases) within the Eulerian fluid to model inter-particle collisions in high volume concentration particle flows, as the drag force upon the Lagrangian particles due to the Eulerian particle phase, in a similar manner to Pirker *et al.* (2009). The method requires two-way coupling of the discrete and fluid phases.

This state of the commercial CFD software shows the extensive research into coal modelling, which is beneficial to co-fire modelling, as well as the acceptance of fixed-orientation drag models. Therefore a solid foundation for development of new models is provided with portability for other researchers. However, the reverse of this is working around a black box. Although Fluent provides several user-defined function (UDF) macros to enable additional models it takes experience to learn the full limits, capabilities and computational effort of their use. The results can be highly unpredictable when the existing macros must be used for calculations outside of their intended purpose.

Furthermore, the modeller must follow existing experimental data in order to provide validation, this precludes many desired investigations. Recognition must be given to the very challenging environment, in which the industrial experimentalist works. However, even with the scarce experimental data that is available, it is difficult to capture the full effect of individual numerical models when the result can only be quantitatively compared at sparse measurement locations and at large margins of error.

7.2 Overall Conclusions

The objectives of the thesis, as set down in section 1.4, have been achieved, providing an overview of the current options available to co-fire modellers in terms of advanced non-spherical particle aerodynamics and the standard coal combustion models. In the course of these investigations, impediments to the successful implementation of the models to experimentally validated test cases have been identified. These being the cumbersome nature to the execution of some user defined models within black-box software, the great computational commitment required to simulate additional phenomena and the lack of good quality data.

In Chapter 4, Biomass Fuel Particle Aerodynamics in a Pipeline, investigation into the flow of biomass particles in a pipe showed that for dilute suspensions in an horizontal pipe with lateral secondary flows the only change that must be made to the standard spherical particle model, for acceptable results, is for the drag experienced to be augmented based on the fixed-orientation drag law by Haider and Levenspiel (1989). It was expected that, in an horizontal pipe, drag would not oppose gravity and therefore, although drag still dominates the flow velocity, the lift, inter-particle collision and wall collision models, as well as turbulent dispersion, would become significant as the only methods through which vertical motion opposing gravity could be imparted to the particle. However, in general, it is found that where recirculation of the particles is induced by a secondary fluid flow, such as that present following a bend in a pipe, the particle drag provides the means to travel against gravity and therefore modelling other phenomena is of less significance. Also the non-spherical drag model is required to correctly predict the flow velocity of the acicular particles. It is important to note that the use of the spherical drag model presents significantly reduced flow velocity compared to the experimental data.

Predictions of various blends of biomass, representing coal/biomass combinations (flour and willow) were found to be in good agreement, irrespective of the conveying velocities and mass loadings. Stable particle distributions and transportation throughout the measuring section of the pipe is also observed. The effects of the inter-particle collisions were less quantifiable and may not be significant in the case of mass loadings

less than about 5%. The influence of the physical properties on particle transportation has been clearly demonstrated. Although the chemical properties of the biomass were not considered, they are expected to have some influence on the transportation, especially moisture content resulting in adhesion and agglomeration, which may be considered for future study.

In Chapter 5, Coal and Biomass Pneumatic Transportation Modelling in a Swirl Burner, the perpendicular feedpipe to the primary air annulus once again induced a secondary flow that gives rise to a trail of particles at the top of the inner wall under steady flow conditions. Direct collisions with the flame holder, that partially obstructs the primary air annulus, and the turbulence in this region, rapidly mixes, but does not destroy, the irregular distribution of particles at the flame holder position. A comparison of photographic evidence from experiments and a previous numerical study (Ma *et al.*, 2009) shows that a large eddy simulation (LES) of coal and biomass co-fire flame, assuming a uniform distribution of particles, accurately predicts the physical case. Therefore the asymmetry of the particle distribution predicted in this chapter does not fully capture all the physics but it does underline an area in which knowledge is lacking.

In Chapter 6, Co-firing Chinese Straw with Coal in a 300MW_e Tangentially Fired Pulverised Fuel Furnace, a challenging combustion case was modelled requiring careful meshing and an informed estimation of the unmeasured boundary conditions. It was found that a close match is made between the experimentally determined excess oxygen and that within the exhaust of the numerical prediction, when the air flow rate and fuel flow rate are determined on the back of an envelope, but if the experimental air flow rate is used then a disparity is observed. The difference is caused by the measurement error within the air flow rate, excess air coefficient and fuel stoichiometry. In addition, good agreement was found between the predicted temperature results and the experimental data using the standard particle combustion models (e.g. devolatilisation and char combustion), treating all particles as spherical aerodynamically and reactively. This is a positive result for operators and presents a useful addition to the small pool of paired experimental and numerical work for full scale coal and biomass co-firing. Unfortunately the levels of biomass loading do not cause significant change in the measured furnace temperatures. The reason for this is twofold, first because the

temperature measurements could only be carried out away from the flame and also due to the expense and risk of performing the experiments with high biomass loadings. This means that the adequacy of the standard models as used in this case may not extend generally to biomass combustion, but is suitable for similar co-fire loads. In addition, detailed information from the numerical calculations within the burner region still has no experimental support to improve theoretical models.

A particular goal of CFD simulations of thermal energy generation is to predict accurate NO_x emissions. In this thesis a trend of decreasing NO_x with biomass loading was successfully predicted. Accurate quantitative prediction of NO_x is a very challenging topic. This is due not only to the sensitivity of the results to the NO_x model constants themselves, taken from measured fuel-N properties at lower temperature conditions, but also the temperature and species field obtained from the simulations. In addition, the experimental NO_x measurement is in effect a temporal average over the time taken to fill the gas bag and although the Reynolds-averaged Navier-Stokes (RANS) ensemble average is also temporal, applying NO_x predictions to the averaged flow field does not equate to using the raw turbulence data in NO_x calculations and subsequently averaging. Due to the highly dynamic reversible reactions of oxygen and nitrogen based radicals, a more computationally expensive unsteady RANS or LES simulation may identify pockets of flow, that are highly conducive to the production of the pre-cursors to NO_x, that do not exist in the steady calculations performed herein. Finally, the accuracy of the industrial NO_x concentration measurements should also be borne in mind. The prediction of unburnt-carbon (UBC) in flyash shares the problems with that of NO_x, in the form of dependence upon local temperature and species conditions, possible extinction of particles in the entropic flow, that is not captured in relatively simple turbulence modelling, and complex chemistry modelling based on variable fuel properties from low temperature experiments. In particular the model is found to be hypersensitive to the intrinsic activation energy, E_i .

In summary the findings of the thesis are:

- Modelling the aerodynamics of a dilute suspension of biomass particles in an horizontal pipe with a secondary flow that acts to suspend the particles, only requires a fixed-orientation drag model for accurate bulk velocity predictions. However, where the

lateral fluid velocity is negligible, the lift of the particles along the shear velocity gradients may be significant and the Saffman lift model is simple to implement within Fluent. Due to the restraints of the on-line sensing equipment, greater density particle loading could not be investigated with experimental validation. Even with simple elastic wall collisions, the qualitative trend of gravimetric stratification of the particle concentration was replicated. The precise quantitative extent to this cannot be gleaned from the experimental data, nor can the trend of evacuation of the particles from the central region of the pipe, as observed in the numerical results.

- When the feedpipes are neglected from the computational domain, in a full scale furnace, the numerical results are not highly sensitive to the particle aerodynamics. In addition, with low biomass loadings, less than about 12%, the use of the spherical surface area of the biomass particles in chemical reaction is acceptable. The standard combustion models have many ill-measurable constants and the accuracy of new models will never be able to exceed that of the measurement of their constants. Moreover, for accurate UBC or NO_x models, let alone alkaline metal emissions from biomass, slagging or fouling, the challenges in experimental measurements must be overcome so that a greater understanding of the combustion within a furnace is achieved.

- Another aspect to coal and biomass co-firing that has received much lesser attention is the pneumatic transportation. This thesis presents an investigation using programmed UDFs to model non-spherical drag, Saffman lift force, randomised impulsive wall collisions and stochastic inter-particle collisions. The method predicts a steady inconsistency in the distribution of the particles at the flame holder location (the end of the primary-air annulus). The prediction does not appear to be in agreement with experimental experience from the test rig. An alternative explanation may be that, physically, devolatilisation of the fuel particles begins inside the primary-air duct and the volatile gases mix relatively uniformly before the burner mouth. This causes a complete flame once turbulent ignition takes place at the flame holder, and that this same behaviour is captured by the simulation of a uniformly distributed distribution of particles that devolatilise very rapidly, but such a chemical response could not be modelled in this cold-flow aerodynamics investigation. Academically, this is a topic that

requires more research and the results obtained could be used to inform future plant designers.

7.3 Future Work

Further work is required for the application of these investigations to better inform industrial designers. Coupled experimental data and numerical simulations of a representative feedline system with a range of coals and biomass, including gaseous emissions from the particle should be performed. The behaviour observed in the experiments may suggest that unsteady multi-phase physics is required in the simulations. In particular, the modelling of agglomeration is expected to be of significance where biomass particles are generally large and wet, compared to coal, resulting in aggregation of the biomass particles, and electrostatic attraction and hydro-adhesion of the coal dust to the larger biomass particles. This would tend to produce larger particle clumps and a more inertial particulate flow as well as retarding the ignition of such clusters. An adjunct application of the agglomeration model would be to slagging and fouling with the aggregation of ash particles. Furthermore an accretion model of particles to the wall during the conveyance and ash deposition should add value to the simulations. It is currently difficult to assess the success of the non-spherical aerodynamics and combustion models for biomass towards the secondary goals, these being UBC and NO_x predictions and moving forward into more exotic, corrosive, emissions. The greater reaction surface, and change in the temperature history of a particle that may result from the different aerodynamic responses, based on its shape, do not appear significant in furnace temperature predictions. However, this should become more important for UBC and NO_x emissions. Ultimately, CFD simulations could be used to predict the conveying air velocities, temperatures, minimum milling requirements and fuel blends to provide sufficient mixing for ignition at, but not before, the burner and tolerable deposition behaviour.

In terms of academic aspirations, numerical simulation should be able to handle the entire process of PF power generation, from unmilled fuel to ash filtration. This may eliminate many of the guessed boundary condition assumptions that must be made due to the arbitrary boundaries imposed on open-systems. The milling and pneumatic

transport systems require extensive individual investigations, the future challenges for the combustion chamber have already been discussed in the previous paragraph, and the challenges of computational psychrometrics, for the steam cycle, remain formidable, before the assembly of these components to a full power station model. Such a model could predict the lifetime load cycles of the system components, aid modular design and minimise their cost, as well as identify minimal wear operational regimes and expose unforeseen causes of inefficiency. This presents a vast field for research, but one that is currently precluded by computational expense. On the other hand, to many, an engineer's experience would be considered equal to the separate tasks achieved by the method.

More optimistically, were there ever a dawning of the room-temperature superconductor age, heralding a vast improvement in computing power, CFD may be greatly freed from imposed restraints upon computational expense. This would allow a shift from modelling to direct numerical simulation (DNS) from first principles with huge FDM grids. However, this would also require the detailed physical knowledge and accurate experimental information.

References

- Abbas T, Awais MM, Lockwood FC.** (2003) *An artificial intelligence treatment of devolatilisation for pulverised coal and biomass in co-fired flames.* Combustion and Flame 132:305-318
- ANSYS** (2009a) *Fluent Theory Guide Version 12.* ANSYS Inc, USA
- ANSYS.** (2009b) *Fluent UDF Manual.* ANSYS Inc, USA.
- ANSYS.** (2009c) *Fluent User's Guide Version 12.* ANSYS Inc, USA.
- Apte SV, Mahesh K, Moin P, Oefelein JC.** (2003) *Large-eddy simulation of swirling particle-laden flows in a coaxial-jet combustor.* International Journal of Multiphase Flow 29:1311-1331
- Arsenijovic ZL, Grbavcic ZB, Garic-Grulovic RV, Zdanski FK.** (1999) *Determination of non-spherical particle terminal velocity using particulate expansion data.* Powder Technology 103:265-273
- Backreedy RI, Fletcher LM, Ma L, Pourkashanian M, Williams A.** (2006) *Modelling pulverised coal combustion using a detailed coal combustion model.* Combustion Science and Technology 178:763-787
- Backreedy RI, Jones JM, Ma L, Pourkashanian M, Williams A, Arenillas A, Arias B, Pis JJ, Rubiera F.** (2005) *Prediction of unburned carbon and NO_x in a tangentially fired power station using single coals and blends.* Fuel 84:2196-2203
- Badzioch S, Hawksley PGW.** (1970) *Kinetics of the thermal decomposition of pulverised coal particles.* Industrial Engineering Chemical Process Design Development 9(4):521-530
- Basu P, Butler J, Leon MA.** (2011) *Biomass co-firing options on the emission reduction and electricity generation costs in coal-fired power plants.* Renewable Energy 36:282-288
- Basu P, Kefa C, Jestin L** (2000) *Boilers and Burners Design and Theory.* Springer, New York.
- Batchelor GK** (2000) *An introduction to fluid dynamics.* Cambridge University Press, Cambridge.

- Battista JJ, Hughes EE, Tillman DA.** (2000) *Biomass co-firing at Seward station.* Biomass and Bioenergy 19:419-427
- Baum MM, Street PJ.** (1971) *Predicting the combustion behaviour of coal particles.* Combustion Science and Technology 3:231-243
- Baxter L.** (2005) *Biomass-coal co-combustion: opportunity for affordable renewable energy.* Fuel 84:1295-1302
- Belosevic S, Sijercic M, Tuckovic D, Crnomarkovic N.** (2008) *A numerical study of a utility boiler tangentially-fired furnace under different operating conditions.* Fuel 87: 3331-3338
- Besnard D, Harlow FH.** (1986) *Nonspherical particles in two-phase flow.* International Journal of Multiphase Flow 12(6):891-912
- Bocksell TL, Loth E.** (2001) *Random walk models for particle diffusion in free-shear flows.* AIAA Journal 39(6):1086-1096
- BP** (2011) [British Petroleum] *Statistical Review of World Energy June 2011.* www.bp.com [June 2011]
- Cai JM, Liu RH, Deng CJ, Shen F.** (2007) *Amount, availability and potential uses for energy of agricultural residues in mainland China.* Journal of the Energy Institute 80(4):243-246
- Cao GL, Zhang XY, Wang YQ, Zheng FC.** (2008) *Estimation of emissions from field burning of crop straw in China.* Chinese Science Bulletin 53(5):784-790
- Cao J, Ahmadi G.** (1995) *Gas-particle two-phase turbulent flow in a vertical duct.* International Journal of Multiphase Flows 21(6):1203-1228
- Carter RM, Yan Y, Cameron SD.** (2005) *On-line measurement of particle size distribution and mass flow rate of particles using combined imaging and electrostatic sensors.* Flow Measurement and Instrumentation 16(5):309-314
- Carter RM, Yan Y.** (2005) *An instrumentation system using combined sensing strategies for on-line mass flow rate measurement and particle sizing.* IEEE Transactions on Instrumentation and Measurement 54(4):1433-1437
- Cash JR, Karp AH.** (1990) *A variable order Runge-Kutta method for initial value problems with rapidly varying right-hand sides.* ACM Transactions of Mathematical Software 16(3):201-222

- Chhabra RP, Agarwal L, Sinha NK.** (1999) *Drag on non-spherical particles: an evaluation of available methods.* Powder Technology 101:288-295
- Chinnayya A, Chtab A, Shao J, Carter RM, Yan Y, Caillat S.** (2009) *Characterisation of pneumatic transportation of pulverized coal in a horizontal pipeline through measurement and computational modelling.* Fuel 88:2348-2356
- Choi CR, Kim CN.** (2009) *Numerical investigation on the flow, combustion and NO_x emission characteristics in a 500MWe tangentially fired pulverised-coal boiler.* Fuel 88: 1720-1731
- Clift R, Grace JR, Weber ME.** (1978) *Bubbles, Drops and Particles.* Academic Press, London
- Crowe CT, Sommerfeld M, Tsuji Y.** (1998) *Multiphase flows with droplets and particles.* CRC Press, Boca Raton
- Dai J, Sokhansanj S, Grace JR, Bi X, Lim CJ, Melin S.** (2008) *Overview and some issues related to co-firing biomass and coal.* The Canadian Journal of Chemical Engineering 86:367-386
- Damstedt B, Pederson JM, Hansen D, Knighton T, Jones J, Christensen C, Baxter L, Tree D.** (2007) *Biomass co-firing impacts on flame structure and emissions.* Proceedings of the Combustion Institute 31:2813-2820
- Dandy DS, Dwyer HA.** (1990) *A sphere in shear flow at finite Reynolds number: effect of shear on particle lift, drag, and heat transfer.* Journal of Fluid Mechanics 216:381-410
- Darvell LI, Jones JM, Gudka B, Baxter XC, Saddawi A, Williams A, Malmgren A.** (2010) *Combustion properties of some power station biomass fuels.* Fuel 89:2881-2890.
- DECC** (2010) [Department of Energy and Climate Change] *The renewables obligation (amendment) order 2010* requires the original *The renewables obligation order 2009.* www.decc.gov.uk [2011]
- DECC** (2012) *Fact sheet: Grandfathering and cost control for biomass co-firing and conversions.* www.decc.gov.uk [2012]
- Dennis SCR, Singh SN, Ingham DB.** (1980). *The steady flow sue to a rotating sphere at low and moderate Reynolds numbers.* Journal of Fluid Mechanics 101(2):257-279

- Díez LI, Cortés C, Pallarés J.** (2008) *Numerical investigation of NO_x emissions from a tangentially-fired utility boiler under conventional and overfire air operation.* Fuel 87: 3331-3338
- Dobrowolski B, Wydrych J.** (2007) *Computational and experimental analysis of gas-particle flow in furnace power boiler installations with respect to erosion phenomena.* Journal of Theoretical and Applied Mechanics 45:513-537
- Donea J, Huerta A.** (2003) *Finite element methods for flow problems.* Wiley, Chichester.
- Eaton AM, Smoot LD, Hill SC, Eatough CN.** (1999) *Components, formulations, solutions, evaluation and application of comprehensive combustion models.* Progress in Energy and Combustion Science 25:387-436
- EC** (2001) [European Commission] *Large Combustion Plant Directive 2001/80/EC.* www.defra.gov.uk [2012]
- EC** (2011) *Industrial Emissions Directive 2010/75/EU.* www.defra.gov.uk [2011]
- Edge P, Gubba SR, Porter R, Pourkashanian M, Jones JM, Williams A.** (2011) *LES modelling of air and oxy-fuel pulverised coal combustion – Impact on flame properties.* Proceedings of the Combustion Institute 33:2709-2716
- Ferrante A, Elghobashi SE.** (2003) *On the physical mechanisms of two-way coupling in particle-laden isotropic turbulence.* Physics of Fluids 15:315–329
- Fuchs A, Zangl H, Brasseur G, Petriu EM.** (2006) *Flow-velocity measurement for bulk granular solids in pneumatic conveyor pipes using random-data correlator architecture.* IEEE Transactions on Instrumentation and Measurement 55(5):1228-1234
- Gabitto J, Tsouris C.** (2007) *Drag coefficient and settling velocity for particles of cylindrical shape.* Powder Technology 183:314-322
- Ganser GH.** (1993) *A rational approach to drag prediction of spherical and nonspherical particles.* Powder Technology 77:143-152
- Gera D, Mathur M, Freeman M, O’Dowd W.** (2001) *Moisture and char reactivity modelling in pulverised coal combustors.* Combustion Science and Technology 172: 35-69
- Gera D, Mathur MP, Freeman MC, Robinson A.** (2002) *Effect of large aspect ratio biomass particles on carbon burnout in a utility boiler.* Energy and Fuels 16:1523-1532

- Glarborg P, Jensen AD, Johnsson JE.** (2003) *Nitrogen conversion in solid fuel fired systems*. Progress in Energy and Combustion Science 29:89-113
- Göz MF, Laín S, Sommerfeld M.** (2004) *Study of numerical instabilities in Lagrangian tracking of bubbles and particles in two-phase flow*. Computers and Chemical Engineering 28:2727-2733
- Gubba SR, Pourkashanian M, Williams A.** (2011) *Effect of internal heat transfer within large coal/biomass particles on combustion in a pulverised coal/biomass fired combustion test facility*. Fuel Processing Technology 92:2185-2195
- Haider A, Levenspiel O.** (1989) *Drag coefficient and terminal velocity of spherical and nonspherical particles*. Powder Technology 58(1):63-70
- Hansson J, Berndes G, Johnsson F, Kjärstad, J.** (2009) *Co-firing biomass with coal for electricity generation – an assessment of the potential in EU27*. Energy Policy 7: 1444–1455
- Hinze J.** (1975) *Turbulence*. McGraw-Hill, New York.
- Hughes PC.** (2004) *Spacecraft Attitude Dynamics*. Dover, New York.
- IEA.** (2011) [International Energy Agency] *Energy Statistics*. www.iea.org [June 2011]
- Jones JM, Pourkashanian M, Waldron DJ, Williams A.** (2010) *Prediction of NO_x and unburned carbon in ash in highly staged pulverised coal furnace using overfire air*. Journal of the Energy Institute 83(3):144-150
- Ku XK, Lin JZ.** (2008) *Motion and orientation of cylindrical and cubic particles in pipe flow with high concentration and high particle to pipe size ratio*. Journal of Zhejiang University, Science A 9(5):664-671
- Kurose R, Makino H.** (2003) *Large eddy simulation of a solid-fuel jet flame*. Combustion and Flame 135:1-16
- Laín S, Grillo CA.** (2007) *Comparison of turbulent particle dispersion models in turbulent shear flows*. Brazilian Journal of Chemical Engineering 24(3):351-361
- Laín S, Sommerfeld M, Kussin J.** (2002) *Experimental studies and modelling of four-way coupling particle-laden horizontal channel flow*. International Journal of Heat and Fluid Flow 23:647-656
- Laín S, Sommerfeld M.** (2008) *Euler/Lagrange computations of pneumatic conveying in a horizontal channel with different wall roughness*. Powder Technology 184:76-88

- Lin CKK, Liu HS.** (1997) *Numerical simulation of dilute turbulent gas-solid flows in horizontal channels.* International Journal of Multiphase Flow 23(3):575-605
- Lin W, Jensen PA, Jensen AD.** (2009) *Biomass Suspension Combustion: Effect of two-stage combustion on NO_x emissions in a laboratory-scale swirl burner.* Energy and Fuels 23:1398-1405
- Loth E.** (2008) *Drag of non-spherical solid particles of regular and irregular shape.* Powder Technology 182:342-353
- Lu Y, Glass DH, Easson WJ.** (2009) *An investigation of particle behaviour in gas-solid horizontal pipe flow by an extended LDA technique.* Fuel 88:2520-2531
- Lu H, Elvin IP, Scott J, Foster P, Vickers M, Baxter LL.** (2010) *Effects of particle shape and size on devolatilisation of biomass particle.* Fuel 89(5):1156-1168
- Ma L, Gharebaghi M, Porter R, Pourkashanian M, Jones JM, Williams A.** (2009) *Modelling methods for co-fired pulverized fuel furnaces.* Fuel 88:2448-2454
- Ma L, Jones JM, Pourkashanian M, Williams A.** (2007) *Modelling the combustion of pulverised biomass in an industrial combustion test furnace.* Fuel 86:1959-1965
- Massey B.** (1998) *Mechanics of fluids.* Stanley Thornes, Cheltenham.
- Matsumoto S, Saito S.** (1970) *Monte Carlo simulation of horizontal pneumatic conveying based on the rough wall model.* Journal of Chemical Engineering Japan 3:223-230
- Maxey MR, Patel BK.** (2001) *Localised force representations for particles sedimenting in Stokes flow.* International Journal of Multiphase Flow 27:1603-1626
- McKendry P.** (2002) *Energy production from biomass (part 2): conversion technologies.* Bioresource Technology 83:47-54
- Mei R.** (1992) *An approximate expression for the shear lift on a spherical particle at finite Reynolds number.* International Journal of Multiphase Flow 18(1):145-147
- Minier JP, Peirano E.** (2001) *The pdf approach to turbulent poly-dispersed two-phase flows.* (Elsevier) Physics Reports 532:1-214
- Morsi SA, Alexander AJ.** (1972) *An investigation of particle trajectories in two-phase flow systems.* Journal of Fluid Mechanics 55(2):193-208
- OECD** (2010) *Factbook.* www.oecd-ilibrary.org [June 2011]

- Oesterlé B, Bui Dinh T.** (1998) *Experiments on the lift of a spinning sphere in a range of intermediate Reynolds numbers.* Experiments in Fluids 25:16-22
- Oesterlé B, Petitjean A.** (1993) *Simulation of particle-to-particle interactions in gas-solid flows.* International Journal of Multiphase Flow 19(1):199-211
- Pedersen KH, Jensen AD, Berg M, Olsen LH, Dam-Johansen K.** (2009) *The effect of combustion conditions in a full-scale low-NO_x coal fired unit on fly ash properties for its application in concrete mixtures.* Fuel Processing Technology 90:180-185
- Pelegrina AH, Crapiste GH.** (2000) *Modelling the pneumatic drying of food particles.* Journal of Food Engineering 48:301-310
- Perry AE, Henbest SM, Chong MS.** (1986) *A theoretical and experimental study of wall turbulence.* Journal of Fluid Mechanics 165:163–99
- Pirker S, Kahrmanovic D, Aichinger G.** (2009) *Modelling mass loading effects in industrial cyclones by a combined Eulerian-Lagrangian approach.* Acta Mechanica 204:203-216
- Pozorski J, Apte SV.** (2009) *Filtered particle tracking in isotropic turbulence and stochastic modelling of subgrid-scale dispersion.* International Journal of Multiphase Flow 35:118–128
- Qian X, Yan Y, Malmgren A.** (2011) *Flow measurement of pneumatically conveyed biomass-coal particles using multi-channel electrostatic sensors.* I2MTC 2011, accepted.
- Roache PJ.** (1998) *Fundamentals of computational fluid dynamics.* Hermosa, Albuquerque.
- Robinson AL, Rhodes JS, Keith DW.** (2003) *Assessment of potential carbon dioxide reductions due to biomass-coal cofiring in the United States.* Environmental Science and Technology 37:5081–5089
- Rosendahl L.** (2000) *Using a multi-parameter particle shape description to predict the motion of non-spherical particle shapes in swirling flow.* Applied Mathematical Modelling 24:11-25
- Rubinow SI, Keller JB.** (1961) *The transverse force on a spinning sphere moving in a viscous fluid.* Journal of Fluid Mechanics 11:447-459

- Rundqvist R, Ljus C, van Wachem B.** (2005) *Experimental and numerical investigation of particle transport in a horizontal pipe*. American Institute of Chemical Engineers Journal 51(12):3101-3108
- Saddawi A, Jones JM, Williams A, Wójtowicz MA.** (2010) *Kinetics of thermal decomposition of biomass*. Energy and Fuels 24:1274-1282
- Saffar-Avval M, Tabrizi HB, Mansoori Z, Ramezani P.** (2007) *Gas-solid turbulent flow and heat transfer with collisional effect in a vertical pipe*. International Journal of Thermal Sciences 46:67-75
- Sami M, Annamalai K, Wooldridge M.** (2001) *Co-firing coal and biomass fuel blends*. Progress in Energy and Combustion Science 27:171-214
- Schneider H, Frank T, Pachler K, Bernet K.** (2002) *A numerical study of the gas-particle flow in pipework and flow splitting devices of coal-fired power plant*. 10th Workshop on Two-Phase Flow Predictions, 9th-12th April 2002, Martin-Luther-Universität Halle-Wittenberg, Halle, Germany 227-236 (Ed. Sommerfeld M)
- Shao J, Krabicka J, Yan Y.** (2007) *Comparative studies of electrostatic sensors with circular and probe electrodes for the velocity measurement of pulverised coal*. Chinese Journal of Scientific Instruments 28(11):1921-1926
- Shao J, Krabicka J, Yan Y.** (2010) *Velocity measurement of pneumatically conveyed particles using intrusive electrostatic sensors*. IEEE Transactions on Instrumentation and Measurement 59(5):1477-1484
- Slade R.** (2012) *The role of biomass in future global energy supply*. Energy World February 2012 14-15
- Smith IW** (1982) *The combustion rates of coal chars: A review*. The Combustion Institute 19:1045-1065
- Smith KL, Smoot LD, Fletcher TH, Pugmire RJ** (1994) *The structure and reaction processes of coal*. Plenum Press, New York.
- Sommerfeld M, Huber N.** (1999) *Experimental analysis and modelling of particle-wall collisions*. International Journal of Multiphase Flow 25:1457-1489
- Sommerfeld M.** (2001) *Validation of a stochastic Lagrangian modelling approach for inter-particle collision in homogeneous isotropic turbulence*. International Journal of Multiphase Flow 27:1829-1858

- Sommerfeld M.** (2002) *Modelling of particle-wall collisions in confined gas-particle flows*. International Journal of Multiphase Flow 18(6):905-926
- Sommerfeld M.** (2003) *Analysis of collision effects for turbulent gas-particle flow in a horizontal channel: Part I. Particle transport*. International Journal of Multiphase Flow 29:675-699
- Tsuji Y, Morikawa Y, Tanaka T, Nakatsukasa N, Nakatani M.** (1987) *Numerical simulation of gas-solid two-phase flow in a two-dimensional horizontal channel*. International Journal of Multiphase Flow 13(5):671-684
- van Loo S, Koppejan J.** (2008) *Biomass Combustion and Co-firing*. Earthscan, London.
- Vassilev SV, Baxter D, Andersen LK, Vassileva CG.** (2010) *An overview of the chemical composition of biomass*. Fuel 89:913-933
- Versteeg HK, Malalasekera W.** (1995) *An introduction to computational fluid dynamics: The finite volume method*. Longman Scientific and Technical, Harlow.
- Vreman AW.** (2007) *Turbulence characteristics of particle-laden pipe flow*. Journal of Fluid Mechanics 584:235-279
- Wang X, Tan H, Niu Y, Pourkashanian M, Ma L, Chen E, Liu Y, Liu Z, Xu T.** (2011) *Experimental investigation on biomass co-firing in a 300MW pulverised coal-fired utility furnace in China*. Proceedings of the Combustion Institute 33:2725-2733
- Wang Y, Yan L.** (2008) *CFD studies on biomass thermochemical conversion*. International Journal of Molecular Sciences 9:1108-1130
- Williams A, Backreedy R, Habib R, Jones J, Pourkashanian M.** (2002) *Modelling coal combustion: the current position*. Fuel 81:605-618
- Williams A, Pourkashanian M, Jones JM.** (2000a) *The combustion of coal and some other solid fuels*. Proceedings of the Combustion Institute 28:2141-2162
- Williams A, Pourkashanian M, Jones JM.** (2001) *Combustion of coal and biomass*. Progress in Energy and Combustion Science 27:587-610
- Williams A, Pourkashanian M, Jones JM, Skorupska N.** (2000b) *Combustion and gasification of coal*. Taylor and Francis, New York.

- Wornat MJ, Hurt RH, Yang NYC, Headley TJ.** (1995) *Structural and compositional transformations of biomass chars during combustion.* Combustion and Flame 100: 131-143
- Yan Y, Byrne B, Woodhead S, Coulthard J.** (1995) *Velocity measurement of pneumatically conveyed solids using electrodynamic sensors.* Measurement Science and Technology 6:515-537
- Yan Y.** (2001) *Guide to the flow measurement of particulate solids in pipelines. Part I: Fundamentals and principles.* Powder Handling Processes 13(4):343–52
- Yang YB, Sharifi VN, Swithenbank J, Ma L, Darvell LI, Jones JM, Pourkashanian M, Williams A.** (2008) *Combustion of a single particle of biomass.* Energy and Fuels 22(1):306-316
- Yasuna JA, Moyer HR, Elliot S, Sinclair JL.** (1995). *Quantitative predictions of gas-particle flow in a vertical pipe with particle-particle interactions.* Powder Technology 84: 23-34
- Yilmaz A, Levy EK.** (2001) *Formation and dispersion of ropes in pneumatic conveying.* Powder Technology 114: 168-185
- Yin C, Rosendahl L, Kær SK, Condra TJ.** (2004). *Use of numerical modelling in design for co-firing biomass in wall-fired burners.* Chemical Engineering Science 59: 3281-3292
- Yin C, Rosendahl L, Kær SK, Sørensen H.** (2003) *Modelling the motion of cylindrical particles in a nonuniform flow.* Chemical Engineering Science 58: 3489-3498
- Zhang H, Ahmadi G, Fan FG, McLaughlin JB.** (2001) *Ellipsoidal particles transport and deposition in turbulent channel flows.* International Journal of Multiphase Flow 27: 971-1009
- Zienkiewicz OC, Taylor RL, Nithiarasu P.** (2005) *The finite element method for fluid dynamics.* Elsevier Butterworth Heinemann, London.

Appendix

A-I Particle rotational relaxation time

In this section the particle rotational relaxation time is derived in two dimensions. This is the same in 3D when the fluid rotation is taken as that in the plane perpendicular to the axis of particle rotation. The identities which relate the particle angular acceleration to the relative angular velocity between the fluid and particle surface and therefore the rotational relaxation times are presented here:

$$\begin{aligned}\dot{\vec{\omega}}_p &\equiv H\vec{\Omega} \\ H^{-1} &\equiv \tau_\omega\end{aligned}\tag{A.1}$$

where $\dot{\vec{\omega}}_p$ [$^c s^{-2}$], is the particle angular acceleration, H [s^{-1}], is the inverse of the rotational relaxation time and this is constant over a single timestep, $\vec{\Omega}$ [$^c s^{-1}$], is the relative angular velocity between the particle and the fluid (defined in equation [3.37]) and, τ_ω [s], is the particle rotational relaxation time. For simplicity, a linear relationship is assumed to exist over each timestep associated with constant angular acceleration. At the lower Re_r values (Rubinow and Keller, 1961) that the particles are expected to experience, the coefficient of rotation has an inverse dependence upon Re_r , resulting in a ‘‘Stokes’ regime’’ for the rotary particle response, with a linear relationship between the drag torque and relative angular velocity, in which H is permanently constant. The relaxation time is derived from the expressions above as follows:

$$\begin{aligned}\dot{\vec{\omega}}_p &\equiv H\vec{\Omega} \\ \Rightarrow \frac{d\vec{\omega}_p}{dt} &= H(\vec{\omega}_f - \vec{\omega}_p) \Rightarrow \int (\vec{\omega}_f - \vec{\omega}_p)^{-1} d\vec{\omega}_p = \int H dt \\ \Rightarrow -\ln(\vec{\omega}_f - \vec{\omega}_p) &= Ht + c \Rightarrow (\vec{\omega}_f - \vec{\omega}_p)^{-1} = e^{Ht+c} = Ae^{Ht}\end{aligned}\tag{A.2}$$

where, $\vec{\omega}_f$ and $\vec{\omega}_p$ [$^c s^{-1}$], are, respectively, the fluid and particle angular velocities.

If the particle is initially rotationally quiescent then there is a boundary condition for $\vec{\omega}_p(t)$:

$$\begin{aligned}\vec{\omega}_p(0) = 0 &\Rightarrow (\vec{\omega}_f - 0)^{-1} = A e^0 \Rightarrow A = \vec{\omega}_f^{-1} \\ \Rightarrow (\vec{\omega}_f - \vec{\omega}_p)^{-1} &= \vec{\omega}_f^{-1} e^{Ht} \Rightarrow \vec{\omega}_f - \vec{\omega}_p = \vec{\omega}_f e^{-Ht} \Rightarrow \vec{\omega}_p = \vec{\omega}_f (1 - e^{-Ht})\end{aligned}\quad [\text{A.3}]$$

At time $t = H^{-1}$, $\vec{\omega}_f - \vec{\omega}_p$ will have reached e^{-1} of its original value ($\approx 36.7\%$). Hence the definition of τ_ω gives the rate of an exponential decay in the relative angular velocity.

Rubinow and Keller (1961) assumed a rotationally static fluid, but in this thesis a modified form is adopted (Láin and Sommerfeld, 2008), namely:

$$I_p \dot{\vec{\omega}}_p = \vec{T} = \frac{\rho_f d_p^5}{64} C_R \vec{\Omega} |\vec{\Omega}| \quad [\text{A.4}]$$

where I_p [kg^2m^2], is the spherical moment of inertia about the centre, \vec{T} [Nm], is the resultant torque acting over the timestep, ρ_f [kgm^{-3}], is the fluid density, d_p [m], is the particle diameter and, C_R , is the coefficient of rotation.

For a spherical particle of uniform density, the moment of inertia about any diametric axis is given by:

$$\begin{aligned}I_p &= \frac{1}{10} m_p d_p^2 \quad \text{and} \quad m_p = \frac{4}{3} \pi \left(\frac{d_p}{2} \right)^3 \rho_p \\ \Rightarrow I_p &= \frac{\pi}{60} d_p^5 \rho_p\end{aligned}\quad [\text{A.5}]$$

where m_p [kg], is the particle mass and, ρ_p [kgm^{-3}], is the particle density.

Combining equations [A.4] and [A.5], it is found that:

$$\dot{\vec{\omega}}_p = \frac{\rho_f d_p^5}{64} C_R \vec{\Omega} |\vec{\Omega}| \cdot \frac{60}{\pi d_p^5 \rho_p} = \frac{60}{64\pi} \frac{\rho_f}{\rho_p} C_R \vec{\Omega} |\vec{\Omega}| \quad [\text{A.6}]$$

The Stokesian coefficient of rotation (Rubinow and Keller, 1961) is presented below, using the diameter as length dimension instead of the original radius. The limit

of the range, $0 < \text{Re}_r \leq 32$, is given by Laín and Sommerfeld (2008) since only creeping conditions are considered initially:

$$C_R = \frac{64\pi}{\text{Re}_r} = \frac{64\pi\mu}{\rho_f d_p^2 |\vec{\Omega}|} \quad [0 < \text{Re}_r \leq 32] \quad [\text{A.7}]$$

where Re_r is the rotational Reynolds number, defined in equation [3.38].

Combining equations [A.6] and [A.7], $\dot{\vec{\omega}}_p$ may be simplified:

$$\dot{\vec{\omega}}_p = \frac{60}{64\pi} \frac{\rho_f}{\rho_p} \frac{64\pi\mu}{\rho_f d_p^2 |\vec{\Omega}|} \vec{\Omega} |\vec{\Omega}| = \frac{60\mu}{\rho_p d_p^2} \vec{\Omega} \quad [\text{A.8}]$$

and therefore, using equation [A.1], the relaxation time is given by:

$$\Rightarrow H = \frac{60\mu}{\rho_p d_p^2} \Rightarrow \tau_\omega = \frac{\rho_p d_p^2}{60\mu} \quad [0 < \text{Re}_r \leq 32] \quad [\text{A.9}]$$

A ballistic rotational drag regime exists under higher Re_r conditions in which the rotation is proportional to the square of the relative angular velocity, for which an empirical fit was offered by Dennis et al. (1980). Recollection of the ballistic coefficient of rotation in equation [3.43], and substitution into equation [A.6] yields the angular acceleration under ballistic rotation conditions:

$$\dot{\vec{\omega}}_p = \frac{60}{64\pi} \frac{\rho_f}{\rho_p} \frac{128.4}{\text{Re}_r} k_R \vec{\Omega} |\vec{\Omega}| = \frac{120.375\mu k_R}{\pi \rho_p d_p^2} \vec{\Omega} \quad [\text{A.10}]$$

$$\Rightarrow H = \frac{120.375\mu k_R}{\pi \rho_p d_p^2} \Rightarrow \tau_\omega = \frac{\pi \rho_p d_p^2}{120.375\mu k_R} \quad [32 < \text{Re}_r \leq 1000] \quad [\text{A.11}]$$

where the non-linear dependence upon Re_r is introduced into the relaxation time by the rotation correction, k_R .